

ABSTRACT

WEBSTER, CAROLINE ELISE. Research in Support of the Design of a Hemiarthroplasty for Osteosarcoma of the Distal Radius in a Veterinary Model. (Under the direction of Drs. Ola Harrysson and Denis Marcellin-Little).

The use of hemiarthroplasty for limb sparing in osteosarcoma patients has been limited due to the manufacturing techniques and materials that have historically been used. In feline and canine models, the aim of this project was to study extensively the geometry of the distal aspect of the radius, develop novel ligament clamping methods, and evaluate suitable bearing materials for the application culminating in a proposed design of the hemiarthroplasty implant.

Computed tomography (CT) scanning is used to capture three-dimensional bone anatomy. The accuracy of CT data is limited by CT resolution. CT scans in two orientations and μ CT scans were compared to laser scanned data of the distal region of the feline radius. CTT overestimated CC and ML length by 4 to 10% while μ CT underestimated CC and ML length by 1%. CTL and CTT underestimated the ML radius of curvature by 15% while μ CT underestimated it by 3%. CTL and CTT overestimated the CC radius of curvature by more than 100% while μ CT underestimated it by 5%. Deviations from the articular surface were 0.26 ± 0.09 mm for CTL, 0.30 ± 0.28 mm for CTT, and 0.04 ± 0.02 mm for μ CT. Articular surface models derived from conventional CT images have dimensional errors approximately matching pixel size and do not allow the accurate determination of dimensions and radii of curvature in small joints. μ CT images are acceptable accurate for use in small joint hemiarthroplasty modeling. Additionally, μ CT scans were analyzed at incrementally decreasing resolution. A resolution of 0.192 mm was deemed appropriate for small joint hemiarthroplasty.

Secondly, while total arthroplasty replaces most functions of ligaments and tendons with mechanical features; hemiarthroplasty will require that ligament function be preserved to maintain acceptable joint function. Three primary ligaments are responsible for maintaining functionality in the feline radial carpal joint: the medial collateral ligament, the ulnar collateral ligament and the palmar fibrocartilage. A biomechanical evaluation was performed to evaluate three clamp-based ligament attachment methods using the medial collateral ligament. The in-tact ligaments exhibited an average maximum load of 122.55 ± 65.26 N and stiffness of 26.65 ± 9.49 N/mm. The manufactured clamps all had significantly ($P < 0.05$) lower maximum loads. The spiked texture had the highest mean maximum load at 45.5% of in-tact. Greater than 50% of in-tact stiffness was achieved by all clamping surfaces; however, both the flat and spiked textures had significantly lower stiffness values as compared to the in-tact specimen. The ridged texture stiffness did not differ significantly from the in-tact stiffness and the mean stiffness was 74.5% of in-tact.

A main limitation to the success of hemiarthroplasty in weight bearing joints in the past was cartilage damage due to mismatched material properties of metals used as bearing surfaces. With the advances made in polymer development, it is feasible that polymers used to replace small articular cartilage defects or that have similar properties to articular cartilage are suitable for hemiarthroplasty. Polyurethane and polyvinyl alcohol were evaluated in surface matched compression at two strain rates to determine the effect of creating functional geometries on the properties of the parts. Polyurethane exhibited higher average maximum loads at 65% strain for all thicknesses and strain rates. Additionally, the compressive tangent stiffness of all specimen increased as the

percent strain increased. The increase in thickness reduced the variability between specimens manufactured in the same material.

The final contribution of the work was a set of design parameters that should be used as a baseline for verification and validation of hemiarthroplasty implants.

Additionally, a custom patient specific workflow is proposed.

© Copyright 2018 by Caroline Elise Webster

All Rights Reserved

Research in Support of the Design of a Hemiarthroplasty for Osteosarcoma of the Distal Radius in a Veterinary Model

by
Caroline Elise Webster

A dissertation submitted to the Graduate Faculty of
North Carolina State University
in partial fulfillment of the
requirements for the degree of
Doctor of Philosophy

Industrial Engineering

Raleigh, North Carolina
2018

APPROVED BY:

Dr. Ola Harrysson
Co-Chair of Advisory Committee

Dr. Denis Marcellin-Little
Co-Chair of Advisory Committee

Dr. Harvey West

Dr. Jacqueline Cole-Husseini

Dr. Jonathan Richards-Stallings

BIOGRAPHY

Caroline Elise Webster was born in Orlando Florida. She moved to North Carolina and attended Davie County High School in Mocksville, NC. She received her B.S. in Biomedical Engineering with a concentration in Biomechanics from North Carolina State University in 2012. She then went on to receive her Masters in Industrial Engineering while working towards completing her PhD in Industrial Engineering from North Carolina State in 2016.

ACKNOWLEDGEMENTS

Research funding for a portion this dissertation was provided by the Leonard Leonard X. Bosack & Betty M. Kruger Charitable Foundation, Marshall, VA.

I would like to thank the following research collaborators: Dr. Corey Sims, Dr. Erin Koballa, and Dr. Anna Dunlap. Additionally, I would like to thank James Robey, Jimmy Thostenson, Amanda Hanley, Diana Courtright, Kristen Karasiewicz, Matthew White, Chet Wyrick, and Christopher Ledford for their technical support.

TABLE OF CONTENTS

LIST OF TABLES	iv
LIST OF FIGURES	vi
INTRODUCTION	1
LITERATURE REVIEW	5
Osteosarcoma	5
Limb Sparing	7
Hemiarthroplasty	14
Additive Manufacturing	21
RESEARCH GOALS	26
Objective 1	26
Objective 2	27
Objective 3	28
CHAPTER 1 – RADIAL CARPAL JOINT TOPOGRAPHY	29
1.1. Introduction	29
1.2. Literature Review	30
1.3. Materials and Methods	38
1.4. Results	47
1.5. Discussion	51
1.6. Conclusion	57
CHAPTER 2 – LIGAMENT FIXATION	58
2.1. Introduction	58
2.2. Literature Review	59
2.3. Materials and Methods	65
2.4. Results	71
2.5. Discussion	75
2.6. Conclusions	77
CHAPTER 3 – POLYMER BEARING SURFACE SELECTION	78
3.1. Introduction	78
3.2. Literature Review	78
3.3. Materials and Method	95
3.4. Results	100
3.5. Discussion	105
3.6. Conclusions	106
CHAPTER 4 – PROPOSED IMPLANT DESIGN FEATURES	107
4.1. Introduction	107
4.2. Relevant Background	107
4.3. Proposed Design Features and Process	112
CONCLUSIONS	115
REFERENCES	118
APPENDICES	129
Appendix A – Feline Radius Geometry Characterization Full Results	130
Appendix B – Imaging Modality Comparison Full Results	131
Appendix C – Resolution Study Results	145
Appendix E – Polymer Bearing Surface Compressive Testing	151

LIST OF TABLES

Table 1: Comparison of Total hip arthroplasty to HA Outcome Measures from Burgers et al. [7].	18
Table 2: Joint ROM prior to and following hemiarthroplasty of first MTP joint [51, 52, 54, 55].	20
Table 3: Scan Parameters for Biomodel Fabrication [75].	35
Table 4: Scan and Reconstruction Parameters [76].	37
Table 5: Mean \pm SD percent mass changes (positive numbers indicate an increase in mass) in relation to time zero.	40
Table 6: Measurement definitions and diagrams for distal radius measurements.	42
Table 7: Minimum Thresholding Value - Pilot Study Results.	46
Table 8: Mean \pm SD of important dimensions of the distal region of the feline radius between specimen capture using CMM (n=23).	47
Table 9: Mean \pm SD geometric differences between measurements collected using three computed tomographic modalities compared to a coordinate measurement machine (n = 23).	48
Table 10: Mean \pm SD of root mean square error deviation analysis at varying resolutions.	51
Table 11: Mechanical Properties of Canine Carpal Ligaments (Mean \pm SD) [110].	59
Table 12: Stress Relaxation Loading Protocol.	69
Table 13: Percent change w.r.t t=0.	70
Table 14: Test Protocol.	71
Table 15: Mean \pm Standard Deviation of Surface Roughness (n=3 per specimen).	72

Table 16: Mean \pm Standard Deviation of Maximum Load and Construct Stiffness.	73
Table 17: Maximum Load and Stiffness as a percentage of control specimen values.....	75
Table 18: Maximum Load as a percentage of normal / control of ligament and tendon attachment designs.	76
Table 19: Intrinsic Material Properties of Distal Femoral Articular Cartilage [128].	84
Table 20: Coefficient of friction in articular cartilage for various species [133].....	85
Table 21: Properties of PVA with varying amounts HA.....	92
Table 22: Aggregate modulus and permeability of emulsified PVA-PVP (a) with PLGA (b).....	94
Table 23: Mean \pm SD of maximum load of PVA-PVP Samples – 100% Strain Rate (n=3).	101
Table 24: Mean \pm SD of maximum load of PU Samples – 100% Strain Rate (n=3).	101
Table 25: Mean \pm SD of maximum load of PVA-PVP Samples – 1000% Strain Rate.....	101
Table 26: Mean \pm SD of maximum load of PU Samples – 1000% Strain Rate.....	101
Table 27: Results of Tukey’s post hoc test for maximum load as related to thickness.....	102
Table 28: Mean Compressive Tangent Stiffness (MPa, n=3).....	104
Table 29: Design elements of hemiarthroplasty in the canine radius from literature and experiments performed in the body of work above.	112

LIST OF FIGURES

Figure 1: Medical Patient Data to CAD Model Workflow.....	2
Figure 2: Low elastic modulus hip stem [5].	3
Figure 3: GEN1 (top) and GEN2(bottom) Implants (Veterinary Orthopedic Implants, Burlington Vermont) [36].....	11
Figure 4: Off-the-shelf endoprosthesis (Veterinary Orthopedic Implants, St. Augustine, FL) (top) [36], Custom patient specific limp sparing design (bottom) [41].....	13
Figure 5: Overestimation versus underestimation of MRI calculated cartilage thickness [87].....	33
Figure 6: Box plot showing differences between measurements derived from three computed tomographic (CT) modalities.	49
Figure 7: Representative mediolateral cross-sectional joint surface measurements of feline distal radial articular surfaces comparing three computed tomographic (CT) imaging methods (dashed lines) to coordinate measurement machine (CMM, solid lines). For longitudinal CT (A) and transverse CT (B), large positive and negative deviations from the CMM surface are visible. By comparison, μ CT measurements (C) closely approximate CMM measurements. The scale bar measures 1 millimeter.....	49
Figure 8: Representative CAD models of the distal portion of a representative feline radius showing positive differences between coordinate measurement machine data (visible in cream, A to D), longitudinal	

<p>computed tomographic (CT) data (in blue, B), transverse CT data (in purple, C), and μCT data (in pink, D).</p>	50
<p>Figure 9: Heat map of deviations between point clouds of feline distal radial articular surfaces imaged using a coordinate measurement machine compared to longitudinal CT scans (A), transverse CT scans (B), and μCT scans (C) of one representative sample. Negative deviations (cool colors) indicate that the CT models overestimated the surface and positive deviations (warm colors) indicate that the CT models underestimated the surface. Each image has a separate heat map scale: deviations are approximately 10 times smaller for the μCT compared to longitudinal and transverse CT.</p>	50
<p>Figure 10: Feline Carpal MCL Anatomy [111].</p>	60
<p>Figure 11: Tendon Attachment Devices: A) Fixation Plate, B) Spiked Washer, C) Custom Tendon Anchor [118].</p>	62
<p>Figure 12: Custom Tendon Attachment Prosthesis [119].</p>	63
<p>Figure 13: Porous Tantalum Washers for Tendon Attachment [109].</p>	64
<p>Figure 14: Porous tantalum washer for attachment of the canine patellar tendon [121].</p>	65
<p>Figure 15: Clamping Surface Texture Designs A) Flat (as manufactured using SLM), B) Grooved, C) Spiked.</p>	66
<p>Figure 16: Ligament Clamp Design – Side A (pink), Side B (blue).</p>	67
<p>Figure 17: Build Orientation of Clamping Surfaces.</p>	68
<p>Figure 18: Specimen loaded into ATS.</p>	70

Figure 19: Top – Clamp Side A (Sm), Bottom – Clamp Side B (Lg). From left to right – No Texture, Ridged Texture, Spiked Texture.....	72
Figure 20: Representative Load vs. Displacement Curve – Control Specimen.....	73
Figure 21: Representative Load vs. displacement curve: no texture as manufactured specimen.....	74
Figure 22: Representative Load vs. displacement curve: ridged texture as manufactured specimen.....	74
Figure 23: Representative Load vs. displacement curve: spiked texture as manufactured specimen.....	75
Figure 24: Arrangement of articular cartilage zones as illustrated by Newman. A) chondrocyte placement and orientation, B) collagen fiber placement and orientation [123].	80
Figure 25: Coefficient of friction over time during pendulum friction test [144].	89
Figure 26: Bearing surface offsets – Top 1.5 mm offset, Top + Center 2.5 mm offset, Full – 3.5 mm offset.	96
Figure 27: Polyurethane manufactured under different cooling environments. A) Room Temperature, B) Dry Ice in Ethanol, C) Liquid Nitrogen.....	97
Figure 28: As manufactured porous structures for attachment of molded PVA-PVP to bearing surface construct.....	98
Figure 29: PVA-PVP Hydrogel Specimen following molding - A) 1.5mm, B) 2.5mm, C) 3.5mm thickness).	99
Figure 30: PU surface matched compression testing setup.	100
Figure 31: Load vs Time curves for Polyurethane Material, Left – 1.5 mm	

INTRODUCTION

Additive manufacturing (AM) has had a growing influence in medical and veterinary fields since coming to market in the mid-1980s. Stereolithography (SLA) was the first technology to be commercialized and provided clinicians the luxury of physical patient specific polymer models. Partner technologies were later developed to simplify the data analysis required to convert clinical images into computer aided design (CAD) models required for additive manufacturing. Since then, the addition of AM capabilities in biocompatible metals has increased the influence of the technology into implantable components.

Typical workflow for patient specific AM models or implants involves performing medical imaging converting the images into the appropriate file types, and optimizing the build for accuracy of critical features and building components (Figure 1). The primary medical implant technologies are electron beam melting (EBM) and selective laser melting (SLM). Both processes utilize a metal powder bed as the feed stock material, however, their energy sources differ. SLM utilizes a laser and is performed at room temperature in an inert gas environment, and electron beam melting utilizes a beam of electrons and is performed at an elevated temperature in a vacuum. The two processes have different limitations; however, with both available a wide variety of implants can be successfully manufactured.

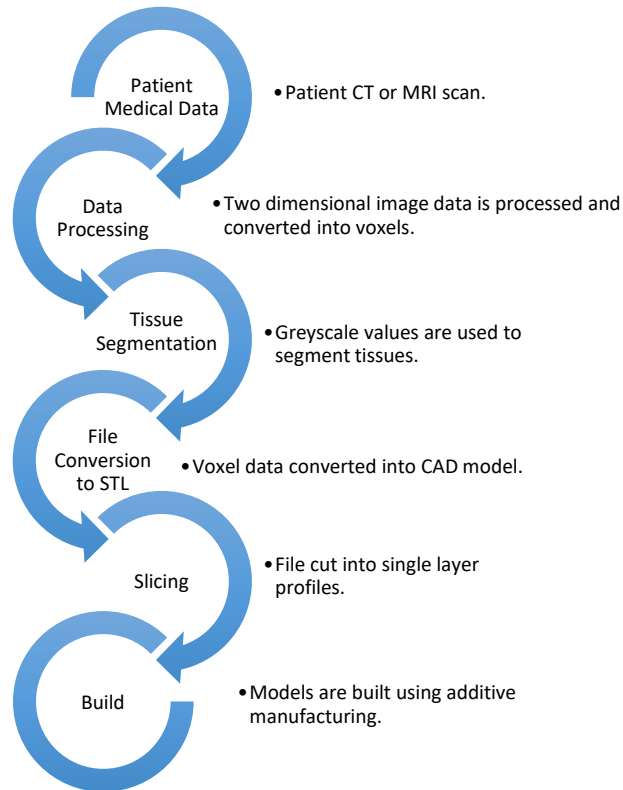


Figure 1: Medical Patient Data to CAD Model Workflow.

For medical applications in both the United States (US) and Europe, governing bodies have approved and/or cleared medical devices made using additive manufacturing processes. In the United States, the Food and Drug Administration (FDA) has cleared standard sized spinal implants manufactured using additive manufacturing [1]. Additionally, clearance has been granted for some patient specific implants manufactured using AM including facial prostheses [2] and cranial plates [3]. Clearance has also been granted to a patient specific total knee replacement that uses CT or MRI data for implant design and sizing [4]. For veterinary applications in the US, the FDA does not regulate veterinary devices, so the use of additive manufacturing and custom patient specific implants are at the discretion of clinicians and owners.

Joint replacement implants have long been a staple for improving function and quality of life as patients age or become injured; however, the mismatched properties of biocompatible metal implant materials and bone contribute to problems such as stress shielding and bone loss. Additive manufacturing has been utilized to manufacture prostheses with mesh geometries that are matched more closely to the bone properties in both medical and veterinary environments (Figure 2) [5].

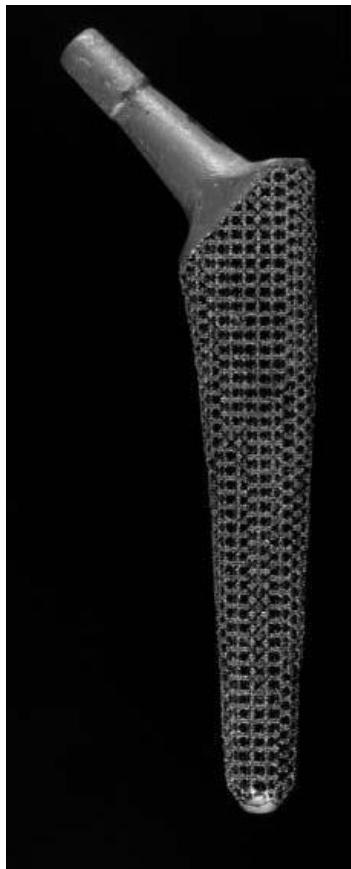


Figure 2: Low elastic modulus hip stem [5].

A great deal of research into the concept of hemiarthroplasty (HA) was completed with traditional manufacturing processes and is detailed in the literature review below. The technology at this time is primarily used in the hip and shoulder. In the shoulder joint, hemiarthroplasty patients are younger than patients that receive total

shoulder arthroplasty [6]. In the hip joint, hemiarthroplasty in the elderly is favorable when the patients have low activity levels [7]. The implants most often use metal bearing surfaces and are made of solid metal, like total joint replacement components. The failure of hemiarthroplasty as an alternative to total joint replacements in active individuals is largely attributed to the large-scale wear and damage of the opposing articular surface due to the mismatched properties between cartilage and common biocompatible metals.

The utilization of hemiarthroplasty with matched geometry; mechanical and wear properties; and suitable ligament clamping structures for limb sparing would provide a novel pathway to successful development and ultimately implementation of hemiarthroplasty. The proposed research includes research objectives culminating in an initial design framework of a novel hemiarthroplasty implant for limb sparing designed for additive manufacturing techniques in a canine model. The first objective is a geometric and surface characterization of the radius and radial carpal joint using feline cadaver limbs, and analysis of several CT scanning methods using 3-dimensional (3D) computer aided design (CAD) modeling software. The second objective of this research is to optimize ligament fixation methods for ligaments and tendons critical to function of the radial carpal joint. The final objective is to evaluate custom articular surface bearing of selected biocompatible materials for their suitability to articulate with cartilage.

Literature Review

Osteosarcoma

According to a review of osteosarcoma treatment published in 2014, the incidence of osteosarcoma is reported to be 0.3-3/100,000 people per year in the European union with a higher incidence of 0.8-11/100,000 adolescents between 15 and 19 years of age [8]. In the United States, the incidence of osteosarcoma is reported as 0.31/100,000 with an incidence of 0.44/100,000 before the age of 24 [9]. According to Anfinson et al., occurrence in the United States between 1976 and 2005 presented with a bimodal distribution with one peak at 20 years of age and another between 75 and 79 years of age [10]. Mirabello et al. investigated the worldwide incidence and also identified a bimodal distribution with a peak around puberty and another in the elderly population [11]. Primary site tumors are most commonly located in the distal femur, proximal tibia and proximal humerus with metastases most often located in the lungs [8]. The treatment of osteosarcoma often consists of preoperative and postoperative chemotherapy and surgical tumor removal. The most common drugs include high-dose methotrexate, doxorubicin, cisplatin, and ifosfamide. 35-45% of patients have tumors that are or become resistant to chemotherapy. Osteosarcoma is generally considered to be resistant to radiation therapy; however, radiotherapy may be used in cases where surgical resection is not an option. Several common chemotherapy agents increase the effectiveness of local radiation therapy [8].

In dogs, osteosarcoma is the most common bone tumor. The occurrence of osteosarcoma in the canine population peaks at a mean age of 7 years according to Mueller et al., with a secondary peak between 18 and 24 months [12]. Earlier, Brodey et

al., reported a similar peak in occurrence around 7 years of age, and attributed the second peak to a variance in life expectancy of breeds [13]. In a review of skeletal osteosarcoma, Brodey et al., noted that the most common sites for canine osteosarcoma are the femur, tibia, humerus and radius [14]. Szewczyk et al. reviewed canine osteosarcoma in 2015: similarly to the treatment in the human population, canine treatment consists of tumor removal via surgery combined with chemotherapy and or radiation. The three most common chemotherapy options are carboplatin, cisplatin, and doxorubicin; however, ifosfamide is also utilized. Similarly to the path of treatment in human medicine, radiation is not considered to be curative and outcomes are also improved with the combination radiation and chemotherapy [15].

The occurrence of feline bone tumors has been reported as 3.1-4.9/100,000 cases, of which 70-80% are osteosarcoma. Contrary to reports in humans and dogs, feline appendicular osteosarcoma is most prevalent at a single time point with Heldmann et al. reported a mean age at diagnosis of 8.03 years [16] and Kessler et al. reported a mean age at diagnosis of 10.1 years [17]. Both reports identified the distal portion of the femur, proximal portion of the humerus and tibia as the most common sites; however, Kessler et al. also found the digits to be commonly affected. Unlike in the canine population, amputation alone is considered curative in feline patients with osteosarcoma in the appendicular skeleton [16].

Liu et al. reviewed the treatment of cats examined between 1962 and 1972 and identified 15 cats with primary osteosarcoma. In five cats, surgical treatment included amputation or excision of the mass. One cat, had metastases in lungs and kidneys 5 months after amputation. The remaining cats survived with no evidence of metastases

for at least 26 months. [18] Tas et al. reported on a case of osteosarcoma in the tibia of a 13-year-old cat. The patient had a mid-femoral amputation and was prescribed NSAIDs for life [19]. Sonnenschein et al. published a case study of an 18-year-old cat with osteosarcoma in the distal portion of the femur. Amputation was performed at the hip joint and there metastases were not identified 11 months after surgery [20].

The use of spontaneous osteosarcoma in client-owned dogs has been discussed as an alternative to experimentally induced osteosarcoma in animal models. Rowell et al. presented several advantages for using the naturally occurring nature of cancers in dogs as models for human cancers. Namely, there are a large number of dogs that receive high levels of veterinary care, humans and dogs cohabitate, which may shed light on causes of cancers, and that large numbers of inherited diseases in humans also appear in dogs. In evaluating osteosarcoma specifically, the authors state that approximately 10,000 dogs are diagnosed yearly compared to 2,650 human diagnoses. Similar surgical and treatment approaches are used for both. Additionally, tumor pathology and genetics are more similar between dogs and humans than dogs and mice [21]. Mueller et al. also confirm the correlations between human and canine osteosarcoma and the use of dogs as a model for the human disease [22].

Limb Sparing

The management of osteosarcoma in human beings and dogs includes surgical tumor removal. Tumor removal without limb amputation is commonly referred to as limb sparing or limb salvage procedures. Limb sparing procedures provide the opportunity for the patient to regain use of the limb following treatment. According to Grimer, $\geq 85\%$

or more of pediatric and adolescent osteosarcoma patients receive limb-salvage surgeries [23]. That article refers to a single randomized trial showing no survival benefit of amputation compared to chemotherapy and limb salvage. However, Longhi et al. concluded that patients receiving limb salvage procedures do have a recurrence rate 10% higher than patients undergoing amputation but no increase in mortality [23, 24] . In dogs, Straw and Withrow report no significant difference in the survival rates of patients who undergo limb-sparing tumor removal and patients who undergo amputation [25].

Several limb-sparing techniques for adult patients have been reported, including modular endoprosthesis, resection without replacement, rotationplasty, allografts and autografts [26]. In pediatric and young adult patients limb-sparing options include modular endoprosthesis, whole bone prostheses, expandable endoprosthesis, allograft composite endoprosthesis, rotationplasty, massive osteoarticular allograft, and intercalary bone autograft [24]. In dogs, limb-sparing techniques include endoprostheses, allograft composite prostheses, cortical allografts, pasteurized tumoral autograft, and double bone transplantation [27]. The variety of available techniques indicates widespread research in the area; however, for the scope of this review the focus will be on artificial prosthesis based limb-sparing approaches.

Whole bone prostheses are used in adult skeletally mature patients when the proportion of bone involved in the tumor is high. Whole bone prostheses also involve the utilization of total joint replacements at the two joints of the involved bone. Liu et al. reported on the use of whole bone prostheses for tumors in the femur. Of the 21

patients, eleven could walk unaided and the mean functional outcome score was 75%. Complications included aseptic loosening (3), infection (3), patella fracture (1) [28].

Modular articulating endoprostheses are used in human patient age groups from pediatric to skeletally mature adult. With the rise in popularity of modular endoprosthetic reconstruction the majority of limb sparing procedures with endoprosthetic commercial implants are performed with modular endoprostheses. These modular implants provide an adaptable off-the-shelf alternative to creating a custom endoprosthesis; and for growing patients, modular components can be revised over time to adapt as the patient grows. Common complications reported with endoprosthetic reconstruction include aseptic loosening, infection, and local recurrence [29]. Galasso et al. also reported on a case of disassembly of a modular prosthesis [30]. Orlic et al. reported on the outcomes of 90 patients who received modular endoprosthesis of proximal femur, distal femur, or proximal tibia. They reported complications in 26 patients including local recurrence, infection, dislocations of prosthesis, and periprosthetic fractures [31]. Peterson et al. reported on the use of modular endoprostheses in the distal portion of the humerus in nine patients. Patients received a modular humeral component and a total elbow arthroplasty. Three instances of bushings failure requiring a revision of the prosthesis were reported. Overall, complication rates were low and authors reported that good functional outcomes were achieved [32]. Rosenbaum et al. reported on patient clinical functional outcomes as they related to patient activity level following reconstruction with modular endoprosthesis for osteosarcoma in the distal femur or proximal tibia. Although patients scored well on clinical function scales, compared to healthy controls they had significantly lower average number of step cycles. Additionally, healthy subjects spent

more time in every intensity activity level than patients that had received a modular endoprosthesis [33].

Ness et al. compared the function of expandable prostheses and modular prostheses in juvenile patients. Generally, patients expected to have a leg length discrepancy less than 4 cm or were skeletally mature at the time of surgery received modular prostheses, and patients with a potential leg length discrepancy of 4-6 cm received non-invasive expandable prostheses. The authors found no significant functional differences between the two groups in either the knee or hip. The expandable prosthesis provided an alternative to modular prosthesis as no surgical intervention was required during growth to compensate for leg length discrepancies [34]. Additionally, Neel et al. reported on the use of noninvasive expandable endoprosthesis reconstruction and reported that one potential advantage over the modular endoprosthesis was the elimination of additional required open surgery to adjust the prosthesis length. The authors reported on 18 implants placed in 15 patients. The implants were custom designed for each patient to compensate for anticipated growth. Sites included a total femur prosthesis, the distal portion of the femur and proximal portion of the tibia. At the time of publication, three patients had reached skeletal maturity and extension was complete with less than 1 cm of leg length discrepancy. The authors reported a 90% regain in functionality between pre- and post-lengthening [35]. Mangat et al. reported on the use of expandable prostheses in 131 patients. A complication rate of 48% was reported with the most common complications including infection, local recurrence, aseptic loosening, periprosthetic fracture, and several cases of patients outgrowing their prosthesis [29].

Limb sparing in veterinary applications have focused primarily on dogs. Several authors describe limb sparing procedures in the distal portion of the radius that require fusing of the carpal joint with plating. Mitchell et al. described the outcomes of 45 canine patients with osteosarcoma in the distal aspect of the radius that received either a 1st generation endoprosthesis (GEN1, Veterinary Orthopedics Implants, Burlington, VT) or 2nd generation endoprosthesis (GEN2, Veterinary Orthopedics Implants, Burlington, VT). The endoprosthesis were manufactured using 316L stainless steel (Figure 3). Previous studies evaluating the first-generation endoprosthesis showed endoprosthesis failure rates of approximately 40%, most commonly because of screw loosening or fracture of the bone proximal to the implant. A retrospective study comparing the first- and second-generation endoprosthesis found that the use of the second-generation endoprosthesis did not result in any decreased rates of implant-related complications or survival rates [36].

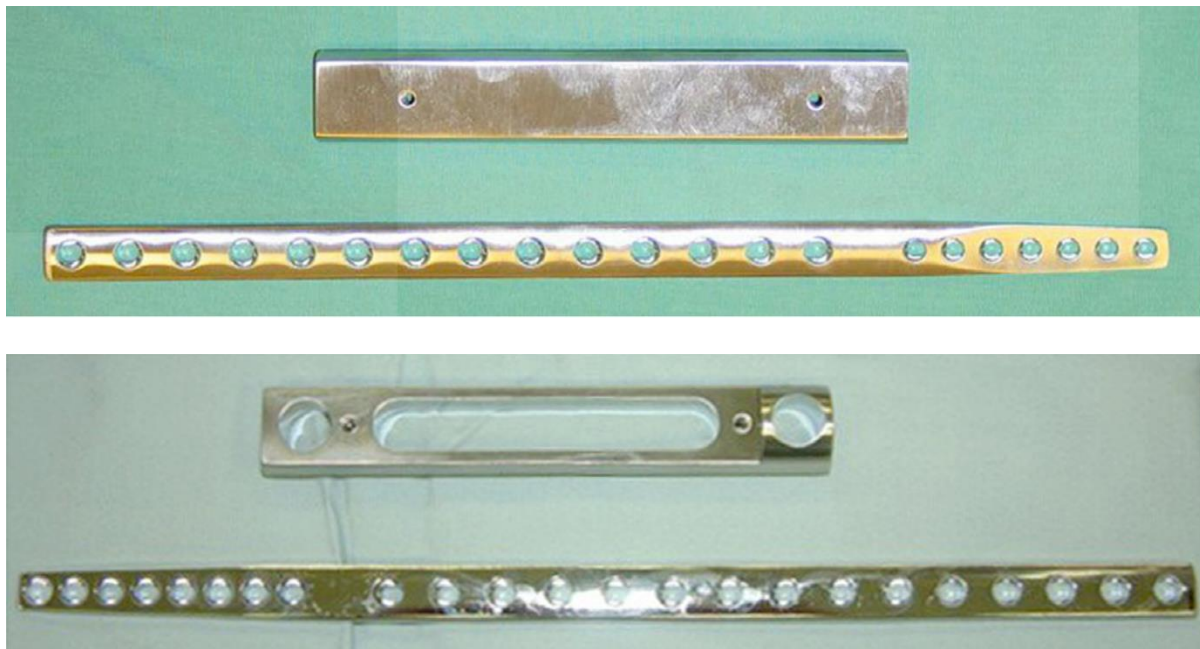


Figure 3: GEN1 (top) and GEN2(bottom) Implants (Veterinary Orthopedic Implants, Burlington Vermont) [36].

An additional case study series by Venzin et al. reported on the use of the GEN2 plate (Veterinary Orthopedic Implants, St. Augustine, FL) discussed above in two patients and an additional limb sparing plate (Locking Limb Salvage Plate, Veterinary Orthopedic Implants, St. Augustine, FL). The patients all had radiographic evidence of screw loosening in both the proximal aspect of the radius and metacarpals; however, the authors reported that two owners were satisfied with the outcome and the third declined further surgical intervention [37]. Venzin et al. reported on a case of a Rottweiler breed dog who received limb sparing surgery for osteosarcoma in the distal portion of the radius using the commercial limb sparing plate discussed above (GEN2, Veterinary Orthopedic Implants, St. Augustine, FL). Following improvement in limb function up to 4 months post-operatively, the limb function worsened. Severe bone resorption in the radius and metacarpal bone was visible on radiographs as well as screw loosening, leading to construct failure [38]. The aforementioned prostheses are standard and off the shelf, with limited variation available (only in length of prosthesis and type of screw used to secure the plate). The use of a porous tantalum implant for limb sparing in the distal portion of the radius was reported by MacDonald et al. The authors reported that although the patient had an infection post-operatively, at final follow-up (332 days) showed no signs of implant failure and the patient was weight bearing well [39]. Harrysson et al. reported on a clinical case of a large breed canine that had a tumor in the proximal aspect of the tibia. A custom limb sparing implant was used in addition to the femoral component of the total knee replacement. The implant was manufactured using additive manufacturing and implanted successfully in the patient [40]. Horn presented a custom patient specific limb sparing implant design for

osteosarcoma in the distal aspect of the radius. Figure 4 below shows the design of the off-the-shelf endoprosthesis for canine limb sparing in the distal portion of the radius, and the custom patient specific limb sparing design manufactured using electron beam melting. The use of additive manufacturing allowed for the tailoring of material properties, namely a reduction in stiffness. The author also reported a reduction in surgical time, and reduced limb stiffness as compared to the standard implant [41]. Custom patient specific limb sparing could provide an alternative and greater success to limb sparing procedures without the added complexity of a hemiarthroplasty implant.



Figure 4: Off-the-shelf endoprosthesis (Veterinary Orthopedic Implants, St. Augustine, FL) (top) [36], Custom patient specific limb sparing design (bottom) [41].

Limb sparing was reported in a case with osteosarcoma in the proximal region of the femur. Liptak et al. reported in 2005 on a case of a hybrid prosthesis limb sparing and allograft for an osteosarcoma in the proximal femur. A total hip replacement was utilized in combination with a proximal femur allograft from a bone bank. The authors reported improvement until a traumatic event 9 months postoperatively caused a luxation in the affected hip [42]. Limb salvage surgery has provided an alternative to amputation that helps to maintain limb function; however, it may not be ideal for return

to pre-illness physical activity levels. The development of a more diverse and robust limb sparing implant that have more flexibility in design and modularity would improve patient outcomes.

Hemiarthroplasty

Although limb-sparing techniques that include total joint replacement or arthrodesis (joint fusion) address some of the shortcomings of amputation, hemiarthroplasty could further improve quality of life and joint mobility by improving joint function as compared to arthrodesis.

Chung et al. published a study following 25 patients who received temporary hemiarthroplasty of the distal portion of the femur or proximal portion of the tibia as temporary measure until the patients reached skeletal maturity and transitioned to a traditional endoprosthesis. The femoral prosthesis had a metal bearing surface, while the tibial prostheses had a metal implant with a polyethylene bearing surface. Of the 25 patients who underwent hemiarthroplasty, three failures occurred in patients with a tibial hemiarthroplasty. Thirteen patients with UHMEPE bearing surfaces had evidence of cartilage degradation. Patients with a femoral hemiarthroplasty had overall better functional scores. The authors reported that some patients opted to maintain a hemiarthroplasty implant, 7/12 for femoral hemiarthroplasty implants and 4/13 for tibial hemiarthroplasty, rather than undergo a revision to a conventional total joint replacement style endoprosthesis. As a temporary measure to preserve a neighboring distal femoral physis, the procedure was successful, as patients showed no signs of premature closure of the physis [43].

A study of children undergoing hemiarthroplasty in the proximal portion of the femur focused on the effects of the prosthesis on the development of the acetabulum. Manoso et al. followed eight patients from hemiarthroplasty until death or conversion to total hip arthroplasty. In normal acetabular development, the acetabulum deepens and enlarges; however, no patient had measurable deepening or enlargement following hemiarthroplasty. All patients showed evidence of lateral translation of the prosthesis and younger patients experienced greater lateral translation. Functionally, all patients walked with a limp. Seven were considered cosmetic and one was considered major. Three patients used crutches or a walking aid – 1 continuously and 2 for prolonged walking [44].

Mayilvahanan et al. used measurements collected from radiographs to develop custom megaprotheses for bone tumors in the proximal portion of the humerus. Of the 57 patients who were followed for a minimum of two years (mean age 27.9), 24 had osteosarcoma. Surgical grade 316L stainless steel was used to manufacture all but eight of the prostheses. The eight remaining prostheses were manufactured using titanium. All were designed to be cemented into the humeral shaft. Excellent or good functional outcome was experienced by 78% of the patients. Reported complications included proximal migration (6), aseptic loosening (2), and humeral stem fracture (2). Using Kaplan-Meier survival analysis, the 5-year survival of the prosthesis in patients with primary sarcomas was 83.2% [45].

To the author's knowledge there is only a single published report of the use of hemiarthroplasty clinically in dogs; however, several studies have utilized animal models for hemiarthroplasty research. There were no reports of hemiarthroplasty being

used in cats and no reports of hemiarthroplasty utilization in the distal radius. Most hemiarthroplasty reports relate to the management of fractures or osteoarthritis.

As discussed previously, hemiarthroplasty patients are, on average, older than the majority of osteosarcoma patients; however, several studies with younger patients have been published. Van Egmond et al. published an observational cohort study with a mean patient age of 39 years (range, 13 to 66 years) at the time of hemiarthroplasty [46]. Patients in that study received a hemiarthroplasty due to osteonecrosis or malignant, benign or metastatic tumors. The unipolar hemiarthroplasty implant group had a higher failure rate and lower mean survival time of 1 year than the bipolar hemiarthroplasty implant group. Overall, after Kaplan-Meier survival analysis of both the unipolar and bipolar hemiarthroplasty implant groups, an overall 89% survival rate was calculated after 15 years and a 56% survival rate after 20 years. Separating the bipolar hemiarthroplasty group for the Kaplan-Meier analysis resulted in improved survival rate of 96% after 15 years and 60% after 20 years. The authors also noted that patients younger than fifty years of age had a higher rate of implant failure of total hip arthroplasty, primarily due to the failure of the acetabular component than patients older than fifty years of age. The major documented mode of failure reported is protrusion of the metal head due to erosion of the subchondral bone, which the authors state is influenced by activity level. The authors concluded that a bipolar hemiarthroplasty is a viable option for patients and would likely provide patients 15 to 20 years before needing to convert to a total hip arthroplasty [46]. These results show promise for the improved outcomes of osteosarcoma patients if superior hemiarthroplasty implants were to be developed.

Additionally, Price et al. retrospectively evaluated patients receiving cemented and uncemented hemiarthroplasty for metastatic tumors. The authors report that cemented prosthesis can increase the incidence of cardiopulmonary complications when used in other patient populations; however, they found that there was no additional cardiopulmonary complication risk when using hemiarthroplasty for metastatic tumors [47]. Although the research of Price et al. and van Egmond et al. show favorable results when utilizing hemiarthroplasty in cases of tumors and metastatic disease, Schneiderbauer et al. found a higher rate of dislocation after hemiarthroplasty procedures performed following a tumor resection than after hemiarthroplasty procedures unrelated to tumor resection [48]. The authors retrospectively reviewed over 1,800 patients who received hip hemiarthroplasty implant after tumor resection in the proximal femur or unrelated to a tumor resection. After Kaplan-Meier survival analysis, the ten-year dislocation rate was 10.9% for hemiarthroplasty following tumor resection and 2.1% for hemiarthroplasty unrelated to a tumor resection. The authors note that most dislocations occurred without trauma [48]. Because of the increased risk in dislocations for hemiarthroplasty following tumor resection, it is possible that standard hemiarthroplasty implants could be redesigned specifically for use with tumor resection to mitigate some of the dislocation risk. Additionally, as each tumor resection is unique, patient-specific implants could be considered a viable option as well.

The results of clinical outcomes for the most common procedures have been reported in meta-analyses and systematic reviews, pooling data from large numbers of patients to present a broad picture of success measures of procedures. Hip hemiarthroplasty procedures utilizing metal bearing surface prostheses are the most

widely reported load bearing clinical application of hemiarthroplasty. In 2012, Burgers et al., performed a meta-analysis evaluating the two main treatment choices for displaced femoral neck fractures in a healthy elderly population with a mean age of the included studies > 69. This analysis included variables such as patient pain measures, revision rate, one-year mortality rate, dislocation rate, and a quality of life measure. These measures were evaluated one to five years after the procedure (Table 1).

Table 1: Comparison of Total hip arthroplasty to HA Outcome Measures from Burgers et al. [7].

	Total Hip Arthroplasty	Hemiarthroplasty
Revision Rate	4%	7%
One Year Mortality Rate*	13%	15%
Dislocation Rate	9%	3%
Major Complication*	25%	24%
Minor Complication*	13%	14%
Harris Hip Score	81 pts	77 pts
Harris Hip Score (Subdomain Pain)	42 pts	39 pts
Rate of Patients Reporting Mild to No Pain	75%	56%
Western Ontario and McMaster Universities Osteoarthritis Index	94	78
EQ-5D Quality of Life	0.69	0.57

*Note: Authors report the measure did not differ statistically

From these data, the authors concluded that in elderly patients that are fit, total hip arthroplasty may be a preferable procedure; however, the authors noted the lack of literature available to definitively draw conclusions [7].

Complication, pain, and mortality rates have been frequently assessed in meta-analyses and reviews of hemiarthroplasty, which have varying results. Ahn et al. in 2008 reported no significant differences in pain following either a cemented or uncemented hemiarthroplasty [49], and Lup et al. reported lower pain levels for patients that received cemented hemiarthroplasty implants as compared to patients that received uncemented hemiarthroplasty [50]. Burgers et al. reported substantially higher rates for pain greater than mild in both uncemented (34.4%) and cemented (23.6%) [7]

than the Luo et al. study [50]. The one year mortality rate for hemiarthroplasty was reported to be 15% [7]; however, higher rates of 24.4% and 27.2% for cemented hemiarthroplasty and uncemented hemiarthroplasty respectively were reported in a second study [50]. No significant difference between patients that received cemented hemiarthroplasty and uncemented hemiarthroplasty were reported for revision rates and postoperative complications [49, 50].

Additional clinical literature reports of hemiarthroplasty in load bearing joints include joints in the feet, most commonly as a course of treatment to relieve symptoms of hallux rigidus (osteoarthritis). As reported by several authors, the current surgical standard treatment of severe hallux rigidus is joint arthrodesis [51, 52]. Dos Santos et al. reported that this procedure is not tolerated well by younger and/or active patients [51]. A common measure utilized to evaluate patients with hallux rigidus is the American Orthopedic Foot and Ankle Society (AOFAS) scale, which evaluates the following: pain, activity limitations, footwear requirements, metatarsophalangeal (MTP) joint motion, interphalangeal (IP) joint motion, MTP-IP stability, callus related to hallux MTP-IP, and alignment [53]. Five authors reported favorable significant differences between the results of the AOFAS scale pre- and post-operatively. Konkel et al. reported an increase in AOFAS score in 36 patients over an average follow up period of 72 months. The preoperative average score was 19 and the post-operative average score was 89 [54]. Sorbie et al. followed 19 patients for an average of 68 months and found an increase in AOFAS score from 56.8 pre-operatively to 88.2 post-operatively [53]. Dos Santos et al. reported that at follow up (3.5 years) of 11 patients the average AOFAS score was 77.27 as compared to an average preoperative score of 32 [51]. Ronconi et al. followed

21 patients for an average of 26.4 months and AOFAS scores improved to an average of 76.0 following hemiarthroplasty as compared to 47.5 prior to the procedure [52, 55]. In addition to favorable improvements in the AOFAS score, authors also reported significant favorable increases in joint range of motion summarized in Table 2 below.

Table 2: Joint ROM prior to and following hemiarthroplasty of first MTP joint [51, 52, 54, 55].

Authors	Average Follow Up	Pre-operative ROM	Post-operative ROM
Kissel et al.	12 months	20.6°	50°
Ronconi et al.	26.4 months	24.5°	52.6°
Dos Santos et al.	3.727 years	4.545°	21.818°
Konkel et al.	72 months	17°	72°

The ROM results obtained by Dos Santos et al. at the final follow up were lower, however not significantly, than the ROM evaluated 6 months following surgery of 43.6°. Dos Santos et al and Kissel et al. reported no failures or complications [51, 55]. Ronconi et al. reported a single patient experienced of implant loosening, two patients experienced lateral dislocation, and ten patients experienced dorsal subsidence [52]. Konkel et al. reported radiolucency in 35 of 36 patients at final follow up (mean 72 months) [54].

In a comparative study of the outcome of 21 hemiarthroplasty recipients and 27 arthrodesis recipients for the treatment of hallux rigidus, Raikin et al. reported five hemiarthroplasty failures, in addition to significantly less positive results of hemiarthroplasty when compared to arthrodesis. The AOFAS scores at final follow up (79.4 months for hemiarthroplasty and 30 months for arthrodesis) were reported as 64.6 for the hemiarthroplasty group and 83.8 for the arthrodesis group. The authors found no significant difference in the pre-operative AOFAS scores between groups. Additionally, hemiarthroplasty recipients had higher reported pain measured using the visual analog pain scale of 2.1 as compared to the value 0.7 for the arthroplasty group [56].

The single reported of clinical use of hemiarthroplasty in dogs was published by Sparrow et al. in 2014. A 7-month-old Saint Bernard due to an osteochondritis dissecans lesion comprising almost half of the humeral head [57]. A custom hemiarthroplasty implant was designed using measurements made from CT images and was fabricated from wrought stainless steel and a cobalt chromium alloy. The bearing surface of the implant was polished stainless steel and the surface of the implant in contact with bone was grit blasted and plasma sprayed with hydroxyapatite. Clinical assessment continued for 105 weeks after surgery. Pre-surgical lameness was subjectively graded as 6/10 to 7/10. 5-week post-operative lameness was graded as a 2/10 until 27 weeks post-operative when it was graded as a 1/10 and, at 47 weeks postoperative, there were no visible signs of lameness. An arthroscopic evaluation was performed at 47 weeks and evidence of low-grade cartilage disease on the caudal surface of the glenoid. Long-term clinical outcome at 2 years showed normal range of motion and no joint pain response to palpation. However, force plate analysis at 2 years showed a return to only 65% of normal peak vertical ground reaction forces [57]. This corroborates what is thought to be the reasons for selecting surgical interventions other than hemiarthroplasty in load bearing joints of healthy active younger patients. Wear and disease evidenced in 1 year in the cartilage opposing the metal surface confirms the need for better bearing materials to support the otherwise positive outcomes of hemiarthroplasty.

Additive Manufacturing

Additive manufacturing is an emerging class of manufacturing processes defined by the unique layer-by-layer addition of material. There are many additive

manufacturing processes, including SLM, EBM, SLA, material jetting, and fused deposition modeling (FDM). SLM and EBM can be used to fabricate parts made of implantable biocompatible materials. This technology review focuses on orthopedic implants manufactured using additive manufacturing.

Several reviews have been published recently about the role of additive manufacturing in medicine. The first review published in 2009 by Giannatis and Deduossis described the use of medical patient data to create physical models and the use of these models as surgical rehearsal tools, intra operative guidance and testing, and patient specific shielding masks. The parts were made of polymers and were manufactured using SLA or selective laser sintering (SLS). The authors reported several instances where additive manufacturing was used to fabricate custom patient specific implants used as patterns for titanium casting. Applications included skull defects, mandible replacements following tumor removal, and implants intended for total knee replacement. Patterns for polymer castings for use in dental applications and plastic surgery applications were also reported [58]. The authors did not report on any case where additive manufacturing was used to directly manufacture patient-specific implants.

In 2014, a review written by Sidambe focused on the biocompatibility of titanium implants manufactured directly using additive manufacturing or powder metal injection molding. The authors evaluated the effects of surface roughness and porosity of Ti6Al4V (Ti-64) implants. The EBM process demonstrate acceptable biocompatibility [59]. A study published by Haslauer et al. studied traditionally manufactured disks in addition to polished, unpolished and porous disks of EBM manufactured titanium and

found the biocompatibility to be comparable to traditionally manufactured Ti-64 implants. The authors described biocompatibility studies of direct metal laser sintering (DMLS) fabricated implants and reported studies acceptable biocompatibility [60].

In 2007, acetabular cups for total hip replacements manufactured using additive manufacturing received a European Community (CE) mark for commercial medical use. In the US, FDA approval was granted in 2010 [61]. Murr et al. reviewed designs and manufacturing methodology for orthopedic implants manufactured using additive manufacturing and reported on the clinical use of acetabular cups with low modulus mesh outer surface. The authors proposed several designs for mesh structures that can be used in conjunction with total joint replacements [62]. Wang et al. reviewed additive manufacturing topics in orthopedics, including the production of bone scaffolds and cited several examples of DMLS and EBM being used in cranial and maxillofacial surgery [63]. Xilloc, a company specializing in patient specific implants, was involved in the report of a patient receiving a total mandible replacement manufactured using additive manufacturing [64]. Studies with long-term follow-up of patients receiving custom patient specific implants manufactured using additive manufacturing are not available, since the technology is still emerging. As more individuals receive additively manufactured implants, reports describing the long-term survival of these implants will emerge.

In veterinary orthopedics, Harrysson et al. published a review summarizing advances in the field. To the authors' knowledge, a single off-the-shelf orthopedic implant manufactured using additive manufacturing was available: a low-modulus hip stem and acetabular cup (BFX cup and stem, BioMedtrix, Whippany, NJ). The bulk of

reports for veterinary orthopedics were custom patient specific implants. Potential uses of additively manufactured implants were listed including limb sparing applications, maxillofacial defect repair, spinal implants, implants for management of complex deformities, and complex fracture plating. Implants manufactured out of Ti-64 using the EBM process were described. Additionally, the authors reported on the use of additive manufacturing to manufacture custom patient specific osseointegrated prostheses. Custom bone plates and tissue attachment structures were designed and implanted. The implants included a portion that bridged internal bone plate and an external trunnion. The authors reported using both EBM and SLM to manufacturing Ti-64 implants [40].

Beyond clinical case studies, Marcellin-Little et al. compared the mechanical properties of hip stem-femur constructs in cadaveric canine femurs after implantation of a low modulus mesh hip stem and a commercially available cobalt chrome hip stem. The compressive strength of the low modulus mesh stem was reported to be greater than 80 MPa and the elastic modulus was reported to be 12 GPa. The construct stiffness was 995 ± 80 N/mm for the low modulus hip stem and 1606 ± 240 N/mm for the commercially available hip stem. This difference was statistically significant. Also, the hoop strains showed no significant difference at 800 N of loads, but two medial strain gages on EBM stems had significantly lower strain at the 1600 N/mm. Stress shielding is a significant problem in total joint replacement with commercially available, traditionally manufactured total joint replacements. The authors concluded that the low modulus stem showed acceptable performance for consideration in clinical applications [5]. There are no clinical reports of implants manufactured using additive manufacturing.

This technology, however, would provide the customizability and small features required to design a novel veterinary hemiarthroplasty.

Research Goals

The goal of this body of research is to *investigate the components of an implant design and develop a translatable design framework for hemiarthroplasty as a surgical intervention for osteosarcoma in the distal region of the radius*. This work is motivated by two general problems: 1) current surgical intervention for osteosarcoma is limited, especially in the veterinary space, 2) current use of hemiarthroplasty as a treatment for osteosarcoma has had little success due to the bearing material selected.

Objective 1

The first objective of this research is to *determine how to accurately capture required patient specific data for hemiarthroplasty*. The research objective is divided into three executable research tasks.

- 1.1) Characterize the geometry of the distal aspect of the radius
- 1.2) Quantify the difference between measured features of the distal aspect of the feline radius as captured using direct measurement and computed tomography (CT) scanning

The primary hypothesis for research tasks 1.1 and 1.2 is that current clinical CT imaging is not an acceptable data source for CAD models in small joints. Secondly, imaging the bone such that the long axis is perpendicular to the direction of bed travel will provide more accurate models than bones imaged in the common clinical orientation (long axis of bone is parallel to the direction of bed travel).

- 1.3) Determine an appropriate resolution required to accurately capture critical features of the distal aspect of the feline radius using computed tomography scanning

The hypothesis for research task 1.3 is that a resolution less than 0.6 mm and greater than 0.024 mm would be suitable for hemiarthroplasty in small joints.

Objective 2

The second objective of this research is to *investigate the manufacturability of critical ligament attachment features using additive manufacturing techniques*. The research objective is broken up into three executable research tasks.

- 2.1) Evaluate current ligament attachment methods in published literature.
- 2.2) Design and manufacture custom clamping surfaces for the feline medial collateral ligament
- 2.3) Determine the mechanical strength of the native ligament attachment as compared to the ligament attachment clamps.

The primary hypothesis for this objective is that one of the novel additively manufactured clamp designs will be suitable for use in a hemiarthroplasty implant in the distal portion of the radius. Secondly, the stiffness and strength of the developed attachment methods will be quantified.

Objective 3

The third objective for this research is to *assess the functional characteristics of selected polymeric bearing materials*. This research objective is broken into three executable research tasks.

- 3.1) Evaluate current materials that have appropriate wear characteristics for load bearing against articular cartilage in published literature.
- 3.2) Develop strategies for manufacturing surface matched bearing surfaces in two selected polymeric bearing materials
- 3.3) Evaluate the surface matched compression properties of the metal-polymer bearing surface construct

The primary hypothesis for this chapter is that one selected bearing material will have superior compressive properties.

Chapter 1 – Radial Carpal Joint Topography

1.1. Introduction

In order to accurately design a hemiarthroplasty aiming to replace the distal portion of the radius of the radial carpal joint one must first evaluate the shape of the existing bone, and the ability of current clinical imaging modalities to provide an accurate representation of the articulating surface. The 3D geometry of bones and joints is often captured using computed tomography (CT) scanning. CT scanning has been used to assess the shape and relative position of bones [65], estimate joint loads [66-68], assess joint pathology [69, 70], and plan surgical procedures [71]. The accuracy of articular surfaces captured using CT scans has been evaluated in several studies [72-74]. With the increase in popularity of additive manufacturing, CT data is commonly used to create CAD models or physical models. The accuracy of AM models produced from CT scan derived CAD models has been evaluated with a focus on CT scan parameters and CT scan segmentation parameters [75, 76]; however, neither study evaluated the accuracy of the CAD models produced from CT scans before model fabrication. Accurate CAD models generated from segmented CT scans are a key step for the accurate design and fabrication of patient-specific implants [77].

The purpose of the current study was to evaluate the accuracy of longitudinal CT (CT_L) and transverse CT (CT_T) of a small articular surface by comparing CT_L and CT_T measurements to microCT (μCT) measurements and to measurements collected using a laser-based coordinate measuring machine (CMM). Measurements included the overall dimensions, radius of curvature, and surface deviation. Subjectively, accuracy was considered acceptable if the magnitude of the deviation was < 0.6 mm (the slice

thickness selected in the study) for linear dimensions, < 0.75 mm for radii of curvature [78], and < 50 μm for mean deviations from the articular surface [79]. The authors hypothesized that μCT measurements had acceptable accuracy whilst CT_L and CT_T measurements did not have acceptable accuracy. The authors also hypothesized that CT_T measurements were more accurate than CT_L measurements.

1.2. Literature Review

Three-dimensional scanning and stereophotogrammetry have been previously used to evaluate the shape of cartilage and subchondral bone surface [80-82]. Laser coordinate measuring systems have also been used to evaluate bone shape [80, 83] and symmetry [84]. Studies evaluating CT scan accuracy and validation have also used laser and non-laser based coordinate measuring systems as the measurement standard in the human knee [85], human phalanx bone [79], and human spine [86]. Additionally, segmentation from computed tomography images have been validated using laser scanning [79]. Laser based coordinate measuring systems can also be used to evaluate the accuracy measurements of cartilage obtained by MRI data [85, 87, 88] and water displacement measurements [85].

CAD models generated from CT scans have been used to support the development of hemiarthroplasty implants in the distal portion of the human humerus. Using Mimics software (Materialise NV, Plymouth, MI), CT scan data was reconstructed to create 3D CAD models and to determine the flexion extension axis, and a humeral coordinate system. The results obtained support the use of anthropometric and

geometric surface analysis and characterization in the development of a hemiarthroplasty implant [83].

Although CT scan data can provide information about the shape of the subchondral bone, in the glenohumeral joint Soslowsky et al. used three-dimensional stereophotogrammetry to reconstruct cartilage and subchondral bone surfaces (cartilage dissolved in sodium hypochlorite solution). The radius of curvature was larger in males than females in the humeral head and the glenoid ($P < 0.002$), and the subchondral bone surface had less curvature than the cartilage surfaces ($P < 0.00005$) [82]. A similar study used CT scan data to calculate the radius of the humeral head in humans, and found statistically significant differences between the radius of subchondral bone and the radius of the articular cartilage surface ($P < 0.001$) [89]. From these results an understanding of the cartilage shape would be critical to determining geometry for a hemiarthroplasty implant in the shoulder. An analysis performed simply by CT would not have shown the cartilage surface and could have led to suboptimal fit of prosthetic components.

Millington et al. also used a stereophotography system with an accuracy of 2 μm to evaluate the cartilage volume, thickness, and surface area of the human ankle. Scans were acquired with intact cartilage and after dissolving cartilage in a sodium hypochlorite solution. The authors found no significant difference in the mean cartilage thickness of the talar and tibial cartilage; however fibular cartilage showed a significantly greater mean thickness than talar and tibial cartilage. The talus demonstrated a significantly larger surface area than the tibia and fibula. The coefficient of variation over the cartilage surfaces was calculated to be 30.21% for the tibia-fibula and the talar

cartilage. The authors conclude that this method could be used as a gold standard for validating the accuracy of MRI measurement techniques [88].

Several authors have evaluated the accuracy of MRI computations using scanning techniques as the standard of measurement. Trinh et al. used three-dimensional laser scanning to evaluate the cartilage morphology, volume, average thickness, surface area, and surface curvature of the human knee. Joints were imaged before soft tissue dissection using CT and MRI. A laser scan of intact cartilage was completed. Cartilage was removed using sodium hypochlorite, and a second scan was completed. The reported accuracy of the laser scanner was 50 μm . After alignment of the scans, an expert user manually outlined the articular cartilage region to be used in the measurements. Measurement validation was performed using an artificial model that was scanned with and without artificial cartilage. The volume of the artificial cartilage was then calculated from the scan and measured using water displacement. Thickness measurements were also calculated from the artificial scans and measured using calipers. The error between the scanned volume and water displacement measurements were 4.0% for femoral cartilage and 6.4% for tibial cartilage. The authors state that these errors are well within the errors for the water displacement method. The results of the thickness measurements using calipers were 4.5% for femoral cartilage and 3.6% for tibial cartilage, which the authors used to claim the laser scan data can be used as the true standard when evaluating the accuracy of MRI calculated measurements. The error between the laser scanned volumes and MRI calculated volumes ranged from 9.7% to 24.1% for femoral cartilage and 3.2% to 29.3% for tibial cartilage [85].

Koo et al. also performed an evaluation of accuracy of MRI measurements using laser scanning methods as the true standard in the human adult male knee. Like Trinh et al. MRI scans with the soft tissue intact were performed and subsequent laser scans were performed after the removal of soft tissue to capture the cartilage surface and geometry. An additional laser scan was performed after removing the cartilage with sodium hypochlorite solution to obtain the subchondral bone surface geometry. The error due to the dehydration of the cartilage was reported to be less than 1% due to the limited time the cartilage was exposed to air (22 minutes). The accuracy of the cartilage thickness measurements calculated from the MRI varied with the actual cartilage thickness ($p=0.05$) (Figure 5)[87].

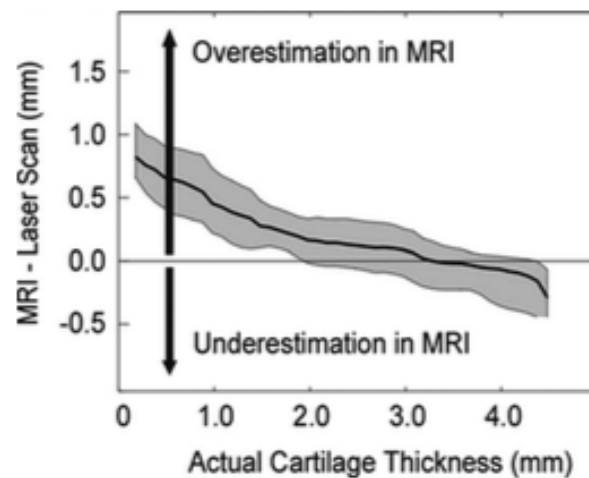


Figure 5: Overestimation versus underestimation of MRI calculated cartilage thickness [87].

As illustrated in Figure 5, cartilage thickness was overestimated for thinner regions of cartilage and underestimated for thicker regions. The range of cartilage thickness values where MRI calculation was most accurate was 2.5 to 3.3 mm [87]. The validation of reconstructions from computed tomography image data sets reconstructed

with BRAINS2 software has also been performed using 3D laser scanning by DeVries et al. Reconstructions were created by either smoothing the image data before surface generation or directly from unsmoothed image data and smoothing after surface generation using Laplacian smoothing. After CT scanning, the soft tissues were removed from the distal middle and proximal phalanx bones from the index finger of each specimen. Cartilage was removed from the surface by soaking in sodium hypochlorite. Three-dimensional laser scans were taken with a 0.2 mm resolution. The results show that the two smoothing techniques presented did not differ from the laser scanned surface measurements [79].

Podolsky et al. used a laser scanning system with a resolution of 100 μm to evaluate the use of a third toe osteochondral graft in a proximal interphalangeal joint reconstruction of the finger. Scans were taken with the cartilage surface intact and after dissolving cartilage in sodium hypochlorite. The authors then calculated the maximum and average cartilage thickness for each surface, as well as the coefficient of variation for the thickness across the surface. The authors reported results that in each comparison the mean thickness was significantly smaller and the coefficient of variance was significantly higher in the toes than fingers. The authors concluded that although differences exist between variance and thickness of the third toe cartilage, middle phalanx-based grafts may be suitable for proximal interphalangeal grafts [90].

In veterinary applications, Breit et al. used laser scanning to evaluate the subchondral bone surface of German Shepherd Dogs and Rottweilers with normal anatomy and bilateral fragmentation of the medial coronoid process of the elbow. The ulnae with fragmentation of the medial coronoid process of the elbow were biologically

macerated using *Dermestes Maculates* larvae and the normal ulnae were macerated using warm water. Using analysis of the laser scans the authors concluded that geometry did not play a role in the onset of bilateral fragmentation of the medial coronoid process of the elbow. The use of laser scanning was critical because MRI or other measurement techniques were deemed less than optimal for analysis of the canine elbow because of the closeness of opposing joint surfaces [80].

In order to evaluate the shape of an anatomic surface, several general steps have to be performed, each of which introduce error into the final result. First data must be acquired, then segmented or registered, then output for comparison. With the rise of additive manufacturing in medical modeling, several authors have explored the error associated with these steps and gone on to evaluate the accuracy of the final output of the additively manufactured medical model.

Fitzwater et al. performed the most comprehensive evaluation of CT scanning parameters, software image retro reconstruction methods, and modeling threshold reconstruction values on the accuracy of the additively manufactured models. An initial 156 data sets were evaluated and after elimination for gross errors in scan data, 17 scans were used to create biomodels using SLA and FDM. The ranges for penetrability, x-ray tube current, pitch, and radiation dosage can be found below in Table 3 [75].

Table 3: Scan Parameters for Biomodel Fabrication [75].

Scan Parameter	Minimum Value	Maximum Value
Penetrability (kV)	80	140
X-Ray Tube Current (mA)	60	160
Pitch	0.6	0.75
Radiation (mSv)	2.71	19.52

Based on the results of CT variables on accuracy of the biomodels, as penetrability increased biomodel accuracy increased for all measurements except bone length for which it had no effect. Additionally, an increase in X-Ray tube current corresponded to an increase in the caudal and cranial thickness measurements of the biomodels [75]. In 2015, Pinto et al. reported in more detail on the effects of each stage of pre-processing to obtain an additively manufactured biomodeling including patient imaging, segmentation, conversion to the .stl file format, manufacturing and infiltration. Unlike Fitzwater et al., Pinto et al. used a single printer to conduct their experiments (ZPrint 310 Plus, 3D Systems), and used a CT scan of the printed biomodel in order to perform comparisons between the CT scan data [76]. This procedure was previously published by Arrieta et al. in 2015 and provides information on accuracy based on the scan voxels [91]. The presence of voxels in the scan of the biomodel which were not present in the scan of the bone are reported as false positives, the lack of a voxel in the scan of the biomodel which is present in the scan of the bone were reported as a false negative [76, 91]. The various parameters modified by Pinto et al. can be found below in table 4. Slice thickness (1mm), field of view (6cm x 6cm), and matrix resolution (512x512 pixels) remained constant during each scan [76].

Table 4: Scan and Reconstruction Parameters [76].

Parameter	Baseline Value	Alternate Value(s)
Scan Acquisition Voltage (kV)	80	120, 140
Scan Acquisition Current (mA)	80	100
Lower Threshold Value for Segmentation (HU)	-668	-704, -686, -650, -632
Resolution of .stl Triangulation	High (Mean Area = 9.6mm ² , Standard Deviation = 9.3mm ²)	Medium (Mean Area = 18.9mm ² , Standard Deviation = 16.2mm ²), Low (Mean Area = 37.6mm ² , Standard Deviation = 31.3mm ²)
Layer Thickness for Manufacturing (mm)	0.0875	0.1
Material for Manufacturing	ZP150	ZP131
Infiltration Post-Manufacturing	Yes	No

Based on the modification of the parameters listed in Table 4 above. Pinto et al. reported that the baseline parameters had a false positive rate of just over 20% and no false negatives. Manipulation of the parameters yielded both positive and negative impacts on the accuracy of the CT scan of the biomodel. Increasing the acquisition voltage had an overall positive effect on the accuracy of the CT scan of the biomodel. Increasing the voltage decreased the rate of false positives and had no effect on the rate of false negatives as compared to the baseline values. Increasing the current however, served to decrease the accuracy of the biomodel scan resulting in no change in the rate of false positives and increasing the rate of false negatives as compared to the baseline values. During the segmentation process, decreasing the lower threshold bound increased the rate of false negatives and resulted in no change in the rate of false positives; however, increasing the lower threshold decreased the rate of false positives while increasing the rate of false negatives. The results of manipulation of the segmentation show that the ideal threshold value will likely introduce some false positive and false negative results. As was expected, decreasing the resolution of the stl

file resulted in an increase in global errors; and, increasing the layer thickness during printing increased the rate of false positives. The global errors were reported to be worse around regions of sharp curvature, and scans were taken without soft tissue making results difficult to interpret in a clinical setting [76].

Before the studies above were published, Hopper et al. presented 3D reconstructions of conventional and helical CT scans. Transverse scans with slice thickness of 2, 4, or 8 mm were acquired and the helical scans were performed with a pitch of 1.5 and 1.6 mm. Blinded radiologists reviewed and ranked the reconstructions from best to worst. The authors concluded helical CT scans produced higher quality 3D reconstructions than comparable conventional CT scans [92].

Huutilainen et al. also reported on the accuracy of the image data to .stl file conversion process by demonstrating the wide variance between software and user during the reconstruction process. Little information was provided on the scan parameters used; however, unlike the studies above, Huutilainen et al. used a cone beam computed tomography scan. The results confirmed the quantified variability in the Fitzwater et al. and Pinto et al. studies; reconstruction of image data can be a large source of variability in patient biomodels [93].

1.3. Materials and Methods

Cats euthanized at three local animal shelters for reasons independent from this research were used in this study. Skeletally immature cats as seen during physical examination or on CT scans were excluded. Forelimbs were harvested via scapular

disarticulation with intact soft tissues, were wrapped in saline-soaked gauzes, placed in airtight containers, and frozen at -20°C.

1.3.1. Patient Data Acquisition - Longitudinal and transverse CT scanning

Forelimbs were scanned using a multislice CT scanner (Siemens Sensation 64, Siemens, Washington, D.C.) with 140mA, 120 kVp, 0.6 mm slice thickness, 0.4 mm slice increment, 512 x 512 pixels, with a voxel size of 0.6³ mm³. Scans were done in two orientations: a conventional longitudinal orientation and a transverse orientation. The longitudinal orientation matches the orientation most commonly used to image clinical patients, the long axis of the bone is positioned parallel to the direction of travel of the table. The transverse orientation was scanned with the long axis of the bone positioned perpendicular to the direction travel of the table to maximize the number of slices with articular surface data.

1.3.2. Patient Data Acquisition - MicroCT sample preparation and scanning

The limbs were frozen in extension. A 4-cm-long section centered over the radiocarpal joint was prepared using a band saw. Specimens were scanned using a μ CT scanner (XTH 225 ST, Nikon, Melville, NY) at 150kV and 14.6 W, with a voxel size of 0.024³ mm³.

1.3.3. Patient Data Acquisition - CMM sample preparation and scanning

Enzymatic digestion was used to remove the articular cartilage of the distal portion of the radius without disturbing subchondral bone [94]. The optimal digestion

period was determined in preliminary work. Five radii were immersed in a papain solution (10 mg/mL papain, 5.5 mm L-cysteine, 10% penicillin-streptomycin-amphotericin in phosphate buffered saline) at 37°C. The bones were dried and weighed after 30 minutes, 2 hours, every 6 hours for 24 hours, and every 12 hours for the remainder of 72 hours (Table 5).

Table 5: Mean \pm SD percent mass changes (positive numbers indicate an increase in mass) in relation to time zero.

Time	% Mass Change
30 min	7.1 \pm 1.0
2 hrs	6.5 \pm 1.2
6 hrs	-6.6 \pm 5.
12 hrs	-15.4 \pm 4.1
18 hrs	-19.9 \pm 4.5
24 hrs	-23.1 \pm 4.4
36 hrs	-29.6 \pm 14.5
48 hrs	-28.6 \pm 14.1
60 hrs	-29.0 \pm 14.2
72 hrs	-29.5 \pm 13.9

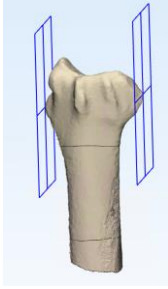
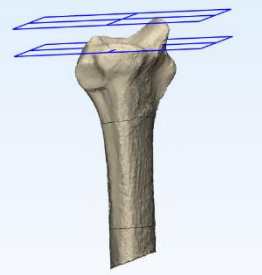
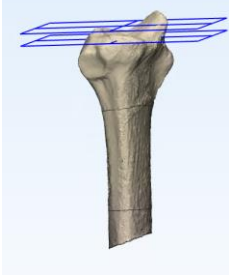
Mass change between 36 and 72 hours was negligible; therefore, a 36-hour dissolution was selected. Carpal joints were dissected and the articular cartilage of the distal portion of the radius was lightly coated with talcum powder, and scanned using a laser scanner (FARO Edge Scan Arm, FARO, Lake Mary, FL) to acquire point clouds of the radial articular surface. Specimen were rinsed and the articular cartilage was enzymatically digested. Following digestion, the specimen were rinsed, coated with talcum powder and a second laser scan was completed.

1.3.4. Reconstruction and analysis methods - feline radius geometry characterization

The CMM data was imported into CAD software (3-matic v. 9, Materialise, Plymouth, MI) and anatomic planes were assigned to each sample using known

landmarks and visual verification. The following measures were then taken with respect to the established anatomic planes (Table 6).

Table 6: Measurement definitions and diagrams for distal radius measurements.

Dimension	Definition	Diagram
Mediolateral (ML) Width	Distance between most medial and most lateral points on the radial head perpendicular to planes	
Cranio-caudal (CC) Width	Distance between most cranial and most caudal points on the radial head perpendicular to planes	
Full Depth of Articular Surface	Distance in the transverse direction between the most distal point on the articular surface and most proximal point on the articular surface	
Primary Bearing Depth of Articular Surface	Distance in the transverse direction between the most proximal point on the articular surface and the most distal point on the medial portion of the bearing region of the articular surface	
Radial Shaft Diameter	Fit Cylinder to the proximal region of the shaft of the radius	

1.3.5. Reconstruction and analysis methods – imaging modality comparison

DICOM images from the CTL, CTT, and μ CT were imported using image processing software (Mimics v. 20.0 & 21.0, Materialise, Plymouth, MI) to reconstruct 3-dimensional CAD models of the radius using the *marching cubes* algorithm. CT scans were filtered and selected to include grayscale values ranging from 226 to 3053 HU. If image manipulation was required to separate the radius from the radial carpal bone and ulna, the geometry of the articular surface of the radius was not altered. The μ CT images were filtered and selected to include all grayscale values > 2358 HU. Additional steps were not required to isolate the radius from the radial carpal bone and ulna. Output files (.stl format) were generated using an optimal generation setting to avoid smoothing or data averaging during processing.

The CMM scans were registered to create a single point cloud model for each specimen using automatic registration in the modeling software (Geomagic Studio, 3D Systems; Rock Hill, SC). Outliers and disconnected components were removed before the creation of .stl files of laser scanned bone models. The .stl files from CTL, CTT, and μ CT were compared to CAD model derived from the laser scanned point cloud data which was used as the gold standard. Anatomic reference planes (coronal, parasagittal, and transverse) were assigned to each model of the laser scan data in CAD software (3-matic v. 9, Materialise, Plymouth, MI). The radial articular surface was manually bounded and separated in CAD software and coronal, transverse, and parasagittal anatomic planes were aligned to the global coordinate system. Using Python scripting, .stl files were imported into the modeling software. A two-phase *best-fit* alignment of the .stl file of the laser scan, the CTL, CTT, and μ CT .stl files was performed. The initial

alignment was done with high precision fitting and a tolerance of 1e-6 mm. A second fitting was done with high precision fitting and fine adjustments only enabled to further reduce fitting errors. To evaluate the craniocaudal (CC) radius of curvature, planes parallel to the parasagittal plane spaced 0.5 mm apart were created across the articular surface of the laser scan model using the *automation* feature and identical planes were created for the CT_L, CT_T, and μ CT CAD models. The radius of curvature was calculated using the 2D measurements feature, with a rectangular bounding box and a radius calculation with *best-fit* option. The rectangular bounding box was user inputted based on the curved region of interest in the gold standard and duplicated using the *automation* feature for all other imaging modalities. Mediolateral (ML) radius of curvature was calculated similarly within planes parallel to a coronal anatomic plane spaced 0.5 mm apart.

Surface deviation calculations were performed using the quality control software after the same two-phase *best-fit* alignment procedure described above. The articular surface of the laser scan point cloud was manually selected and that region was compared using the *3D deviation tool* (maximum deviation, 10 mm; maximum angle, 45°) to calculate mean and maximum positive and negative deviations.

To measure ML and CC widths, *.stl* files were imported in the CAD software and aligned using an initial manual *n-points* alignment (3 points on articular surface, 2 points on bone shaft) where the laser scan was the fixed model and CT_L, CT_T, and μ CT models were floating. An additional global alignment was performed using the *automatic alignment* feature (tolerance, 1e-6 mm). Planes parallel to the CC plane were created at the most dorsal and most palmar aspects of the distal portion of the radius. Planes

parallel to the ML plane were created at the most medial and most lateral aspects of the distal portion of the radius. The distance between the most medial and most lateral plane was recorded as ML width, and the distance between the most dorsal and most palmar plane was recorded as CC width.

The study sample size was determined using an *a priori* power analysis from a pilot study of five specimens. A complete block design statistical model was developed for the experiment using differences (Imaging Modality – Laser Scan) for each evaluated value. The residual effects were assumed to have a normal distribution with mean 0 and non-equal variance with respect to treatment. A restricted likelihood test of variances was used to analyze significance of variance differences. *P* values < 0.05 were considered significant.

1.3.6. Reconstruction and Analysis Methods – Resolution Selection

DICOM images from three pilot μ CT scans were imported into an image processing software (Mimics v. 21.0 - alpha, Materialise, Plymouth, MI) using Python scripting. Each pilot scan was converted using lossless compression, and the resolution was decreased using resolution change features built into the scripting module. The following resolutions were evaluated: 0.024 mm (Control – As μ CT Scanned), 0.048 mm, 0.096 mm, 0.192 mm, 0.384 mm. Using a manual operation, a profile line was placed through the converted image in the axial plane and greyscale values were plotted with respect to position along the line placed through the bone. The lower bound for the minimum greyscale value for evaluation was selected based on the peak of the lower regions of the curve at 2700. The upper boundary was selected by

visualizing a clear gap between the articular surface boundary and the thresholded voxels at 4500. Thresholding was then performed in 150 unit increments between the lower and upper minimum thresholding bounds, and the radius was automatically separated using a seed point and region growing. CAD models were then exported.

Surface deviation calculations were performed using the quality control software after the same two-phase *best-fit* alignment procedure described above for the whole bone surface. The mean and standard deviation of the RMSE was calculated using Python scripting. An optimal thresholding minimum for each resolution was selected based on the minimum deviation of the RMSE mean of the pilot samples (Table 7).

Table 7: Minimum Thresholding Value - Pilot Study Results.

Resolution (mm)	Thresholding Minimum Value
0.024	3000
0.048	3000
0.096	2850
0.192	2850
0.384	2850

The above procedure was repeated for all specimen using the minimum thresholding values as determined by the pilot analyses, and a region of interest of 5 mm.

A complete block design statistical model was developed for the experiment using differences (Imaging Modality – Laser Scan) for each evaluated value. The residual effects were assumed to have a normal distribution with mean 0 and equal variance with respect to treatment. *P* values < 0.05 were considered significant.

1.4. Results

An *a priori* power analysis was performed using results from a five specimen pilot study using the methods described above. A target power of 0.8 was selected, and the analysis indicated a sample size of 24 was sufficient. Twenty-four specimens were included. One specimen was lost due to skeletal immaturity that was undetected before cartilage digestion, leaving 23 radii. Full data sets can be found in appendices A – C.

1.4.1. Feline radius geometry characterization

The geometry of the feline radius was characterized, and the size of the features of interest of the feline radius may pose imaging challenges for high accuracy modeling for custom patient specific hemiarthroplasty (Table 8).

Table 8: Mean \pm SD of important dimensions of the distal region of the feline radius between specimen capture using CMM (n=23).

Measure	Mean \pm SD (mm)
ML Distance	12.08 \pm 2.86
CC Distance	8.07 \pm 1.91
Shaft Radius	2.61 \pm 0.66
Depth of Full Articular Surface	2.84 \pm 0.67
Depth of primary bearing region of articular surface	1.40 \pm 0.33

1.4.2. Imaging modality comparison

Mean \pm SD percent errors were larger for CT_L and CT_T than μ CT for every measure evaluated (Table 9). The mean difference in ML width between CMM measures and CT_L, CT_T, and μ CT respectively were smaller but not significantly for μ CT than other measures CT_L and CT_T. The mean difference in CC width between CMM measures and CT_L, CT_T, and μ CT were significantly different between each imaging modality.

Table 9: Mean \pm SD geometric differences between measurements collected using three computed tomographic modalities compared to a coordinate measurement machine (n = 23).

	Laser Scan (CMM)	Longitudinal CT (CT _L)	Transverse CT (CT _T)	MicroCT (μ CT)
ML length				
Length (mm)	12.64 \pm 0.92	13.06 \pm 0.84	13.13 \pm 0.88	12.47 \pm 0.81
Difference with laser scan (mm)	-	0.43 ^a \pm 0.41 ^d	0.49 ^a \pm 0.41 ^d	-0.17 ^a \pm 0.16 ^e
Error (%)	-	3.62 \pm 3.31	4.48 \pm 2.59	1.30 \pm 1.12
CC length				
Length (mm)	8.37 \pm 0.66	8.86 \pm 0.67	9.20 \pm 0.72	8.34 \pm 0.62
Difference with laser scan (mm)	-	0.49 ^a \pm 0.20 ^d	0.83 ^b \pm 0.26 ^d	-0.03 ^c \pm 0.10 ^e
Error (%)	-	5.91 \pm 2.37	9.97 \pm 3.08	0.82 \pm 0.86
ML radius of curvature				
Difference with laser scan (mm)	-	-0.37 ^a \pm 0.93 ^d	-0.31 ^a \pm 1.15 ^d	-0.19 ^b \pm 0.24 ^e
Error (%)	-	12.04 \pm 10.48	14.25 \pm 18.06	2.52 \pm 2.79
CC radius of curvature				
Difference with laser scan (mm)	-	2.58 ^a \pm 22.55 ^d	5.48 ^a \pm 41.99 ^e	-0.10 ^a \pm 0.27 ^f
Error (%)	-	99.41 \pm 549.31	256.57 \pm 1,716.59	5.18 \pm 4.80
Surface Deviation				
RMSE (mm)	-	0.26 ^a \pm 0.09 ^d	0.30 ^a \pm 0.28 ^d	0.04 ^b \pm 0.02 ^e
Maximum positive deviation (mm)	-	3.04 ^a \pm 1.17 ^d	2.45 ^a \pm 0.90 ^d	0.38 ^b \pm 0.18 ^e
Maximum negative deviation (mm)	-	-1.18 ^a \pm 1.11 ^d	-1.53 ^b \pm 0.73 ^d	-0.26 ^c \pm 0.11 ^e

Within a row, mean values with different superscripts differ statistically ($P < 0.05$). Within a row, standard deviation (SD) values with different superscripts differ statistically ($P < 0.05$)

The mean difference was smallest for μ CT and largest for CT_T. The mean ML ROC difference between imaging modality and CMM was larger for CT_L and CT_T than for μ CT (Figures 6-7). The CC ROC difference between imaging modalities and CMM did not differ statistically for CT_L and CT_T compared to μ CT.

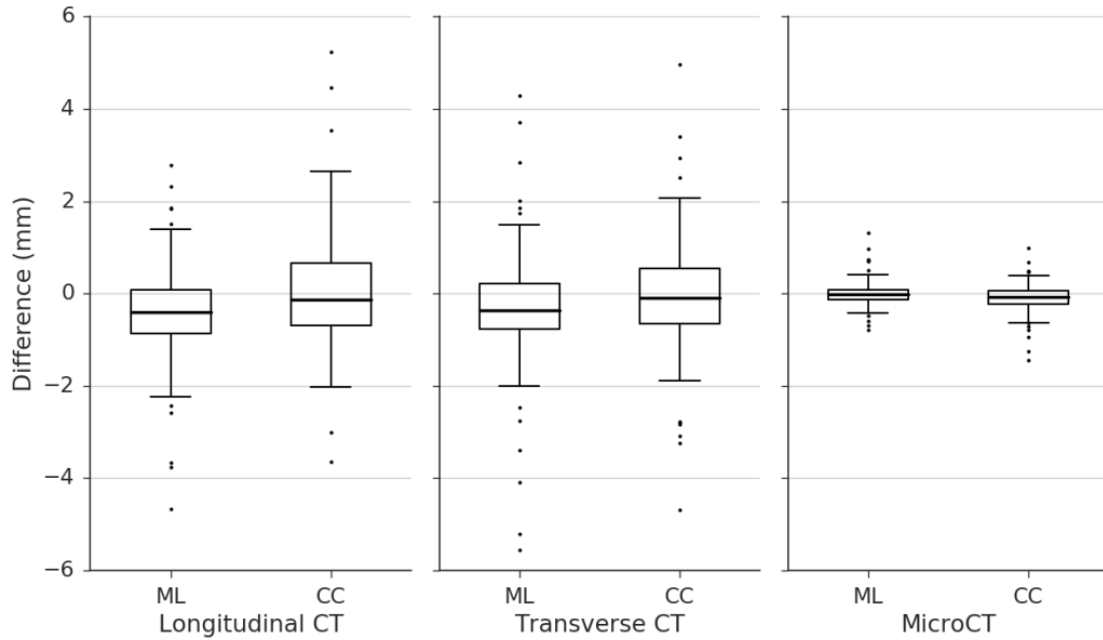


Figure 6: Box plot showing differences between measurements derived from three computed tomographic (CT) modalities.

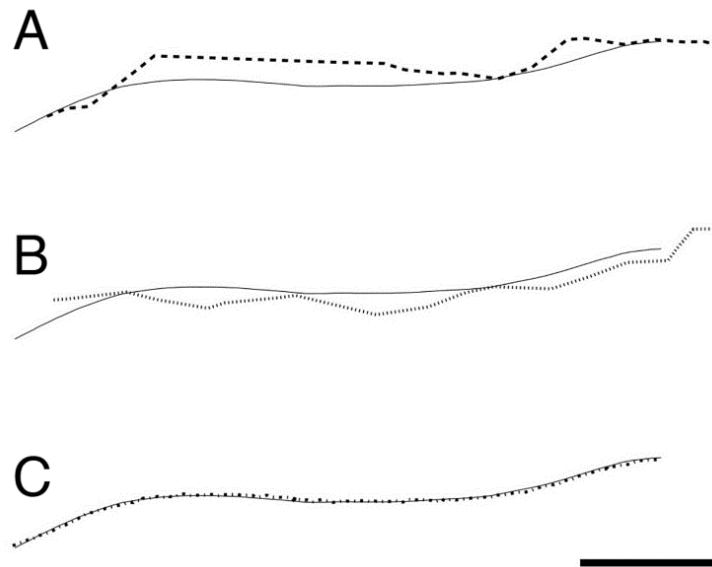


Figure 7: Representative mediolateral cross-sectional joint surface measurements of feline distal radial articular surfaces comparing three computed tomographic (CT) imaging methods (dashed lines) to coordinate measurement machine (CMM, solid lines). For longitudinal CT (A) and transverse CT (B), large positive and negative deviations from the CMM surface are visible. By comparison, μ CT measurements (C) closely approximate CMM measurements. The scale bar measures 1 millimeter.

The root mean square error (RMSE) of the deviation from the articular surface was larger for CT_L and CT_T models than for μCT (Figure 8). The mean maximum positive surface deviation was higher for CT_L and CT_T models than for μCT models. The difference in the mean minimum negative surface deviation was statistically significant between all measures. The mean difference was smallest for μCT and largest for CT_T (Figure 9). The variance between μCT and CMM was significantly smaller than CT_L and CT_T for all measures. Statistically significant differences in variance between CT_L and CT_T were only present for CC ROC.

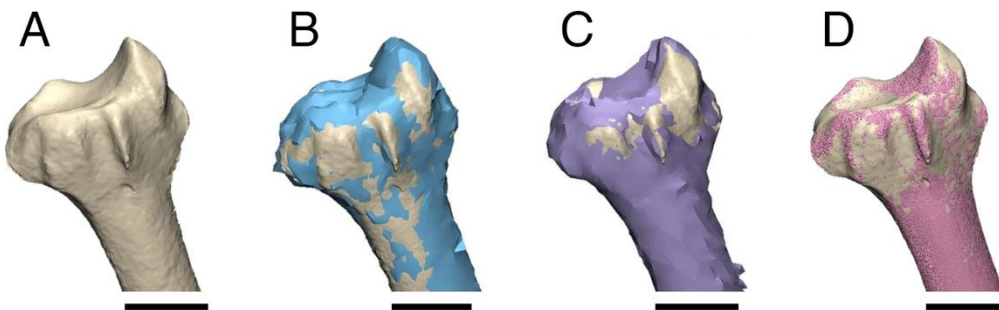


Figure 8: Representative CAD models of the distal portion of a representative feline radius showing positive differences between coordinate measurement machine data (visible in cream, A to D), longitudinal computed tomographic (CT) data (in blue, B), transverse CT data (in purple, C), and μCT data (in pink, D).

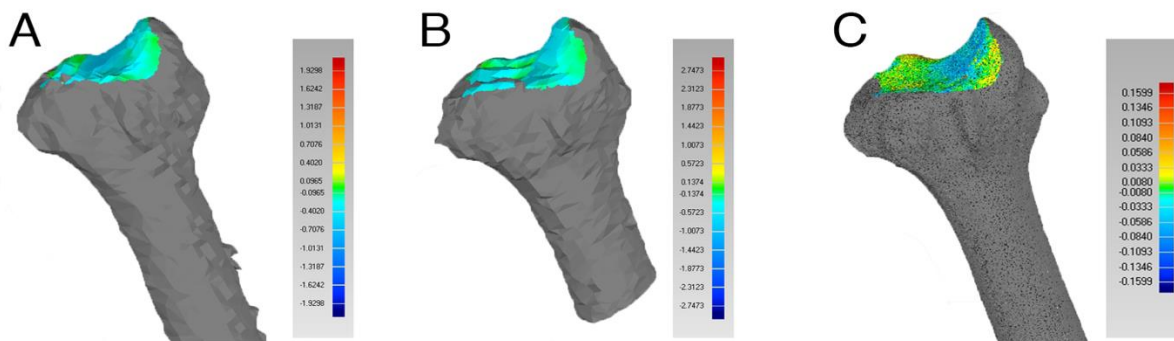


Figure 9: Heat map of deviations between point clouds of feline distal radial articular surfaces imaged using a coordinate measurement machine compared to longitudinal CT scans (A), transverse CT scans (B), and μCT scans (C) of one representative sample. Negative deviations (cool colors) indicate that the CT models overestimated the surface and positive deviations (warm colors) indicate that the CT models underestimated the surface. Each image has a separate heat map scale: deviations are approximately 10 times smaller for the μCT compared to longitudinal and transverse CT.

1.4.3. Resolution Selection

A subset (n=15) of CMM and μ CT data were evaluated to determine an appropriate resolution level for the feline radius for custom patient specific hemiarthroplasty design. Differences in resolution values between 0.024 mm and 0.192 mm were not significantly different. A resolution of 0.192 mm would be acceptable to image the feline radius for high accuracy CAD modeling for custom patient specific hemiarthroplasty (Table 10).

Table 10: Mean \pm SD of root mean square error deviation analysis at varying resolutions.

Resolution	Mean \pm SD (mm)
0.024 mm	0.048 ^a \pm 0.02
0.048 mm	0.065 ^a \pm 0.01
0.096 mm	0.068 ^a \pm 0.01
0.192 mm	0.084 ^a \pm 0.01
0.384mm	0.120 ^b \pm 0.01

mean values with different superscripts differ statistically ($P < 0.05$)

1.5. Discussion

In this study, the geometry of the distal region of the feline radius was characterized. 3D CAD models derived from conventional longitudinal CT imaging (CT_L), from transverse CT imaging (CT_T), and from μ CT were compared to each other and to laser scanned surfaces to assess their relative accuracy; from which an acceptable resolution was selected for imaging the carpal joint for a radial hemiarthroplasty. The distal radial articular surface was selected because small articular surfaces with complex curvature are most affected by imaging modality. Additionally, the distal aspect of the radius is a common site of limb sparing in companion animals and a site of hemiarthroplasty in human beings [95, 96]. An accurate assessment of joint surface geometry is a prerequisite for the optimization of

articulating custom orthopedic implants, such as custom arthroplasties or hemiarthroplasties.

Linear deviation measurements of the articular surface (length, articular surface deviation) differed among modalities: the accuracy and the precision were lower for CT_L and CT_T measurements compared to μCT measurements, most of these differences (4/5 for mean, 5/5 for variance) were statistically significant. We accepted the hypothesis that μCT measures had acceptable accuracy and CT_L and CT_T did not have acceptable accuracy. The lack of statistically significant differences in ML length between CT_L , CT_T , and μCT may have resulted from the fact that ML length was the longest linear measurements and imaging errors were smallest relative to the overall size measured or from the relatively large variance present in CT_L and CT_T measurements. Differences in the accuracy of μCT and CT_L / CT_T were the likely consequence of the increased resolution of the μCT relative to CT_L and CT_T . The μCT voxel edges were approximately 25 times smaller than voxel edges of CT_L and CT_T . μCT included approximately 15,000 more voxels than CT_L or CT_T . The dimensions of the voxel are made up of in-plane pixel size (a combination of the field of view and matrix dimensions) and slice thickness. While decreasing voxel volume increases geometric accuracy, it would increase the radiation dose. In a study evaluating the influence of slice thickness on patient radiation dosing, a decrease in slice thickness increased the radiation dose [97].

Measurement accuracy and precision did not differ statistically between CT_L and CT_T for most linear deviation measures (3/5 for mean, 5/5 for variance). We therefore rejected the hypothesis that CT_T was more accurate than CT_L . The lack of improvement

in models created from CT_T as compared to CT_L was unexpected since there were 3 times as many slices containing articular surface data with the CT_T orientation compared to the CT_L orientation. Subjectively, CAD models reconstructed from the CT_T scans had more noise than CT_L , likely because of the increased length of x-ray travel within specimens. The resulting beam hardening may have been responsible for the lack of increase in accuracy in CT_T relative to CT_L . Beam hardening has been well described in the literature [98]. Effects are pronounced in bone because of its high calcium content [99] and subsequent x-ray absorption [100]. Attempts to optimize corrections for beam hardening exist in clinical applications [99] and in industrial metrology applications [100-102]. Another study compared CT_L , oblique CT, and CT_T imaging of a human ankle prosthesis implanted in a pig stifle joint CT_T measurements were less accurate than CT_L measurements [103].

Measurements errors on models from μCT , including radius of curvature errors, were small and would be compatible with the design of conforming implants. By comparison, measurements errors associated with CT_L and CT_T were large, particularly radius of curvature measurements errors. The ML radius of curvature was more accurately evaluated than the CC radius of curvature. Additionally, the large percent errors demonstrated that although there was no measurement bias (mean differences were centered around zero), the magnitude of error was large, making measurements less reliable. The current resolution of CT_L and CT_T would not be compatible with the design of custom conforming arthroplasties nor would it be compatible with the evaluation of small topographic differences in small articular surfaces.

Although μ CT is of suitable accuracy, due to size limitations and radiation doses its use on live patients is limited. Currently, an 80mm bore *in-vivo* microCT can be purchased (Skyscan 1276, MicroPhotonics Inc, Allentown PA) which would be suitable for imaging a feline carpus; however, the use would be limited by the bore diameter. In utilizing computational methodologies to reduce the accuracy of the μ CT in order to bridge the gap between current clinical scanning and μ CT scanning, it was determined that a voxel edge length of 0.192 mm would be acceptable as there were no statistically significant differences between 0.024 mm, 0.048 mm, 0.096 mm and 0.192 mm. In addition to *in-vivo* MicroCT technologies, this resolution may also become available with incremental improvements to clinical CT scanning and post-processing which would be available for a wider variety of locations.

Several studies have evaluated the geometric aspects of the accuracy of CT. In a study comparing the accuracy of human tibiae models from CT scans (pixel size = 0.39 x 0.39 mm, slice thickness = 0.6 mm) and MRI scans compared to using optical laser scanning, mean RMSE for the entire bone was 0.55 mm and mean RMSE for the proximal and distal 10% of the bone were 0.64 and 0.65 mm, respectively [104]. These errors are approximately twice as large as RMSE errors reported for CT_L and CT_T in this study. Interestingly, an increase in bone size and a decrease in x-y pixel size did not improve accuracy. In one study where a calibration device with known dimensions was scanned using a slice thickness of 1 mm, mean geometric errors were 0.17 mm [105]. In another study using CT scan voxel size of 0.39 x 0.39 x 0.4 mm, CT scan accuracy of bones of the index finger had linear deviations of 0.21 mm in the distal phalanx, 0.20 mm in the middle phalanx, and 0.19 mm in the proximal phalanx [79]. These error

values are similar to the RMSE values obtained in this study. This is likely due to the fact that the phalanges have a size similar to the feline radius. A study of the accuracy of length measurements between anatomic landmarks of the spine using a CT scan slice thickness of 1 mm resulted in a mean global error of 1.1 ± 0.8 mm and length measure errors ranging from 0.8 to 2.4 mm [86]. These errors are larger than the errors reported in the current study.

CT parameters influence CT accuracy. In a study evaluating the accuracy of replicas of a canine femur, 3 models were additively manufactured from CT scan data collected using varying scan parameters and linear dimensions were compared using a touch probe CMM system [75]. A range of penetrability (80 to 140 kVp), tube current (60 to 160 mA), pitch (0.6 or 0.75), and several retro-reconstruction kernels and windows were used. The authors reported that 2 to 29% of the variability was due to differences in the model fabrication methods and 4 to 44% of the variability was due to differences in CT scan parameters. However, in that study, no direct measurements of the CAD models before manufacturing were collected. In the study evaluating CT accuracy of human phalanges, voxel size was constant (0.12 x 0.12 x 1 mm) but penetrability (80 to 140 kVp) and tube current (80 or 100 mA) varied [79]. However, segmentation thresholds and triangulation resolutions also varied, complicating the assessment of the influence of CT parameters on CT accuracy. The authors compared CT scans of the human phalanges to CT scans of the AM models of the phalanges; however, no comparison was made directly to the bone model. Higher penetrability values resulted in a decrease in the number of voxels present in the scan of AM models as compared to the scan of the bones, and an increase in tube current resulted in an increase in voxels

in the phalanges but not in the AM models. Increases in the lower bound for grayscale thresholding resulted in a reduction in the number of voxels that appeared in the AM model but not in the phalanges and increased the number of voxels in the phalanges but not in the AM models. Decreasing the lower threshold resulted in an increase in the number of voxels present in the phalanges but not in the AM models [76]. These changes illustrate the large influence that CT parameters and segmentation steps have on the accuracy of CT data.

Several previous studies used segmentation based on grayscale value filtering [75, 76]. Alternative segmentation strategies including Canney edge detection and intensity thresholding have been described. A study compared CT scans (0.39 x 0.39 mm pixel size, slice thickness = 0.5 mm) and 3D contact scans of ovine femurs [106]. Mean deviations were 0.24 mm for single threshold errors and 0.18 mm for multi-threshold errors. The deviations in that article were similar to the deviations reported in the current study. Based on the variety of scanning parameters and segmentation methods, acceptable scanning parameters and segmentation methods for modeling of small joint surfaces will likely require comprehensive standardization of CT scanning protocols, retro-reconstruction methods, and segmentation to optimize CT accuracy for specific regions of interest.

Optimizing CT accuracy is important if patient specific CAD data is used to design hemiarthroplasty implants. Increasing the conformity of a hemiarthroplasty has been shown to reduce friction and improve wear performance to nearly normal as compared to *in vivo* wear [107]. In hip hemiarthroplasty, under sizing the radius of a prosthetic head by as little as 0.75 mm (6.25%) negatively impacts the performance of

the hemiarthroplasty [78]. The large difference in maximum positive deviation and negative deviations and in ROC among modalities, warrants further investigation into the optimal data collection methods that accurately capture the articular surface of feline radiocarpal joints and other small joints.

1.6. Conclusion

Current clinical CT imaging and grayscale filtering segmentation methods used in this study do not have sufficient geometric accuracy for 3D CAD modeling of small articular surfaces. If clinical CT scanning technology could be improved it may be feasible to obtain high accuracy CAD models in small articular surfaces if the resolution was improved. Further development of streamlined protocols based around a total process approach including: resolution, scanning protocol, segmentation, and smoothing to optimize CT accuracy for CAD modeling small articular surfaces.

Chapter 2 – Ligament Fixation

2.1. Introduction

With the use of an endoprosthesis as previously described for osteosarcoma, fusion of the joint or total joint replacement have used mechanical features that replace the functions of ligaments and tendons. Hemiarthroplasty requires successful attachment of ligaments and tendons with good short and long-term strength. The reattachment of tendons or ligaments to bone can be done using sutures alone, bone anchors combined with sutures, blind or through bone tunnels or screws and washers which are often used as fixation devices. However, in a review of cruciate ligament repair methods, the current fixation methods are weak in the short term and care must be exercised during rehabilitation not to damage the construct [108]. Current attachment of ligaments and tendons to metals has had limited success. Initial strength of attachment was at best 47% immediately following surgery; however, 12 weeks following surgery strength was 99% of initial [109]. If initial attachment strength can be improved using additive manufacturing, detailed attachment designs can be developed to incorporate the features that contribute to short-term and long-term performance.

The use of metal clamps manufactured additively provides access to geometrical features that are not available in traditional subtractive manufacturing processes such as computer numerically controlled (CNC) machining or casting. These design capabilities could enable clamping systems with better performance. Additionally, success with additively manufactured ligament clamps would further support the use of custom patient specific property matched implants in the final hemiarthroplasty design

framework. The aim of this study is to compare the attachment strength and mechanical stiffness of three metal clamps to the native bone-ligament-bone construct.

2.2. Literature Review

One study evaluated the mechanical properties of carpal ligaments in quadrupeds. Mechanical testing was performed on 26 carpus sections of canine cadavers, resulting in eight specimens evaluated per ligament of interest. These ligaments included the medial collateral (MC), lateral collateral (LC), palmar ulnocarpal (PU), palmar radiocarpal (PR), accessorometacarpal-IV (AMC-IV), and accessorometacarpal-V (AMC-V) ligament. Specimens were pre-conditioned for 10 cycles at 2% strain, and tested at a strain rate of 0.5% until failure. Failure modes were described as midsubstance, bone-ligament interface, or bony avulsion. AMC-IV ligament failure was divided evenly among the groups, AMC-V failure occurred primarily at the bone-ligament interface, for other ligaments, the majority of the failures were midsubstance (Table 11) [110].

Table 11: Mechanical Properties of Canine Carpal Ligaments (Mean \pm SD) [110].

	AMC-IV	AMC-V	PR	PU	MC	LC
Modulus (MPa)	500-600 ¹	300-400 ¹	100-200 ²	100-200 ²	0-100 ³	0-100 ³
Failure Load (N)	426.15 \pm 100.79 ¹	602.54 \pm 165.22 ³	149.27 \pm 68.61 ²	414.66 \pm 721.29 ¹	392.45 \pm 132.61 ¹	233.11 \pm 144.86 ²

Within a row, values with different superscripts differed statistically ($p < 0.007$)

Anatomical differences in the canine and feline carpal medial collateral ligament (MCL) were highlighted in a comparative anatomic study. The MCL of the carpus in canines has two branches, one that connects the styloid process of the radius to the radial carpal bone, and another that connects the styloid process of the radius to the

palmar surface of the radial carpal bone. Unlike the canine MCL of the carpus, the feline MCL consists of a single ligament portion that connects to the radius in the dorsoproximal region and connects to the radial carpal bone in the palmarodistal region (Figure 10). The ligament angle was measured to be 80° from the longitudinal axis of the radius [111].



Figure 10: Feline Carpal MCL Anatomy [111].

During a dissection of three feline carpal joints, the abductor pollicis longus muscle tendon was severed, leaving only the joint capsule and carpal MCL intact. Joint stability was evaluated using palpation: instability was not detected. Palmar luxation resulted from simultaneous rotation and flexion of the carpal joint once the carpal MCL was severed. The authors conclude that the carpal MCL is the most important structure preventing palmar dislocation of the radiocarpal joint [111].

Literature regarding the management of carpal ligament injuries in cats is scarce. A case report of one feline patient with a ruptured carpal MCL due to a motor vehicle accident, a polypropylene figure-of-8 suture sling was anchored around two screws (one placed in the dorsomedial region of the radius and one placed in the palmaromedial region of the radial carpal bone). The angle of the polyethylene prosthesis was approximately 80° from the longitudinal axis of the radius. At 3 months after surgery,

flexion was observed to be 100° and gait, evaluated subjectively, was deemed normal [111]. Similarly, a cat presented with bilateral carpal injuries of which the right limb showed signs of a rupture of the medial collateral ligament. A Kirschner wire (K-wire) was used to anchor the radial carpal bone to the ulnar carpal bone. The ligament was replaced with braided polyester suture and anchored on the radius with a cortical screw and to the K-wire placed in the radial carpal bone. No lameness was reported at the final follow-up, 4.5 years after surgery [112].

The most common injuries to the cat carpus are due to falls from a height [113, 114] or motor vehicle accidents [115]. Multiple structures of the carpus are often affected. In these cases, the more common treatment for carpal joint injuries is a partial or a total carpal arthrodesis. In a review of the functional outcomes of carpal arthrodesis, seven of 20 patients had complications (n = 9 complications) including pin migration, pin malpositioning, plate loosening, and metacarpal fractures. Authors evaluated both radiographic outcomes between six and twelve weeks, and clinical outcomes after a minimum of six months. Long-term follow up questionnaires were only completed by the owners for 11 cases. In 10/11 patients, owners reported a decrease in the height of jump and 2/11 owners reported changes in their cats activities of daily living (primarily time outside). The authors reported that grooming was unaffected and running was slightly affected. The authors reported that 7/11 cats had excellent surgical outcomes [116].

Evaluations of ligament repair techniques are rare in cats. In a study of the repair of the talocrural joint in cat cadavers, a bone tunnel and polydioxanone ligament prosthesis method was evaluated for stability and range of motion using fixtures to

assist in consistent physical examination. No difference in joint stability was observed after reconstruction; however, statistically significant ($p < 0.05$) differences in joint range of motion were. Mechanical testing of strength was not performed [117].

Short-term strength is often limited when ligaments or tendons are reattached to bone. In one clinical study, three fixation methods for direct attachment of the canine supraspinatus tendon and bone attachment were evaluated for initial strength. The implants included a fixation plate (FP), a spiked washer (SW), and a custom tendon anchor (CTA) (Figure 11). The ultimate pull-out strength was weaker for the FP and SW than the CTA, except the custom tendon anchor with bone block attachment. The direct tendon attachment methods had ultimate pull out strengths that were 9.8, 8.6, or 23% of the intact specimen values for FP, SW and CTA, respectively. The bone block fixation methods had ultimate pull out strengths that were 15.3, 29.6 and 42 % of the intact specimen values for FP, SW, and CTA, respectively [118].

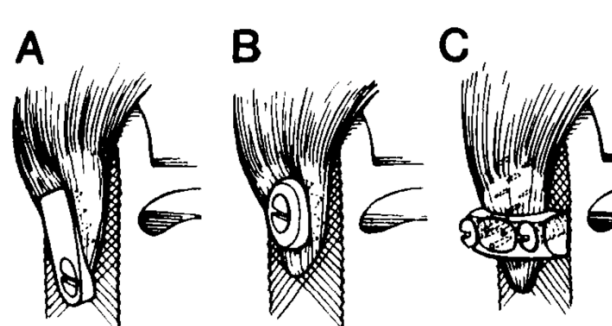


Figure 11: Tendon Attachment Devices: A) Fixation Plate, B) Spiked Washer, C) Custom Tendon Anchor [118].

Similar to the inclusion of the bone in the previous study, Inoue et al. evaluated the effects of including not only a bone plate but also additional cancellous bone graft to their custom tendon attachment prosthesis (Figure 12). Mixed breed dogs were operated on and the supraspinatus tendon was severed and reattached using the

prosthesis, and recovery was monitored for 16 weeks. Animals were then euthanized. At 16 weeks after surgery, weight bearing was 90% of the contralateral limb; however, the supraspinatus muscle volume was $85.5\% \pm 3.5\%$ of the contralateral side ($P < 0.008$). Mechanical testing was performed, and the ultimate tensile strength and stiffness were lower (44% and 43%). Previously, the authors achieved 61% and 44% (ultimate tensile strength and stiffness respectively) differences using an intact bone block with the prosthesis [119].



Figure 12: Custom Tendon Attachment Prosthesis [119].

Using the same implant as described above, Higuera et al. evaluated the custom tendon attachment prosthesis using recombinant human osteogenic protein-1 instead of cancellous bone and bone marrow. However, a significant improvement was not found [120].

In a larger study, the supraspinatus tendon from 40 dogs was reattached between two porous tantalum washers (Figure 13). Normal gait and ground reaction forces were observed three weeks after surgery, and ground reaction forces were not

significantly different from preoperative measures at three weeks and twelve weeks after surgery. The strength of the bone-tendon interface was tested after euthanasia. Strength and stiffness increased significantly ($P < 0.0014$, $p < 0.0299$ respectively) over 12 weeks of *in vivo* healing. Immediately after surgery, ultimate strength and stiffness were reported to be 39% and 47% of the intact specimen respectively. Three weeks after surgery the ultimate strength and stiffness were reported to be 67% and 62% of the intact specimen respectively, 6 week after surgery the ultimate strength was 99% and 94% of the intact specimen respectively, and 12 weeks after surgery, the ultimate strength and stiffness were 140% and 130% of the intact specimen, respectively. Tendinous tissue was observed to have grown through both sides of the washer 12 weeks after surgery [109].

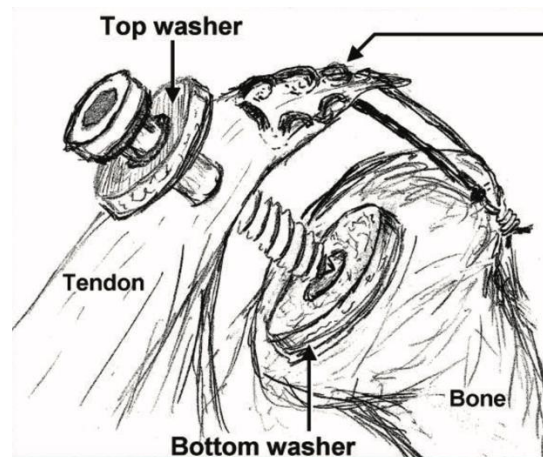


Figure 13: Porous Tantalum Washers for Tendon Attachment [109].

In a study using a similar porous tantalum washer in the canine patellar tendon one side of the washer was cemented to a created defect in the tibia (Figure 14). Ground reaction forces and volume of the quadriceps muscle returned to normal six weeks after surgery. Significant increases in failure force was observed at each time

point, 3 weeks after surgery, the mean \pm SD failure force was 66% \pm 12% of control, at 6 weeks after surgery the difference was 24% \pm 12%, and at 12 weeks after surgery the difference was 24% \pm 7%. Differences were significant ($P < 0.001$) between 3 and 6 weeks and between 3 and 12 weeks. Unlike the previous study there was no difference in the amount of tissue ingrowth and time since operation [121]. Unlike the previous study, cement was used and could have contributed to the differences in failure strength between the two studies.

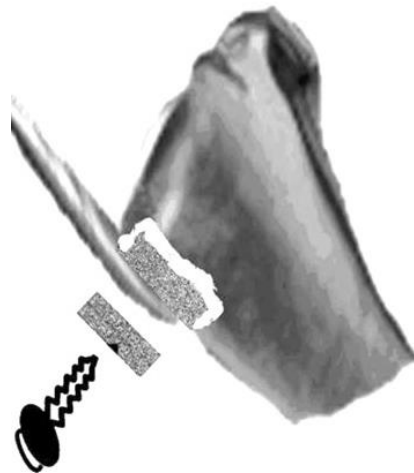


Figure 14: Porous tantalum washer for attachment of the canine patellar tendon [121].

2.3. Materials and Methods

This study used feline cadavers, which were euthanized for reasons unrelated to this research. The soft tissue of the distal region of the feline forelimb was surgically removed, and the medial collateral ligament was severed from the radius and attached to the additively manufactured clamp.

2.3.1. Clamping Surface Design

Three surface textures were evaluated for incorporation in the design of a hemiarthroplasty implant: 1) a flat *as manufactured* Ti6Al4V surface, 2) a ridged surface and 3) a spiked surface (Figure 15). Although, patterns like ridges are typically forged; additive manufacturing (AM) is an efficient way to integrate this type surface texture onto an implant. The clamps were additively manufactured to achieve the most efficient use of a small clamping surface. The ridged surface was selected due to its prevalence in gripping applications such as needle nose pliers. The ridged texture was designed with an extruded isosceles triangular profile. The base of the triangle was 0.45 mm and the height was 0.375 mm. The spiked design was selected based on its similarity to features found in literature. AM methods were used to efficiently achieve a high packing factor of structures on one part. The spiked texture was designed with a conical profile. The base circle had a diameter of 0.375 mm and the height was 0.375 mm. The clamping surface textures were designed to attach to a construct that mimics the shape of the distal region of the radius (Figure 16).

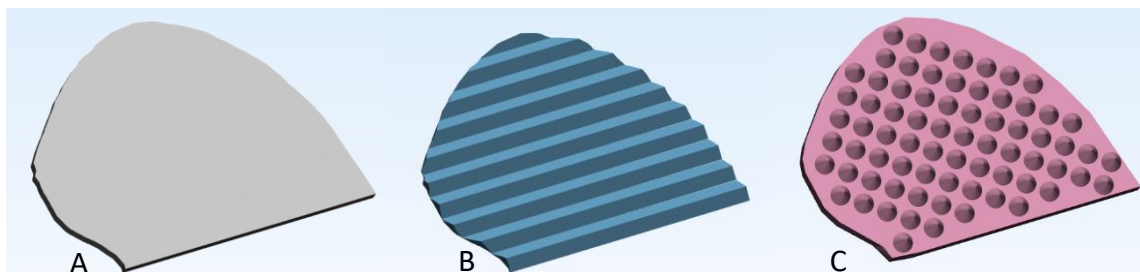


Figure 15: Clamping Surface Texture Designs A) Flat (as manufactured using SLM), B) Grooved, C) Spiked.

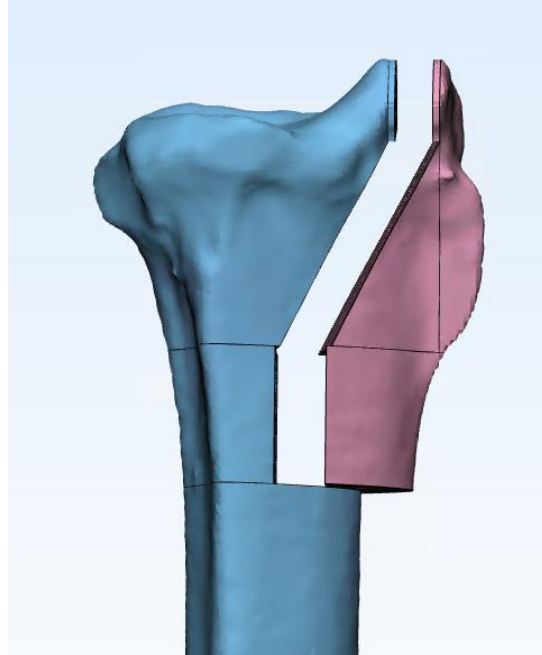


Figure 16: Ligament Clamp Design – Side A (pink), Side B (blue).

2.3.2. Clamping Surface Manufacturing

The clamping surfaces were built using Ti6Al4V (Ti, Al (5.5 - 6.75 wt %), V (3.5 – 4.5 wt. %)) powder (EOS GmbH, Munich, Germany) on the EOS EOSINT M280 with the standard Ti6Al4V build parameters (EOS GmbH, Munich, Germany). Clamping surfaces were oriented such that the clamping surfaces were built in the Z direction (Figure 17).

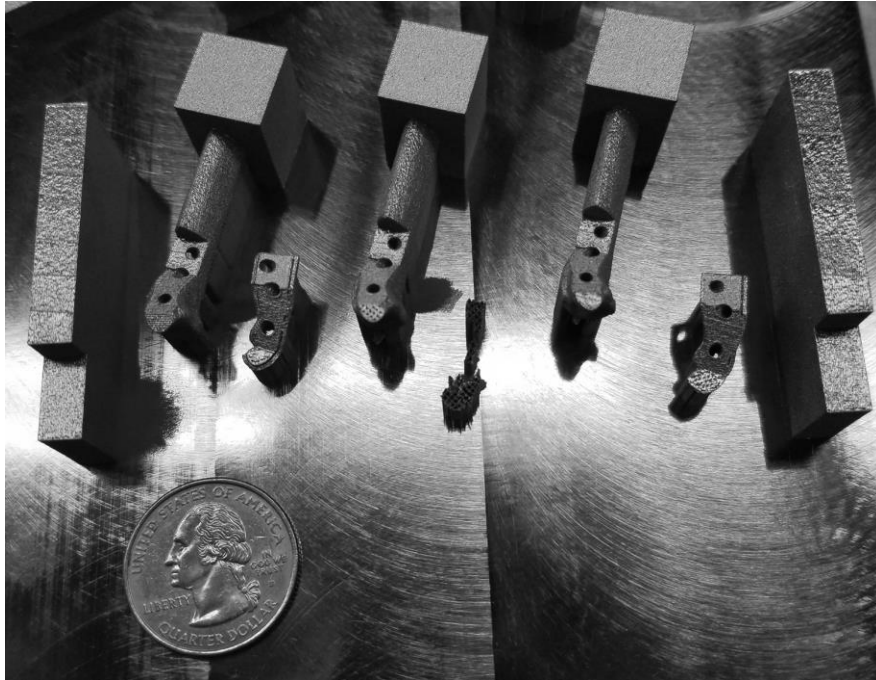


Figure 17: Build Orientation of Clamping Surfaces.

The clamps were removed from the build plate using a band saw and ultrasonically cleaned to remove debris without damaging the clamping surfaces. The implants were imaged under magnification and surface roughness average and mean roughness depth were calculated using a 3D digital microscope (KH 7700, Hirox, Hackensack, NJ) for all surfaces. Average Surface roughness was calculated at 70X magnification in three locations across the textured surfaces.

2.3.3. Experimental Method

The contralateral limbs of specimen used in this study were used for another study by our group that included being imaged with computed and microcomputed tomography, therefore, all limbs were confirmed to be skeletally mature. Forelimbs were harvested via scapular disarticulation with soft tissues intact and were wrapped in saline-impregnated gauze and were frozen at -20°C until dissection. The limbs were

thawed, and the radiocarpal ligament was isolated and harvested with a ≥ 5 -cm-long portion of the radius and the radial carpal bone. For control specimens, the ligament remained intact with the carpal bone and radius. For test specimens, the ligament was transected from its origin on the radius. Specimens not used immediately were re-frozen at -20°C with saline impregnated gauze until testing when they were thawed to room temperature.

Three control specimens were used for preliminary testing to determine the required relaxation time for the tissue. The specimens were loaded onto a universal test machine (Series 1600-CC, Applied Test Systems Inc., Butler PA) and a calibrated 250-lb maximum load cell with $\pm 1\%$ accuracy was used for testing. Specimens were loaded to 4.45 N and unloaded cyclically for 20 cycles to remove hysteresis in the tissue, and were then loaded to 4.45 N where the displacement was set and held constant for one hour (Table 12).

Table 12: Stress Relaxation Loading Protocol.

#	Action	Load	Time
1	Load	4.45 N	
2	Hold	4.45 N	1 sec
3	Unload	0N	
4	Hold	0N	1 sec
Repeat 1-4 for 20 Cycles			
5	Load	4.45 N	
6	Hold Displacement		60 min

Following the test the resulting load-vs-time curve was evaluated. A smoothing algorithm using a running average method was used to remove noise from the data, and the percent change was calculated from time = 0 every 5 minutes for the first 20 minutes and then every 10 minutes until the test ended at 1 hour (Table 13).

Table 13: Percent change w.r.t t=0.

Time (min)	5	10	15	20	30	40	50	END
Mean (%)	-26.22	-30.07	-32.53	-41.50	-36.43	-39.36	-40.28	-41.54
Stdev (%)	3.1	3.9	4.8	8.4	6.3	7.2	7.5	8.4

Eight specimens were evaluated in the control group, and seven specimens were evaluated in each test group: 1) no texture as manufactured clamp, 2) ridged texture as manufactured clamp, 3) spiked texture as manufactured clamp. Specimens were randomly assigned to each test group (Excel v. 15.32 , Microsoft, Redmond, WA). The shaft of the radii of control specimen was potted in an acrylic potting agent (Ortho-Jet BCA, Lang Dental, Wheeling, IL); The remaining specimens were clamped into the clamping surfaces 1.19N-m of torque. The specimens were loaded onto the machine and evaluated using the following protocol (Figure 18, Table 14)



Figure 18: Specimen loaded into ATS.

Table 14: Test Protocol.

#	Action	Load	Time	Rate
1	Load	4.45 N		25.4mm/min
2	Hold	4.45 N	1 sec	
3	Unload	0 N		25.4 mm/min
4	Hold	0 N	1 sec	
Repeat 1-4 for 20 Cycles				
5	Load	4.45 N		25.4 mm/min
6	Hold Displacement		30 min	
7	Load to Failure			25.4 mm/min

Load-displacement curves were outputted, and the maximum load was recorded. A line was fit to the linear portion of the load-displacement curve and the slope was recorded as the stiffness of the construct. A random complete block design statistical model was developed for the experiment. The residual effects were assumed to have a normal distribution with mean 0 and equal variance with respect to treatment. *P* values < 0.05 were considered significant.

2.4. Results

The clamping surfaces were imaged at 70X following manufacturing (Figure 19) and the average surface roughness (R_a) and root mean square error roughness (R_{RMS}) were calculated (Table 15).

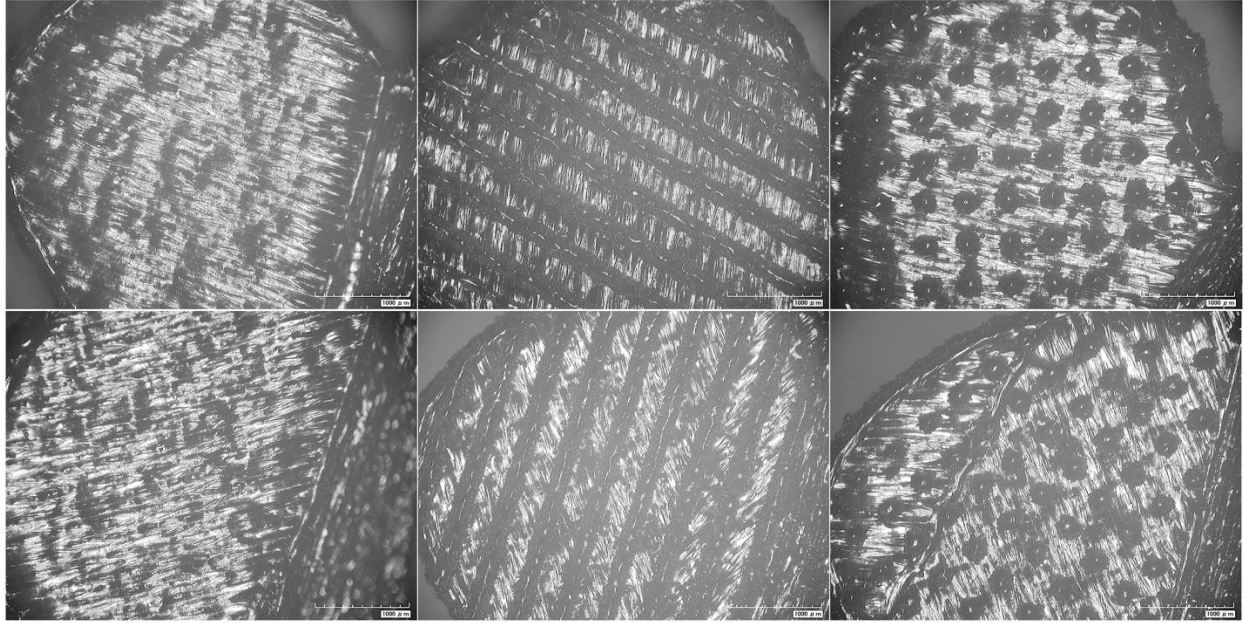


Figure 19: Top – Clamp Side A (Sm), Bottom – Clamp Side B (Lg). From left to right – No Texture, Ridged Texture, Spiked Texture.

Table 15: Mean \pm Standard Deviation of Surface Roughness (n=3 per specimen).

Texture - Side	Average Roughness ($R_a, \mu\text{m}$)	Average Root Mean Square Roughness ($R_{RMS}, \mu\text{m}$)
Flat - A	15.65 \pm 2.69	19.26 \pm 2.46
Flat - B	13.89 \pm 4.28	16.06 \pm 4.78
Ridged – A	90.30 \pm 16.83	102.54 \pm 18.69
Ridged – B	66.47 \pm 2.49	78.68 \pm 3.99
Spiked – A	65.12 \pm 2.25	75.75 \pm 2.25
Spiked – B	31.53 \pm 1.78	38.18 \pm 3.52

The maximum load was recorded and stiffness of the specimen was calculated by fitting a line to the linear portion of the load displacement curve (Figure 20 - Figure 23, Table 16). One specimen from each clamp group was lost during initial test setup or during the cyclic loading prior to the stress relaxation phase and was excluded from the results. Full Data and ANOVA plot can be found in Appendix D.

Table 16: Mean \pm Standard Deviation of Maximum Load and Construct Stiffness.

	Maximum Load (N)	Stiffness (N/mm)
Control (n = 8)	122.55 ^A \pm 65.26	26.65 ^C \pm 9.49
No Texture – As Manufactured Clamps (n = 6)	14.46 ^B \pm 7.25	13.87 ^D \pm 4.38
Ridged Texture – As Manufactured Clamps (n = 6)	25.44 ^B \pm 14.99	19.86 ^{C,D} \pm 6.97
Spiked Texture – As Manufactured Clamps (n = 6)	55.83 ^B \pm 6.25	15.30 ^D \pm 5.76

Within a column, mean values with different superscripts differ statistically ($P < 0.05$).

The maximum load was significantly higher for the control group than for any of the test groups, and although the spiked texture group had the highest mean, the differences between the clamped groups were not significant. The stiffness of the construct was highest again for the native ligament control group; however, the ridged clamp had no significant difference with the control group.

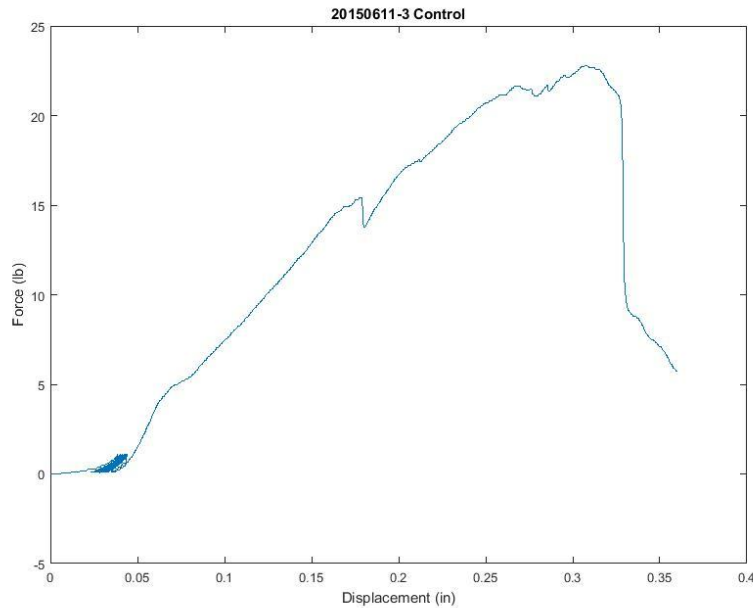


Figure 20: Representative Load vs. Displacement Curve – Control Specimen.

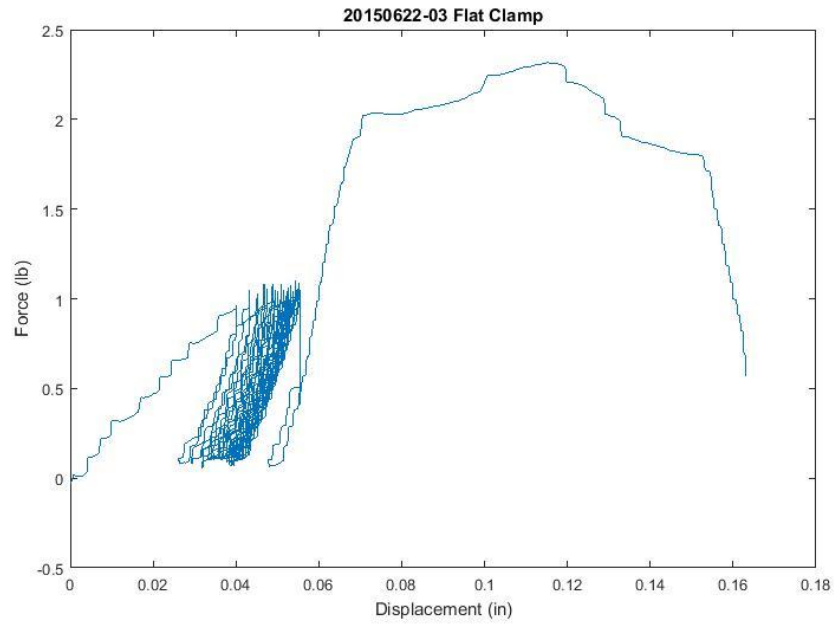


Figure 21: Representative Load vs. displacement curve: no texture as manufactured specimen.

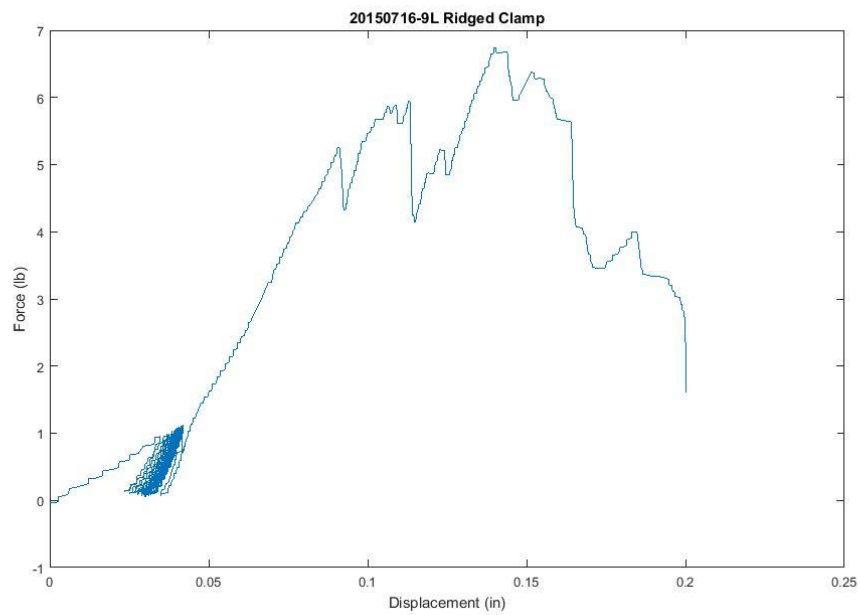


Figure 22: Representative Load vs. displacement curve: ridged texture as manufactured specimen.

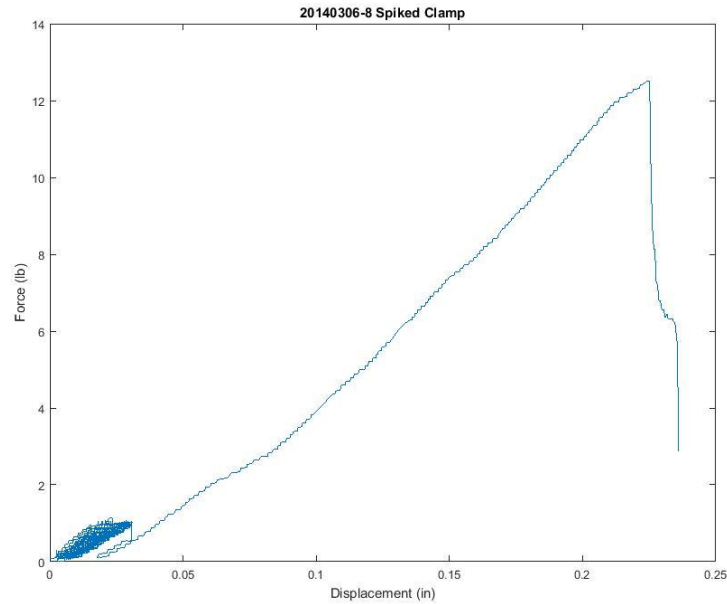


Figure 23: Representative Load vs. displacement curve: spiked texture as manufactured specimen.

The maximum load varied from between 11.8% of the control for the no texture as manufactured clamp group, and as high as 45.5% for the spiked texture as manufactured clamp group. The ridged texture as manufactured clamp group reached 74.5% of the control value for stiffness (Table 17).

Table 17: Maximum Load and Stiffness as a percentage of control specimen values.

	Maximum Load	Stiffness
No Texture – As Manufactured Clamps (n = 6)	11.8%	52.1%
Ridged Texture – As Manufactured Clamps (n = 6)	20.8%	74.5%
Spiked Texture – As Manufactured Clamps (n = 6)	45.5%	57.4%

2.5. Discussion

In this study, the maximum load and stiffness of additively manufactured ligament clamp designs for the feline medial collateral ligament (MCL) were evaluated for their initial pull out properties. The maximum load of the ligaments attached to additively

manufactured clamps perform similarly to published works (Table 18). When compared to designs Lit-1, Lit-2, and Lit-3, all additively manufactured clamping surfaces outperformed designs Lit-1 and Lit-2. The ridged texture surface performed similarly to Lit-3, and the spiked texture outperformed Lit-3 substantially. Only the spiked texture outperformed Lit-6. The use of bone graft or intact bone blocks appears to improve the initial pull out strength of ligament and tendon attachment methods, and none of the proposed designs were able to outperform Lit-5.

Table 18: Maximum Load as a percentage of normal / control of ligament and tendon attachment designs.

Identification	Ligament of Interest	Clamp Design	Maximum load as a Percentage of Normal / Control (%)
Lit -1	Canine Supraspinatus Tendon	Fixation Plate [118]	9.8
Lit - 2	Canine Supraspinatus Tendon	Spiked Washer [118]	8.6
Lit - 3	Canine Supraspinatus Tendon	Custom Tendon Anchor [118]	23
Lit - 4	Canine Supraspinatus Tendon	Large spikes on Mesh Structure with cancellous bone graft [119]	44
Lit - 5	Canine Supraspinatus Tendon	Large spikes on Mesh Structure with intact bone block [119]	61
Lit -6	Canine Patellar Tendon	Porous Tantalum Washer [109]	39
Present Study	Feline Medial Collateral Ligament	No Texture as Manufactured	12
Present Study	Feline Medial Collateral Ligament	Ridged Texture as Manufactured	21
Present Study	Feline Medial Collateral Ligament	Spiked Texture as Manufactured	46

Therefore, the results suggest that additively manufactured clamping surfaces could be used in future hemiarthroplasty designs. Although a substantial difference in maximum load between the control and test groups was observed, the use of additively manufactured clamps in hemiarthroplasty provides initial stability. Additionally, additively manufactured clamps provide flexibility in design that is not available with traditional

processing methods. The ability to achieve 46% strength as compared to normal initially with a spiked design and 75% of normal stiffness with the ridged design. These clamping features could be combined and a porous structure could be added underneath the texture to promote long-term fixation strength as demonstrated by the high strength and stiffness measures after healing with a porous tantalum washer. This study aimed to determine the effects of different surface textures on load and stiffness immediately following attachment of the ligament. Limitations of this study include and small feature sizes of the feline model.

2.6. Conclusions

The initial hypothesis that one of the clamp designs selected would be suitable for use on a hemiarthroplasty in the distal region of the radius in a feline model was rejected due to the substantial difference in maximum loads and stiffness results to the control group when attached in the design clamp. The spiked surface texture experienced the highest maximum load at 46% of the control group, and the ridged surface texture demonstrated the highest initial stiffness at 75% of the loads demonstrated by the control group. Pull out forces were not substantially different than other reported clamping mechanisms; therefore, it is likely that clamping surface design has a much larger impact on the pull out loads of a ligament to a clamping connection site than manufacturing method. In the future, using additive manufacturing to optimize the clamping design using both short term and long term ligament fixation features would allow for initial stability as well as long term strength.

Chapter 3 – Polymer Bearing Surface Selection

3.1. Introduction

A critical component of hemiarthroplasty are the properties of the bearing surface. Historically, hemiarthroplasty implants have had either metal bearing surfaces or ultra high molecular weight polyethylene (UHMWPE) bearing surfaces [7, 43, 45-50]. With the increase in the development of tailored polymeric biomaterials, property matching the bearing material to the material properties of articular cartilage is within reach. The wear properties of polyurethane (PU) and polyvinylalcohol (PVA) hydrogels have been extensively studied and have been found to have favorable wear characteristics when articulating against cartilage. Additional properties have been studied on flat test pieces; however, for these materials to be utilized in hemiarthroplasty they must match the curvature of the portion of the bone that was removed. This study looks to characterize the compressive properties of two advanced polymer materials with custom patient specific geometries for both the polymer replacing the bearing surface of the distal region of the radius and the radial-carpal bone.

3.2. Literature Review

The selection of an appropriate weight-bearing surface material for hemiarthroplasty implants requires an understanding of the specific anatomic, physiologic, and mechanical properties of the cartilage that contacts the bearing material of the hemiarthroplasty implant. There are three main types of cartilage in the body: fibrocartilage, elastic cartilage, and hyaline cartilage. Fibrocartilage is found where ligaments and tendons attach to bone, and elastic cartilage makes up the

cartilage in the human ear and nose. Hyaline cartilage, commonly referred to as articular cartilage, is the type of cartilage found in joints.

Hyaline cartilage contains chondrocytes and an extra cellular matrix (ECM) composed of collagen, proteoglycans, non-collagenous proteins, and fluid. The majority of the volume of articular cartilage and chondrocytes represent 1% of that volume. Although five main types of collagen are present in cartilage the majority of the collagen found in the ECM is type-II collagen. The tensile properties of the cartilage come from the intertwined fibrils created by the type-IX, type-XI and type-II collagen. Proteoglycan aggregates contribute to the recovery and stress distribution properties of hyaline cartilage through the attraction and prevention of water diffusion during loading. The fluid found in cartilage, which makes up 80% of the wet weight, gives cartilage its resistance and compressive properties found in no other tissue or artificial material [122].

The anatomic structure of cartilage can be represented by four distinct zones, each containing three regions. From the outermost region, the four zones are the superficial zone, the transitional (middle) zone, the deep (radial) zone, and the calcified zone (Figure 24) [122, 123].

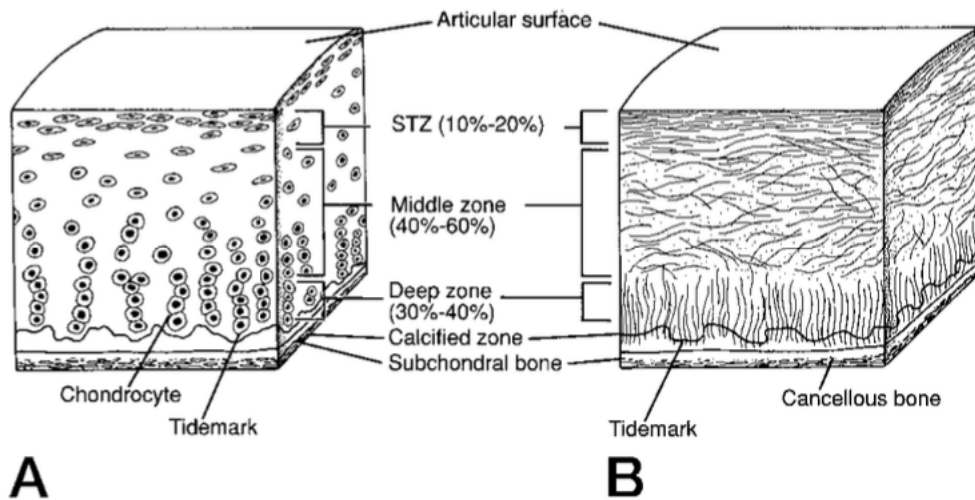


Figure 24: Arrangement of articular cartilage zones as illustrated by Newman. A) chondrocyte placement and orientation, B) collagen fiber placement and orientation [123].

The superficial zone is the thinnest and consists of a laminar layer of collagen fibers, and below the collagen fibers, a layer of flattened chondrocytes [123]. In addition to the structure of the ECM and chondrocytes, the superficial zone has less proteoglycan, large amounts of water and large amounts of fibronectin. This cellular and extracellular matrix structure provides resistance to shear stresses as well as compressive strength [122]. The middle zone contains chondrocytes that are more spherical and the fibers are oriented much more randomly [122, 123]. In the deep (radial) zone, the chondrocytes are spherical and oriented into columns. The matrix fibers are oriented perpendicular to the surface and have the largest diameter. This zone contains the least amount of water and the greatest number of proteoglycans [122]. In the deepest zone, named the calcified cartilage zone, collagen fibrils actually insert into the subchondral bone, serving as anchors and a transition. The shear stresses experienced in this region are the highest of any of the zones because of the

stark difference in properties between the hyaline cartilage and the subchondral bone [122].

Several studies published have compared the anatomy of articular cartilage across mammalian species including human, canine, and feline. The thickness of articular cartilage has been reported as proportional to body weight or mass [124-126]. In the femoral condyle the cartilage thickness was reported (mean \pm SD) as 2.26 ± 0.49 mm for humans, 0.67 ± 0.28 mm for dogs, and 0.327 ± 0.150 mm for cats [124]. Additional measures include cartilage thickness from the human humeral head (1.56 ± 1.32 mm) and canine humeral head (0.68 ± 0.12 mm) as well as from the human metatarsal (1.50 ± 1.02 mm) and feline metatarsal (0.138 ± 0.037 mm) [124]. In a study of the thickness of articular cartilage across mammalian species including human and dog at the proximal medial trochlear, lateral trochlear, distal medial trochlear, proximal medial condyle and distal medial condyle of the knee / stifle, the authors reported an average thickness across locations of 0.6 to 1.3 mm for dogs and 2.2 to 2.5 mm for humans. The authors conclude that the closest match to human articular cartilage in the knee of the species tested (human, horse, goat, dog, rabbit, sheep) is the horse followed by the goat [126]. In a study comparing the articular cartilage of 58 mammalian species including humans and beagles (dog), the authors report increases in thickness with an increase in body mass, a decrease in cellular density with decreasing body mass, and a consistent biomechanical composition [125].

Although the general anatomy and structure of articular cartilage is consistent, cartilage thickness varies both between and within joint surfaces. Shepherd et al. evaluated the variation in human cartilage thickness on the acetabulum, femoral head,

distal aspect of the femur, proximal and distal aspects of tibia, and talus. Cartilage thickness was measured by piercing the surface of the articular surface with a sharp needle [127]. Cartilage thickness in each joint differed significantly ($p < 0.001$) between all pairs except between the ankle and hip. However, the influence of body weight, body mass index, height, and gender on cartilage thickness were not evaluated in the study [127]. Thickness information should be considered for specific regions of interest when developing tissue engineered cartilage replacements in load bearing joints as the data presented by Shepherd et al. shows. Additionally, thickness could play a role in variation in material properties of cartilage that will be presented in following sections.

Once the histologic structure of articular cartilage is understood, it follows that the material properties of healthy articular cartilage should be evaluated as a gold standard target for materials that directly interact in a load bearing manner with articular cartilage. The functional requirements of articular cartilage are two-fold: 1) reduce contact stresses and 2) allow motion within a joint in minimal friction conditions with minimal wear [128]. Cartilage material properties are most often broken into two categories, the properties of the cartilage extracellular matrix, and material properties associated with the biphasic viscoelastic nature of the cartilage tissue including fluid, extracellular matrix and chondrocytes. Additionally, cartilage tissues have an exceptionally low coefficient of friction that should be considered when developing a material that will be in direct loading contact with articular cartilage.

The information about material properties of feline articular cartilage is sparse; however, in many other species the properties of articular cartilage have been studied extensively. In a study of the material properties of feline cartilage in the knee, the

thickness was studied *in situ* across the tibia (medial plateau and lateral plateau), femur (medial condyle, lateral condyle, patellar groove), and patella. Thickness values (mean \pm SD) ranged from 0.181 ± 0.016 mm in the patellar groove to 0.518 ± 0.153 mm in the medial tibia plateau. A biphasic creep indentation test was used to obtain permeability and stress relaxation data. A finite element fit of the stress relaxation data was used to obtain an effective elastic modulus. Permeability and effective modulus were reported as a single value averaged across all test sites where effective elastic modulus was 0.53 ± 0.37 MPa and permeability was $0.66 \pm 0.32 \cdot 10^{-3}$ mm⁴/(N*s) [129].

The material properties of distal femoral cartilage in five species used biphasic creep indentation to obtain intrinsic material properties by non-linear regression curve fitting and a needle probe was used to measure thickness (Table 19). Properties in the primary load bearing regions (medial and lateral condyles) vary from those in the patellar groove, and the smaller porosity ratio and higher permeability of the tissue in the patellar groove means that fluid can move more freely through the tissue and the tissue can compress more quickly [128].

Table 19: Intrinsic Material Properties of Distal Femoral Articular Cartilage [128].

Species	Location	Poisson's ratio	Aggregate Modulus	Permeability $10^{-15} \text{ m}^4/\text{N}\cdot\text{s}$	Thickness (mm)
Human	Lateral Condyle	$0.098 \pm 0.069^{\text{a}}$ ₁	$0.701 \pm 0.228^{\text{a}}$ ₁	$1.182 \pm 0.207^{\text{a}}$ ₁	$2.31 \pm 0.53^{\text{a}}$ ₁
	Medial Condyle	$0.074 \pm 0.084^{\text{a}}$ ₁	$0.588 \pm 0.114^{\text{a}}$ ₁	$1.137 \pm 0.160^{\text{a}}$ _{1, 2, 3}	$2.21 \pm 0.59^{\text{a}}$ ₁
	Patellar Groove	$0.000 \pm 0.000^{\text{a}}$ ₁	$0.530 \pm 0.094^{\text{a}}$ ₁	$2.173 \pm 0.730^{\text{a}}$ _{1, 2}	$3.57 \pm 1.12^{\text{a}}$ ₁
Bovine	Lateral Condyle	$0.396 \pm 0.023^{\text{a}}$ ₂	$0.894 \pm 0.293^{\text{a}}$ ₂	$0.426 \pm 0.197^{\text{a}}$ ₂	$0.94 \pm 0.17^{\text{a}}$ ₂
	Medial Condyle	$0.383 \pm 0.047^{\text{a}}$ ₂	$0.899 \pm 0.427^{\text{a}}$ _{1, 2}	$0.455 \pm 0.332^{\text{a}}$ ₁	$1.19 \pm 0.24^{\text{b}}$ ₂
	Patellar Groove	$0.245 \pm 0.065^{\text{b}}$ ₂	$0.472 \pm 0.147^{\text{b}}$ ₁	$1.422 \pm 0.580^{\text{b}}$ ₁	$1.38 \pm 0.19^{\text{b}}$ ₂
Dog	Lateral Condyle	$0.300 \pm 0.075^{\text{a}}$ ₃	$0.603 \pm 0.237^{\text{a}}$ _{1, 2}	$0.774 \pm 0.563^{\text{a}}$ _{1, 2}	$0.58 \pm 0.20^{\text{a}}$ ₃
	Medial Condyle	$0.372 \pm 0.050^{\text{a}}$ ₂	$0.904 \pm 0.218^{\text{b}}$ ₂	$0.804 \pm 0.776^{\text{a}}$ _{1, 2}	$0.90 \pm 0.15^{\text{b}}$ ₃
	Patellar Groove	$0.093 \pm 0.067^{\text{b}}$ _{1, 2}	$0.555 \pm 0.144^{\text{a}}$ ₁	$0.927 \pm 0.844^{\text{a}}$ ₁	$0.52 \pm 0.12^{\text{a}}$ ₃
Monkey	Lateral Condyle	$0.236 \pm 0.044^{\text{a}}$ ₁	$0.778 \pm 0.176^{\text{a}}$ _{1, 2}	$4.187 \pm 1.545^{\text{a}}$ ₃	$0.57 \pm 0.12^{\text{a}}$ ₃
	Medial Condyle	$0.236 \pm 0.055^{\text{a}}$ ₃	$0.815 \pm 0.180^{\text{a}}$ _{1, 2}	$2.442 \pm 1.129^{\text{a}}$ ₃	$0.72 \pm 0.09^{\text{a}}$ ₄
	Patellar Groove	$0.197 \pm 0.123^{\text{a}}$ ₂	$0.522 \pm 0.159^{\text{b}}$ ₁	$4.737 \pm 2.289^{\text{a}}$ ₂	$0.41 \pm 0.05^{\text{b}}$ ₄
Rabbit	Lateral Condyle	$0.337 \pm 0.092^{\text{a}}$ _{2, 3}	$0.537 \pm 0.258^{\text{a}}$ _{1, 2}	$1.806 \pm 1.049^{\text{a}}$ ₁	$0.25 \pm 0.06^{\text{a}}$ ₄
	Medial Condyle	$0.197 \pm 0.094^{\text{b}}$ ₃	$0.741 \pm 0.101^{\text{a}}$ _{1, 2}	$2.019 \pm 1.621^{\text{a}}$ _{2, 3}	$0.41 \pm 0.10^{\text{b}}$ ₅
	Patellar Groove	$0.206 \pm 0.126^{\text{b}}$ ₂	$0.516 \pm 0.202^{\text{b}}$ ₁	$3.842 \pm 3.260^{\text{a}}$ ₂	$0.20 \pm 0.04^{\text{a}}$ ₅

Within a column, values with different alphabetic superscripts differ significantly ($p < 0.05$) within a species, and values with different numeric superscripts differ significantly ($P < 0.05$) between species within a location.

In an analysis of the differences in properties over regions of the human femoral head and acetabulum, automated biphasic indentation testing was used to obtain material properties and a needle probe system was used to measure thickness. The aggregate modulus ranged from 1.98 ± 0.245 MPa to 0.679 ± 0.162 MPa on the femoral head, and 1.072 ± 0.546 MPa to 1.424 ± 0.602 MPa on the acetabulum. The poisson's ratio ranged from 0.013 ± 0.028 to 0.058 ± 0.074 on the femoral head and $0.011 \pm$

0.022 to 0.055 ± 0.075 on the acetabulum. Permeability ranged from $0.781 \pm 0.450 \times 10^{-15} \text{ m}^4/\text{N}\cdot\text{s}$ to $1.101 \pm 0.610 \times 10^{-15} \text{ m}^4/\text{N}\cdot\text{s}$ on the femoral head and $0.710 \pm 0.362 \times 10^{-15} \text{ m}^4/\text{N}\cdot\text{s}$ to $1.133 \pm 1.114 \times 10^{-15} \text{ m}^4/\text{N}\cdot\text{s}$ on the acetabulum. The thickness ranged from $1.03 \pm 0.16 \text{ mm}$ to $1.84 \pm 0.17 \text{ mm}$ on the femoral head and $1.06 \pm 0.24 \text{ mm}$ to $1.83 \pm 0.45 \text{ mm}$ on the acetabulum. [130]. Biphasic indentation is commonly used to obtain the material properties of cartilage; however, other methods exist such as confined and unconfined compression. A comparison of the three methods was performed using a bovine model with specimen from the humeral head, patella and femoral medial condyle. The Young's modulus was significantly higher in all regions for indentation testing than for confined and unconfined compression testing [131].

In a review of human articular cartilage the permeability was on average between 10^{-16} to $10^{-15} \text{ m}^4/\text{N}\cdot\text{s}$, the compressive aggregate modulus was between 0.08 and 2 MPa, the Young's modulus in tension varied with depth between 5 and 25 MPa, and the solid phase of the tissue has a shear modulus between 0.05 and 0.25 MPa [132]. The coefficients of friction found in Table 20 below are listed for various species and range from 0.002 in the bovine shoulder to 0.35 in the porcine shoulder [133].

Table 20: Coefficient of friction in articular cartilage for various species [133].

Species	Coefficient of Friction
Human Knee	0.005 – 0.02
Porcine Shoulder	0.02 – 0.35
Canine Ankle	0.005 – 0.01
Human Hip	0.01 – 0.04
Bovine Shoulder	0.002 – 0.03

Typically, hemiarthroplasty bearing materials have primarily been metals [7, 46, 56]: cobalt chrome [51-54], titanium [134, 135] or stainless steel [57]. Wear following hemiarthroplasty has been a concern particularly with the use of metals as implant

bearing surfaces. In the human hip, biopsies were performed on the superior aspect of the acetabulum from patients who were having a revision of hemiarthroplasty implants due to pain and from patients who were receiving their first hemiarthroplasty implant (control). Authors histologically evaluated the biopsies and found a significant ($P<0.001$) relationship between the amount of cartilage degradation and the length of time the implant was in place. Additionally, although severe degradation to the cartilage was found in the cartilage of all specimens whose prosthesis had been in place less than 5 years, in patients who had prostheses in place for more than 5 years hyaline cartilage was largely absent. No differences were found between unipolar or bipolar hemiarthroplasty implants [136].

In an ovine model, wear following hemiarthroplasty was evaluated using cobalt chrome as the bearing material. Although, in the sixteen weeks following implantation cartilage wear in each direction was no more than 1mm, at the time of euthanasia there was visually evident cartilage erosion on all specimen. Safranin O stained specimen in load bearing regions were rarely normal (medial and dorsal); however, in infrequent loading regions there were more frequent sections with normal staining (cranial and caudal) [137].

Several studies have explored alternative materials for hemiarthroplasty. In a clinical case study, a patient received an acrylic hemiarthroplasty of the femur. After a 45 year follow-up, the patient reported only mild hip pain that did not interfere in daily life; however, the authors note that these results are unusual based on the poor biocompatibility and fixation strength [138]. In a long-term study of a polyvinyl alcohol hydrogel implant (Cartiva Synthetic Cartilage Implant; Cartiva Inc., Alpharetta GA) for

hallux rigidus, patients who received the hydrogel hemiarthroplasty were compared to patients who received first metatarsophalangeal fusion. Two years after surgery both groups had no significant differences in pain or functional outcomes. Five years after surgery, the implant survivorship was 96%, and patients had statistically significant improvements as compared to preoperative measures of pain, function, and range of motion. X-rays taken showed no signs of implant loosening or wear [139]. A hemiarthroplasty implant with a pyrolytic carbon bearing surface on a graphite head with titanium stem was used in 10 patients with femoral neck fractures, and seven patients with osteonecrosis. In patients with femoral neck fracture, 1/10 underwent conversion to total hip arthroplasty (THA) at 6.5 years post-op; however, in the osteonecrosis group all living patients 6/7 underwent revision due to pain. Five-of-seven patients underwent conversion to THA between six and 51 months (mean 22.2), and one patient converted to THA 55 months following the initial surgical procedure. The cartilage at all conversions had thinned, and all but one femoral stem was stable [140]. In a retrospective review of 134 bipolar femoral hemiarthroplasty implants with metal bearing surfaces, the mean degeneration rate as determined radiographically was 0.34 ± 0.35 mm/yr. [141].

In a rabbit knee model, authors compared human phalangeal hemiprosthesis with cobalt chromium, ceramic (ZrO_2), or pyrocarbon bearing surfaces. Following surgery, animals were monitored for 12 weeks, and at the time of euthanasia one animal in the ceramic and pyrocarbon groups still exhibited minor limping. Biphasic indentation testing was performed and all groups showed significant differences when compared to the normal articular cartilage on the contralateral side. Additionally, the histological

evaluation using the Mankin score resulted in better scores (less damage) for CoCr group than the ceramic and pyrocarbon groups. This difference was significant between the CoCr and ceramic group ($P < 0.011$) [142].

The use of tribology to evaluate the properties of materials and cartilage in contact and relative motion provide the most direct way to evaluate the suitability of a biocompatible material for load bearing surface contact with articular cartilage. A review of advances in cartilage biotribology from 1988 to 2008 by Katta et al. highlights the common methods of *in vitro* tribologic evaluation which include pendulum friction simulators, arthrotripsometers, robotic arms under force control, atomic force microscopy, surface force apparatus, with the most common being pin-on-disk. Common methods of evaluating wear include wear debris analysis, optical surface analysis, and microMRI [143]. Because of the biphasic nature of cartilage, careful consideration of the parameters that affect rehydration is critical. The authors reported that in pin-on-disk setup, sliding velocities between 1 mm/s and 4 mm/s are adopted to simulate *in vivo* conditions. Additionally, the lowest coefficients of friction were found when the stroke length allowed for a minimum of 45% of the tissue to be available for rehydration. In a compilation of data from seven studies that utilized a neutral solution such as phosphate buffered saline, if 70% of the area in the articulating zone or less was loaded, low coefficient of friction values were reported [143].

In an *in vitro* simulation of the effect of radial clearance on wear was evaluated using a pendulum friction simulator (n=6), and two-dimensional profilometry was used to evaluate cartilage deformation and volume change; however, only three specimens for each clearance group was evaluated. Peak contact stress values increased from 5.6

MPa in the group when clearance was less than 0.6 mm to 10.6 MPa when clearance was > 1.8 mm. The coefficient of friction increased with test duration and significant differences were reported to be significantly lower ($P<0.05$) for clearances greater than 1.8 mm as compared to all other groups (Figure 25). Cartilage deformation was greatest in specimen with clearances less than 0.6 mm or greater than 1.8 mm [144].

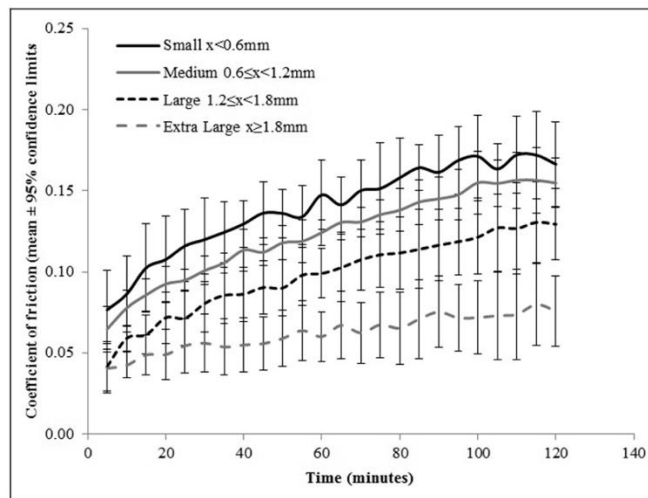


Figure 25: Coefficient of friction over time during pendulum friction test [144].

In a tribological study evaluating the effects of the level of conformity in hemiarthroplasty, authors used a pendulum friction simulator to evaluate contact stress, friction, and cartilage degeneration in a bovine knee model. Articular cartilage of the distal region of the femur was articulated against the tibial articular cartilage with the meniscus intact as the control. Additional test groups included a flat stainless steel plate, a curved stainless steel plate with a radius of 100 mm and a curved stainless steel plate with a radius of 50 mm, which most closely resembles the curvature of the tibial plateau with meniscus. The coefficient of friction decreased at both the 1000 N

peak loading and 250 N peak loading condition as the conformity of the plate increased. Additionally, friction shear stress, average peak contact stress, and wear volume exhibited similar trends [145]. Using a pendulum motion simulator for the hip, Muller et al. evaluated hip hemiarthroplasties with aluminum oxide ceramic or steel bearing surfaces on porcine and human specimen. The lubricant used was a 1:3 ratio of calf serum and Ringer's lactate solution. The measured mean coefficient of friction started at 0.017 and increased to 0.082 following 900 cycles for the ceramic bearing surface, and started at 0.020 and increased to 0.101 for the metal bearing surface in the porcine specimen. In human specimen, the friction coefficient started at 0.017 and increased to 0.083 for the ceramic bearing surface and started at 0.019 and increased to 0.118 for metal bearing surface [146]. In another study looking at a ceramic bearing material, Patel et al. evaluated the use of a zirconium bearing surface with an oxidized layer of about 7 μm using a pin-on-disk testing apparatus. The authors reported no significant difference in the wear of cast cobalt-chrome and oxidized zirconium [147].

Using a reciprocating sliding motion on a pin-on-disk tester, Chan et al. evaluated the wear properties of Cobalt Chrome (CoCr), alumina (Al_2O_3), UHMWPE, and stainless steel against bovine articular cartilage. Additionally, authors used atomic force microscopy to calculate the friction coefficient and surface roughness of the biomaterials. UHMWPE had the lowest coefficient of friction at both the 1 minute, 0.035 ± 0.001 , and 1 hour time point, 0.391 ± 0.012 , alumina had the highest coefficient of friction at the 1 minute, 0.134 ± 0.003 , and cobalt chrome had the largest increase in the coefficient of friction from 0.074 ± 0.003 to 0.566 ± 0.013 . The surface roughness of the materials did not change after testing against articular cartilage [148].

Significant effort into the development of biomaterials as articular cartilage replacement materials is ongoing. Hydrogels have been the focus of a substantial portion of this development work. In a review of the properties of polyvinyl alcohol (PVA), the coefficient of friction was reported to be between 0.04 and 0.07 and shear stress modulus was reported to be 0.28 to 0.54 MPA for a 40% PVA hydrogel matrix. These properties were similar to the reported values for articular cartilage (<0.01 to 0.05 for coefficient of friction and 0.28 to 0.54 MPa for shear modulus). Biocompatibility of PVA hydrogels have demonstrated biocompatibility in a variety of medical applications. Additionally, authors reported that a thickness of 2-3 mm was sufficient for load bearing. [149]. The effects of continuous or dynamic loading on the wear of human femoral articular cartilage on articular cartilage, PVA, or stainless steel were evaluated by Li et al. In continuous sliding, the friction coefficient did not change for cartilage-on-cartilage, and increased for both cartilage-on-stainless steel or cartilage-on-PVA hydrogel; however, in dynamic loading the PVA hydrogel only exhibited a small rise in coefficient of friction from 0.046 to 0.058, and the cartilage values remained consistent [150]. In a reciprocating tribometer, an articular cartilage pin was articulated in sliding contact against PVA. As load increased from 10 N to 20 N a significant decrease in friction coefficient was seen. When Ringer's solution was used as the lubricant the coefficient was higher for all sliding velocities and loading conditions as compared to hyaluronic acid. Coefficients of friction were lower at sliding velocities of 0.1 m/s than 0.2 m/s. The authors demonstrated the effects of loading and speed on the frictional coefficient of PVA [151].

The addition of hydroxyapatite (HA) to polyvinyl alcohol has been evaluated due to the mechanical strength and toughness of pure polyvinyl alcohol. The mechanical properties of PVA-HA were evaluated in tension and compression and the coefficient of friction was found using ASTM D1984-01. Table 21 below summarizes the results found [152].

Table 21: Properties of PVA with varying amounts HA.

	0% HA	3% HA	7.5% HA
Compressive Modulus (MPa)	23.3 ± 4.6	148.6 ± 13.1	72.6 ± 7.9
Maximum Compressive Stress (MPa)	3.3 ± 0.8	> 29.2*	12.3 ± 3.1
Tensile Modulus (un-hydrated) (MPa)	703.2 ± 57.1	1073.6 ± 53.5	783.8 ± 9.1
Maximum Tensile Stress (un-hydrated) (MPa)	14.5 ± 1.6	21.7 ± 1.6	21.4 ± 2.3
Tensile Modulus (hydrated) (MPa)	152 ± 28	275 ± 23	205 ± 15
Maximum Tensile Stress (hydrated) (MPa)	285 ± 61	721 ± 25	410 ± 10
Coefficient of Friction	0.078 ± 0.011	0.067 ± 0.049	0.122 ± 0.047

*Load cell reached maximum before specimen failure

Using a similar sample preparation method, Gonzalez et al. produced PVA-HA samples with 1.5, 3, 6, and 7.5% wt HA. ASTM D412 was used for tensile testing protocol, ASTM D575-03 was used for compression testing and ASTM D1984-01 was used to obtain the coefficient of friction. Compressive modulus and maximum stress was highest for the 1.5% wt. HA at 166.1 ± 51 MPa and 16.9 ± 2.0 MPa respectively. The coefficient of friction for PVA with no HA was 0.073 ± 0.024 and 0.074 ± 0.009 for 3% wt HA, which was higher than the reported friction value above for 3% wt HA [153].

The addition of poly(vinyl pyrrolidone) (PVP) to PVA is another promising additive for PVA hydrogels. In a study using a pin-on-disk tester with a cobalt chrome pin and

either newborn bovine serum or bovine synovial fluid, authors evaluated hydrogels with 10% or 15% w/w solutions at loads of 100 N, 125 N, or 150 N over 100,000 loading cycles. The coefficients of friction were significantly lower after 25,000 for the synovial fluid lubrication. The coefficient of friction for both lubricants was initially 0.095 and fell steadily following 25,000 to 0.03 and 0.08 for synovial fluid and bovine serum respectively. Dry polymer loss (as a measure of wear) was higher in the 10% w/w polymers [154]. In a second study using sliding contact of a stainless steel ball, the tribologic properties of PVA-PVP hydrogel blends containing 15% wt. PVA and either 1% wt., 4% wt., 8% wt. and 15 % wt. PVP manufactured using either 2 – 8 hour freeze-thaw cycles, 4 – 8 hour freeze-thaw cycles or 6 – 8 hour freeze thaw cycles. The water content of the hydrogel increased with increased PVP and decreased with the number of freeze-thaw cycles. The coefficient of friction was lowest for 15% wt. PVP for all lubrication conditions (dry, distilled water, physiological saline, bovine serum). Tensile and compressive strengths increased with increased number of freezing and thaw cycles, and was highest at 1% wt. PVP [155]. PVA-PVP (99:1) hydrogels emulsified with poly(lactic-co-glycolic acid) (PLGA) and dichloromethane (DCM) or ethyl acetate (EA) were evaluated in unconfined compression, and indentation testing , and compared with PVA-PVP (99:1) (Table 22). The authors report that the methods of emulsification provide the ability to tailor the material properties of PVA [156].

Table 22: Aggregate modulus and permeability of emulsified PVA-PVP (a) with PLGA (b).

Sample	Aggregate Modulus (MPa)	Permeability ($\times 10^{-15} \text{ m}^4 / \text{N}\cdot\text{s}$)
Bovine Femoral Cartilage	0.332 ± 0.095	0.546 ± 0.325
PVA-PVP	0.111 ± 0.036	3.14 ± 1.97
DCM 10% wt. a, 10% wt. b	0.108 ± 0.020	3.26 ± 1.97
DCM 20% wt. a, 25 % wt. b	0.093 ± 0.188	2.80 ± 1.084
EA 10% wt. a, 10% wt. b	0.144 ± 0.45	1.91 ± 0.938
EA 20% wt. a, 10% wt. b	0.142 ± 0.267	0.950 ± 0.288
EA 20% wt. a, 25 % wt. b	0.094 ± 0.021	2.62 ± 0.566

The mixing of hydrophilic and hydrophobic polymers containing PVA, PVA and poly(ethylene-co-vinyl alcohol) (EVAP), or PVP and EVAP were evaluated in unconstrained compression, pin-on-disk testing, and contact angle calculation to evaluate their suitability for use as cartilage replacement materials. The authors reported coefficients of friction below 0.08 for all formulations with the lowest coefficient of friction for PVP-EVAP (15 % wt. / 55 % wt.). The lowest contact angle, and subsequently the most hydrophilic material was PVA. Bovine articular cartilage was more hydrophobic than any of the hydrogel formulations.

PVA-PVP hydrogels have been evaluated in an *in vivo* rabbit model. Following the freeze-thaw cycles, half of the specimen were placed directly into water to produce compliant specimen (elastic modulus = 0.59 ± 0.06 MPa), and half of the specimen were dehydrated at room temperature before being placed in water to produce the stiff sample (elastic modulus = 0.18 ± 0.02 MPa). Defects were made in the rabbit condylar surface in both the right and left knee, and were either left untreated, or treated with the compliant or stiff hydrogel specimen. At 24 weeks, soft tissue growth was seen over the compliant implant and bone growth was seen around the compliant implant. The stiff implant showed evidence of shrinkage and fibrous tissue growth was seen surrounding

the implant. Both the compliant implant and stiff implant had evidence of damage to the opposing cartilage [157].

The frictional properties of polyurethane have also been evaluated for use as artificial cartilage or cartilage replacement materials. Polyurethane specimens with varying elastic moduli (1.4 MPa, 6.5 MPa, and 22 MPa) were evaluated in a pendulum friction simulator against the medial compartment of bovine knees for 3600 cycles. Following testing, the surface roughness of the specimens was evaluated using surface profilometry with a resolution of 20 nm. The peak contact stress (5-6 MPa) was not significantly different for the negative control group (articular cartilage and meniscus) than the polyurethane samples with modulus of 1.4 MPa and 6.5 MPa. Significantly higher values, 16 MPa and 23 MPa were measured for polyurethane with a modulus of 22 MPa and the positive control group (stainless steel) respectively. The coefficient of friction was lowest for the duration of the test with articular cartilage and polyurethane with a modulus of 1.4 MPa. The volume of cartilage wear was calculated using microMRI, and found no discernable wear for the negative control or polyurethane samples with 1.4 MPa and 6.5 MPa modulus [158].

3.3. Materials and Method

The canine cadaver used in this study was euthanized for reasons unrelated to this study.

3.3.1. Bearing Construct Design

A computed tomography scan of a canine cadaveric forelimb was collected (Siemens Sensation 64, Siemens, Washington, D.C.; 140mA, 120 kVp, 0.6 mm slice thickness, 0.4 mm slice increment, 512 x 512 pixels). The radius and radial carpal bone were separated using greyscale thresholding (Mimics v21, Materialise, Plymouth MI) and exported to an .stl file. The bearing surfaces were designed using CAD software (3matic v12, Materialise, Plymouth, MI). Thickness of 1.5 mm, 2.5 mm, and 3.5 mm were selected for evaluation [154]. The articular surface was separated and offset either 1.5 mm, 2.5 mm, or 3.5 mm (Figure 26). The offset surface was then modified as described below for development of bearing surfaces of different materials. The carpal bone was isolated, and a hemisphere was centered on the distal side of the bone to create the surface matched compressive component.

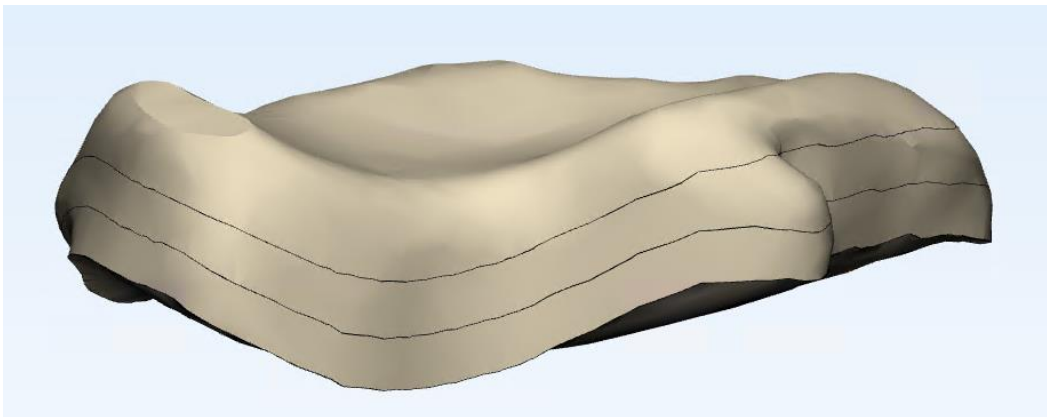


Figure 26: Bearing surface offsets – Top 1.5 mm offset, Top + Center 2.5 mm offset, Full – 3.5 mm offset.

3.3.1.1. Polyurethane

Polyurethane with a shore hardness of 60A and a young's modulus of 1.4-1.8 MPa was selected [158].

3.3.1.2. PVA-PVP

A solution of PVA (M_w : 146,000 - 186,00, 9002-89-5, Sigma Aldrich), and PVP (M_w : 40,000, PVP40, Sigma Aldrich) with a ratio of PVA to PVP of 96:4 was prepared as a 15% w/w solution in physiologic saline [155].

3.3.2. Test Specimen Manufacturing

3.3.2.1. Polyurethane

The polyurethane material was machined to obtain the desired shape. Because of the low hardness of the material, several trial components were manufactured. The first was machined at room temperature with coolant. The second was machined while submerged in 200 proof ethanol with dry ice, and the final trial component was manufactured while submerged in liquid nitrogen. Cryogenic machining of polymers with low hardness has been investigated previously as an alternative approach to molding [159].

Based on a visual inspection of the surface finish of the trial components, the final test specimens were machined while submerged in liquid nitrogen environment to with a press fit onto the metallic portion of the implant base testing analog (Figure 27).

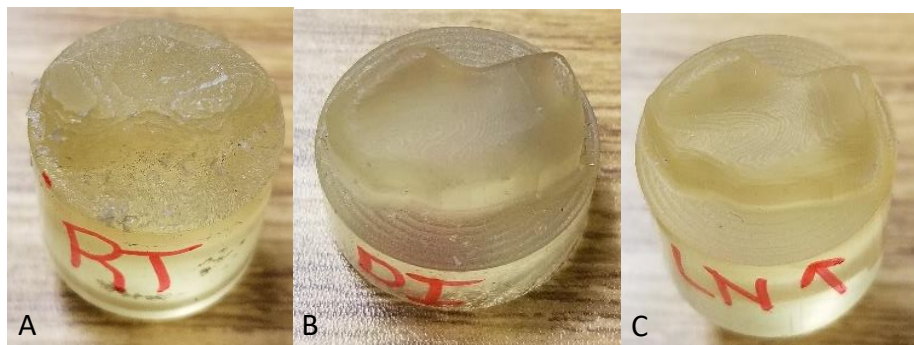


Figure 27: Polyurethane manufactured under different cooling environments. A) Room Temperature, B) Dry Ice in Ethanol, C) Liquid Nitrogen.

3.3.2.2. PVA – PVP

A porous surface on a solid titanium test fixture was manufactured using SLM (EOS Eosint M280, EOS GmbH, Munich, Germany) to create an artificial tidemark and create a structure for the polymer to adhere to (Figure 28).



Figure 28: As manufactured porous structures for attachment of molded PVA-PVP to bearing surface construct.

In a study by Mente and Lewis, a modulus for the tidemark was 0.32 ± 0.25 GPa [160]. Horn et al. evaluated the properties of a variety of titanium mesh structures for use in patient specific limb sparing implants. The optimal unit cell for a mesh structure for the tidemark according to Horn, would be a 20% relative density, rhombic dodecahedron with strut lengths of 6 mm; however, due to the size of the specimen, a smaller strut length was necessary and a strut length of 3 mm was selected [41]. Molds were designed based on the articular surface shape and manufactured using additive manufacturing (ObjetConnex, Stratasys, Eden Prairie, MN).

The PVA-PVP was prepared as described by Ma et al. Following dissolution of the polymers for 24 hours at 95°C. the material was cast into the molds, and the test

fixture was pressed into the mold such that the mesh structure was fully submersed. Specimen were then subjected to 5 cycles of freezing for 16 hours at -20°C and thawing a room temperature for 8 hours. [155] Hydrogel specimen were kept submerged in DI water up until test setup for the specific specimen.

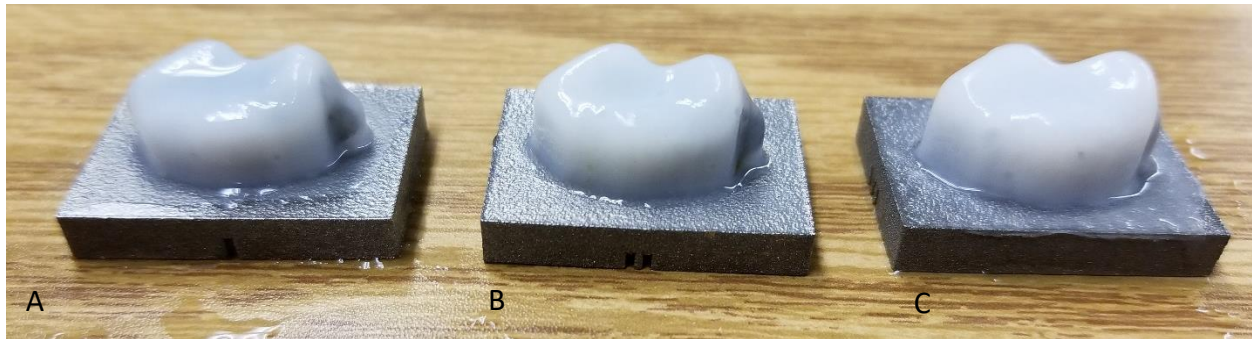


Figure 29: PVA-PVP Hydrogel Specimen following molding - A) 1.5mm, B) 2.5mm, C) 3.5mm thickness).

3.3.3. Test Method

A sample size of nine per material was selected based on material availability, and three samples were manufactured for each thickness level. The specimens were loaded onto a universal test machine (Series 1620-CC, Applied Test Systems Inc., Butler PA) and a calibrated 250-lb maximum load cell with $\pm 1\%$ accuracy was used for testing. Figure 30 shows a representative sample as loaded. Specimens were evaluated at two stain rates 100%/min and 1000%/min up to 65% strain as described by Shi et al. [161]. Specimens were first loaded to 65% strain at a rate of 100%/min 3 times to ensure proper seating of the surface matched carpal bone component. The 100%/min test (3 cycles) was repeated for evaluation followed immediately by the 1000%/min test (3 cycles). Specimens returned to a load of 0.2 lb following each cycle in order to maintain the position of the surface matched carpal bone component.

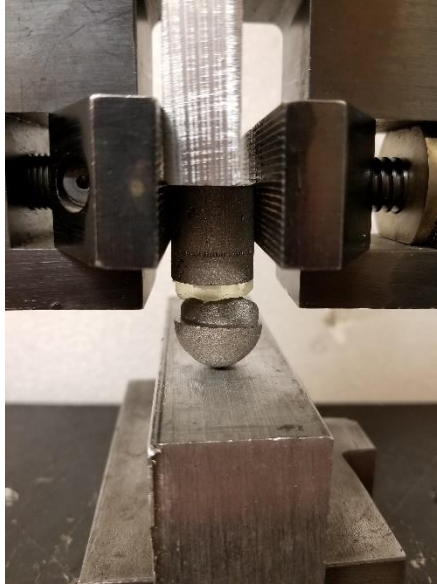


Figure 30: PU surface matched compression testing setup.

A random complete block design statistical model was developed for the experiment. The residual effects were assumed to have a normal distribution with mean 0 and equal variance with respect to treatment. P values < 0.05 were considered significant.

3.4. Results

A total of nine PVA-PVP specimens, and eight PU specimens were evaluated. One PU specimen was lost during the manufacturing process. No specimens showed visual evidence of damage following testing. The maximum load increased as the thickness increased and maximum loads at 1000%/min strain rates were higher than maximum load values at 100%/min strain rate increase (Table 23 - Table 26). Full results can be found in appendix E.

Table 23: Mean \pm SD of maximum load of PVA-PVP Samples – 100% Strain Rate (n=3).

Thickness	Maximum Load (lbs)
1.5 mm	2.52 \pm 1.68
2.5 mm	4.59 \pm 1.83
3.5 mm	5.36 \pm 1.30

mean values with different superscripts differ statistically ($P < 0.05$).

Table 24: Mean \pm SD of maximum load of PU Samples – 100% Strain Rate (n=3).

Thickness	Maximum Load (lbs)
1.5 mm	6.18 \pm 5.01
2.5 mm*	13.94 \pm 2.89
3.5 mm	18.92 \pm 4.71

mean values with different superscripts differ statistically ($P < 0.05$)

*Note: Only two specimens, one was lost during the manufacturing process

Table 25: Mean \pm SD of maximum load of PVA-PVP Samples – 1000% Strain Rate.

Thickness	Maximum Load (lbs)
1.5 mm	5.02 \pm 2.07
2.5 mm	5.51 \pm 2.23
3.5 mm	6.48 \pm 0.38

mean values with different superscripts differ statistically ($P < 0.05$).

Table 26: Mean \pm SD of maximum load of PU Samples – 1000% Strain Rate.

Thickness	Maximum Load (lbs)
1.5 mm	17.81 \pm 3.73
2.5 mm*	24.49 \pm 3.91
3.5 mm	25.78 ^B \pm 1.31

mean values with different superscripts differ statistically ($P < 0.05$).

*Note: Only two specimen, one was lost during the manufacturing process

Using a fitted full factorial model, the effects of material, thickness, and the interaction of material and thickness were found to be statistically significant on the maximum load reached at 65% strain. A second fit model was created for each material to understand the effects of strain rate and thickness on the behavior of materials individually. For both polyurethane and PVA-PVP, strain rate was not significant. A

Tukey's post hoc test was used to evaluate differences in thickness within each material (Table 27).

Table 27: Results of Tukey's post hoc test for maximum load as related to thickness.

Thickness	Polyurethane	PVA-PVP
1.5	A	A
2.5	B	A,B
3.5	C	B

Within a column, rows that do not contain the same letter are considered to have a statistically significant difference ($p < 0.05$)

The load vs time charts found below in Figure 31 and Figure 32 show that for both polyurethane and polyethylene as the thickness of the material increases the variability in the maximum load decreases. This phenomenon is pronounced at the 100% / minute strain rate.

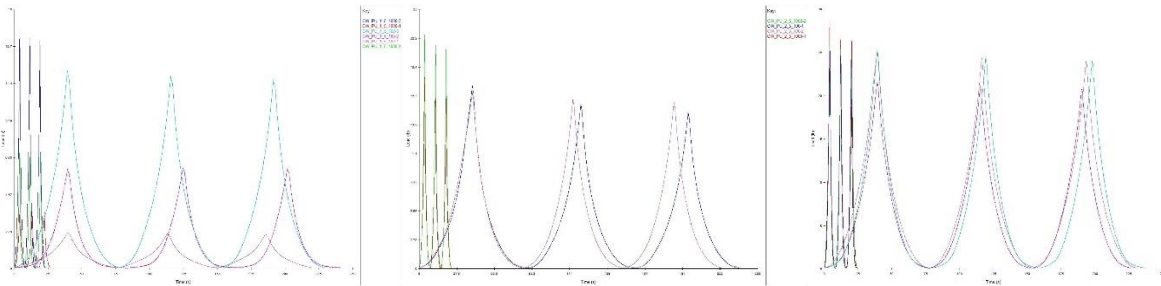


Figure 31: Load vs Time curves for Polyurethane Material, Left – 1.5 mm thickness, Center – 2.5 mm thickness, Right – 3.5 mm thickness

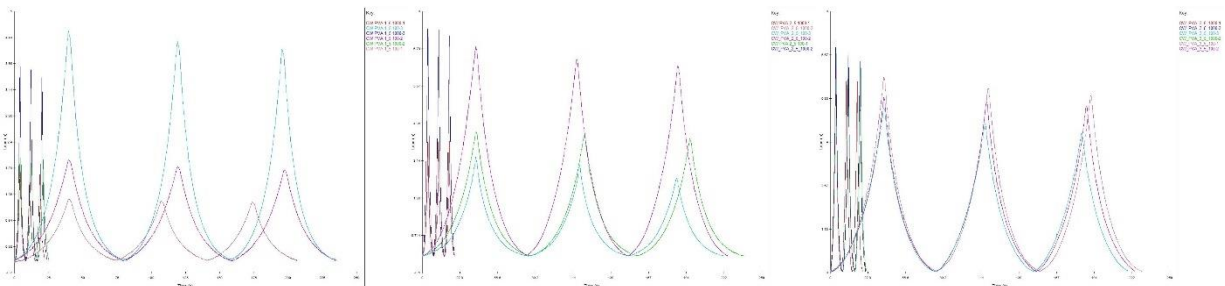


Figure 32: Load vs Time curves for PVA-PVP Hydrogel Material, Left 1.5 mm thickness, Center – 2.5 mm thickness, Right – 3.5 mm thickness

The representative load displacement curves illustrate an increasing stiffness as the displacement increases without regard to strain rate for both PVA-PVP materials (Figure 33) and PU materials.

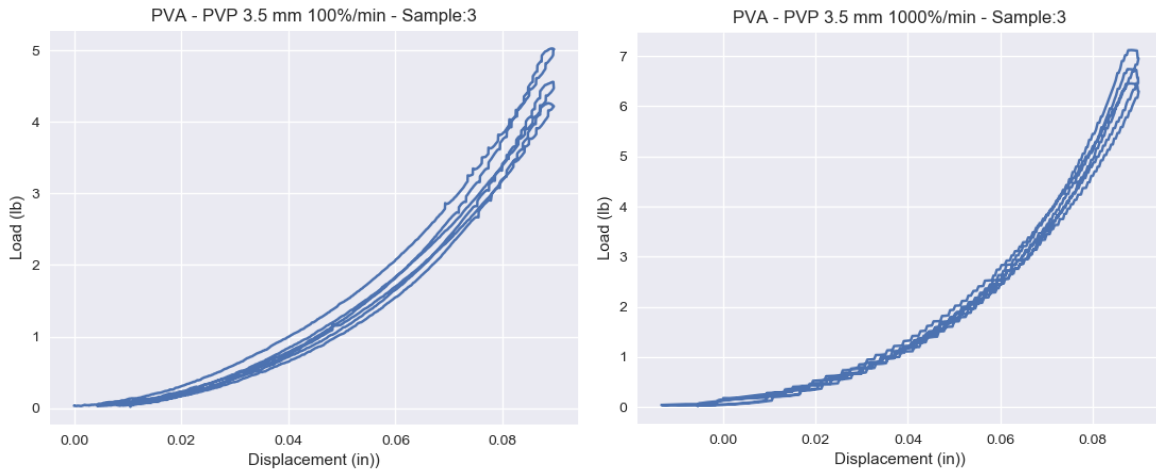


Figure 33: 3.5 mm thick PVA-PVP Sample – Load vs Displacement, Left: 100%/min strain rate, Right 1000%/min strain rate

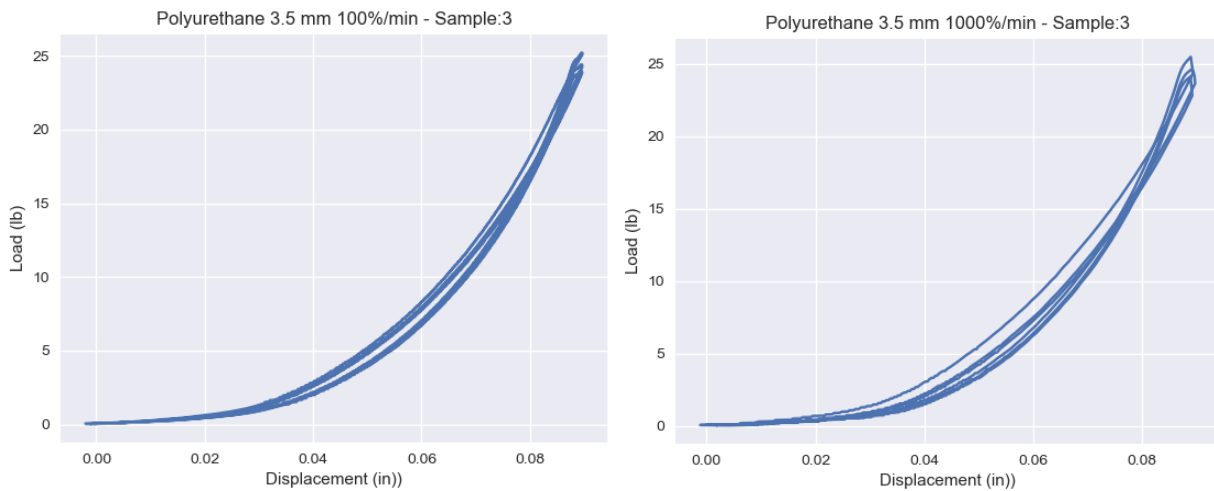


Figure 34: 3.5mm thick PU Sample – Load vs Displacement, Left: 100%/min strain rate, Right: 1000%/min strain rate

The compressive tangent stiffness was calculated from 10% strain to 60% strain for all of the specimen (Figure 35, Table 28). For both strain rates evaluated the stiffness of the material increased as the percent strain increased.

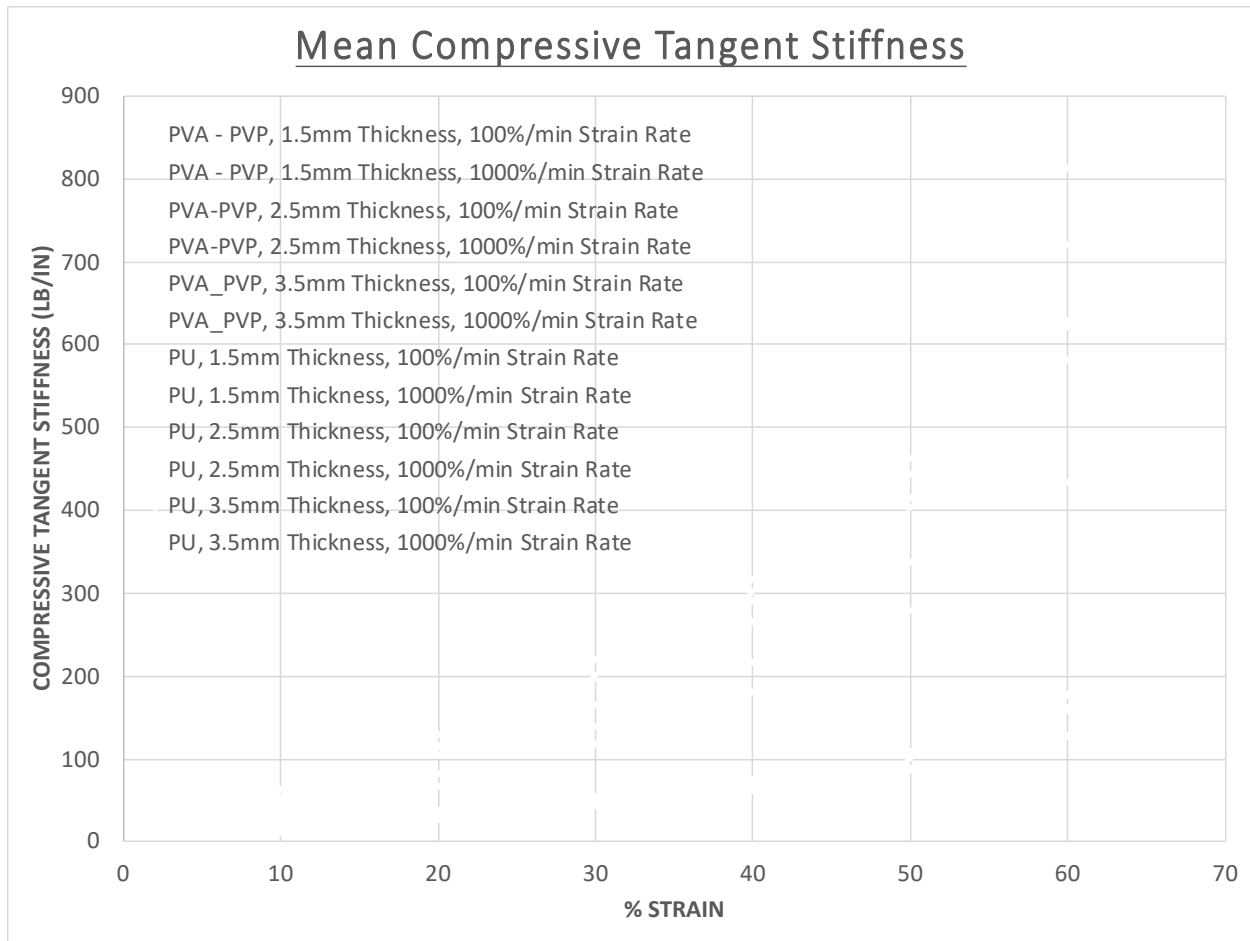


Figure 35: Mean compressive tangent stiffness by material, thickness and strain rate.

Table 28: Mean Compressive Tangent Stiffness (MPa, n=3).

Material	Thickness (mm)	Strain Rate (%/min)	10% Strain	20% Strain	30% Strain	40% Strain	50% Strain	60% Strain
PVA-PVP	1.5	100	16.50	26.25	42.20	64.65	101.80	158.08
PVA-PVP	1.5	1000	9.88	25.73	43.00	64.18	103.19	174.68
PVA-PVP	2.5	100	17.70	31.37	49.80	73.17	107.63	159.83
PVA-PVP	2.5	1000	15.80	33.87	49.93	75.54	110.77	190.20
PVA-PVP	3.5	100	16.63	30.68	44.05	61.34	86.44	125.95
PVA-PVP	3.5	1000	20.83	35.54	51.76	72.74	104.76	175.00
PU	1.5	100	30.08	65.69	116.38	178.15	277.03	433.33
PU	1.5	1000	35.41	80.82	137.49	215.12	336.05	580.26
PU	2.5*	100	51.61	111.98	164.50	263.20	401.79	619.96
PU	2.5*	1000	61.70	128.35	196.52	300.47	460.08	810.72
PU	3.5	100	43.05	103.94	199.39	288.55	414.18	626.69
PU	3.5	1000	50.28	113.89	218.90	315.02	442.24	717.50

*Note: Only two specimen, one was lost during the manufacturing process

3.5. Discussion

The aim of this research was to evaluate the ability to manufacture advanced polymers for bearing surface applications for a custom hemiarthroplasty of the distal region of the radius in a canine model. Two materials with favorable wear properties in pin-on-disc tests, were selected for use. PVA-PVP and PU polymers were evaluated for their manufacturability and compressive properties for use in direct load bearing applications with articular cartilage. As expected, the two bearing materials exhibited significantly different maximum loads at 65% strain. Both materials exhibited characteristics of viscoelastic materials, included strain rate dependent responses and increase in stiffness with an increase in strain rate [162].

PVA-PVP bearing constructs were designed to have biomimetic features. The hydrogel has a similar biphasic nature to cartilage, and the titanium mesh structure used at the base of the construct had properties similar to the tidemark in articular cartilage. The manufacturing process for this bearing construct had several additional steps and took a total of 7 days (168 hours) to achieve samples that were ready for use. The results from the limited sample size show similar load displacement profiles to those seen with PVA hydrogels in literature. This would indicate that manufacturing the PVA-PVP and utilizing a titanium mesh for attachment to a hemiarthroplasty implant does not significantly alter the compressive properties.

The PU bearing constructs used a more straightforward manufacturing process. Machining occurred in two setups and took approximately two hours which was substantially less than the 7 day manufacturing process for the hydrogel. A rod stock of material was machined in two orientations to create the press fit attachment features,

which doubled as features that were used to fix the component to the machine, and a second machining setup for machining the shape of the articular geometry. The machining was performed in liquid nitrogen to harden the material for enhanced machining performance. Further evaluation should be performed to validate the manufacturing processes, determine the relationship between the size of the patient and the optimal thickness of the polymer, and characterize the micromotion of the polyurethane against the titanium base plate.

3.6. Conclusions

The two bearing materials selected were able to be manufactured into functional geometries that were similar to the bearing surface geometry of the distal region of the canine radius. The manufacturing processes did not significantly alter the properties of the polymers as compared to other reported values in literature; however, further studies would need to be completed to determine the wear effects of the polymers on articular cartilage.

Chapter 4 – Proposed Implant Design Features

4.1. Introduction

The experiments performed in the previous sections contributed to a proposed set of hemiarthroplasty design features for a hemiarthroplasty in the canine radius. The results from the experiments in chapter 1 provided information as to the accuracy of patient data required. The results from the experiment presented in chapter 2 determined the clamping method suggested for use, and the results from the experiment presented in chapter 3 determined the material selected as the bearing material. The structure of the metallic stem portion of the implant was suggested to match the material properties of the bone as demonstrated in previous literature below.

4.2. Relevant Background

4.2.1. Metal Structure

Two additive manufacturing techniques are primarily utilized to manufacture metallic implants for orthopedic devices, SLM and EBM. SLM can achieve a higher resolution than EBM: 20 μm – 100 μm and 100 μm respectively. The EBM process takes place in a vacuum and at elevated temperatures. The higher temperatures result in lower levels of residual stresses, and completing manufacturing in a vacuum reduces the contaminants that can be added to the material due to the elements present in air [163].

Using additive manufacturing provides the opportunity to build structures that improve the gap between the mechanical properties of Ti-64 and bone as well as encourage bone ingrowth. Cortical bone porosities range from 1 μm to 100 μm in normal bone, the approximate modulus of bone is 15 GPa, and the density is 2.1 g/ml

[164]. Chua et al. reported required pore sizes of 200-400 μm for bone regeneration [165]. In an *in vivo* experiment, Taniguchi et al. evaluated the effect of pore size on bone ingrowth on specimen fabricated using SLM. Pore sizes of 300 μm , 600 μm , and 900 μm were evaluated using a 'diamond' lattice structure shown below in Figure 36. Rectangular specimens were implanted into the metaphysis of the tibia in rabbits for mechanical testing, and cylindrical specimen were implanted into the femoral condyle in rabbits for histological evaluation. Subjects were euthanized at 2, 4, or 8 weeks following implantation. Authors found mechanical strengths less than 1 GPa for all specimen; however, histologically at 8 weeks all specimen showed signs of bone mineralization in the tissue [166].

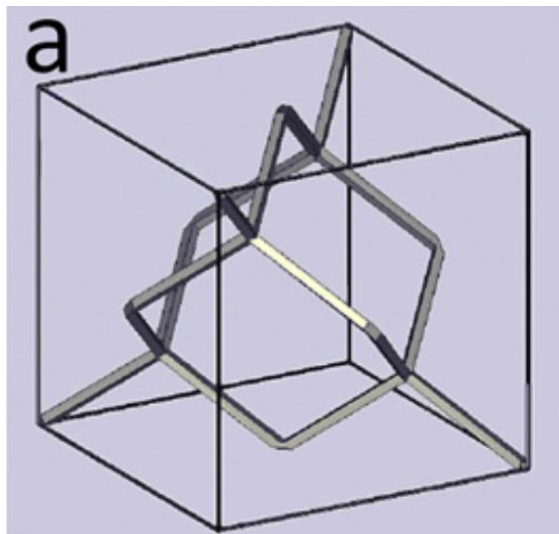


Figure 36: 'Diamond' lattice unit cell [165].

Stress shielding occurs when there is a large mismatch in properties between implantable materials and bone, resulting in the loading occurring through the implant causing the body to resorb the bone (Wolff's Law). The modulus of Ti-64 has been

reported to be 110 GPa, the modulus of cobalt chrome has been reported to be 220-234 GPa, and the modulus of stainless steel has been reported to be 200 MPa [164].

Selecting the unit cell, strut length and strut diameter are important for developing an implant that can reduce stress shielding and improve bone ingrowth into the implant. In an evaluation of unit cells structures suitable for additive manufacturing, authors reduced the number of unit cells to be considered for applications based on the repeatability of forming 3D structures by joining edges or vertices and eliminated structures that had large numbers of small faces. The resulting list is as follows: Platonic solids, cuboctetradron, truncated octahedron, truncated cube, rhombiccuboctehedron, truncated cuboctahedron, triangular prism, rectangular prism, hexagonal prism, octagonal prism, and rhombic dodecahedron [165]. Twelve faced rhombic dodecahedron unit cells were selected by Harrysson et al., and the length of the rectangular struts was varied for evaluation of a femoral stem. Mechanical testing was performed in the build direction and perpendicular to the build direction. The modulus of the material from compression testing was 60 MPa, 25 MPa, and 12 MPa for 8 mm, 10 mm, and 12 mm strut lengths respectively perpendicular to the build platform, and 78.81 MPa and 23.63 MPa for 8 mm and 10 mm respectively in the build direction. In bending tests, the Young's modulus of the 3mm was closest to that of bone with an average of 12.01 GPa [167].

Heinl et al. evaluated two porous structures: the 'diamond structure' is based on a diamond lattice tetrahedrally surrounded by other lattice structures, and the 'hatch structure' where parallel lines with a spacing of 1 mm were alternated every 90° natively on the EBM machine. For the diamond structure the elastic modulus and maximum

strength of specimen tested in compression was 1.6 ± 0.3 GPa and 29.3 ± 0.8 MPa in the build direction and 0.9 ± 0.1 GPa, 21.0 ± 0.7 MPa perpendicular to the build direction respectively. The reported porosity was $81.1 \pm 0.04\%$ (build direction) and $80.8 \pm 0.3\%$ (perpendicular). The hatched structure had modulus and maximum strength of 12.9 ± 0.9 GPa and 148.4 ± 3.5 MPa in the build direction, and 3.9 ± 2.1 GPa, 127.1 ± 29.2 MPa perpendicular to the build direction respectively. Porosity was identical in the build direction and perpendicular to the build direction: $59.5 \pm 0.6\%$. Authors reported that for human femoral cortical bone the modulus and maximum strength were 18.2 ± 0.85 GPa and 205 ± 12.6 MPa parallel to the long axis of the bone and 11.7 ± 1.01 GPa and 131 ± 20.7 MPa perpendicular to the long axis of the bone respectively [168].

Biologically relevant results were obtained from ‘twisted’ unit cell designs manufactured in varying orientations using SLM [169]. The elastic modulus and compressive strength of designs were A) 21.4 ± 0.9 GPa and 316.9 ± 2.6 MPa, B) 14.8 GPa and 228.7 ± 1.0 MPa, C) 26.3 ± 2.1 GPa and 402.9 ± 8.8 MPa respectively (Figure 37). A and B had a larger unit cell height, width, depth, and strut diameter than C. Authors found that the porosity of the built specimen had a difference of less than 2.5% from the porosity as calculated using the CAD model.

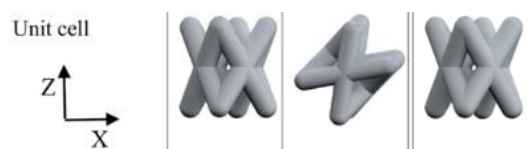


Figure 37: Successful Unit Cell Orientations (Left A, Center B, Right C) [169].

Mullen et al. evaluated the porosity, compressive, and fatigue properties of octahedron unit cell designs that include randomized structures for porous orthopedic implants manufactured using SLM (Figure 38) [169]. Randomization resulted in an increased average pore size, larger pore size range, and Young's moduli between 2 and 4 GPa depending on the degree of randomization between no randomization and 30% randomization. Authors found significant improvement in fatigue properties of all specimen with the addition of a heat treatment of the specimen following manufacturing [170].

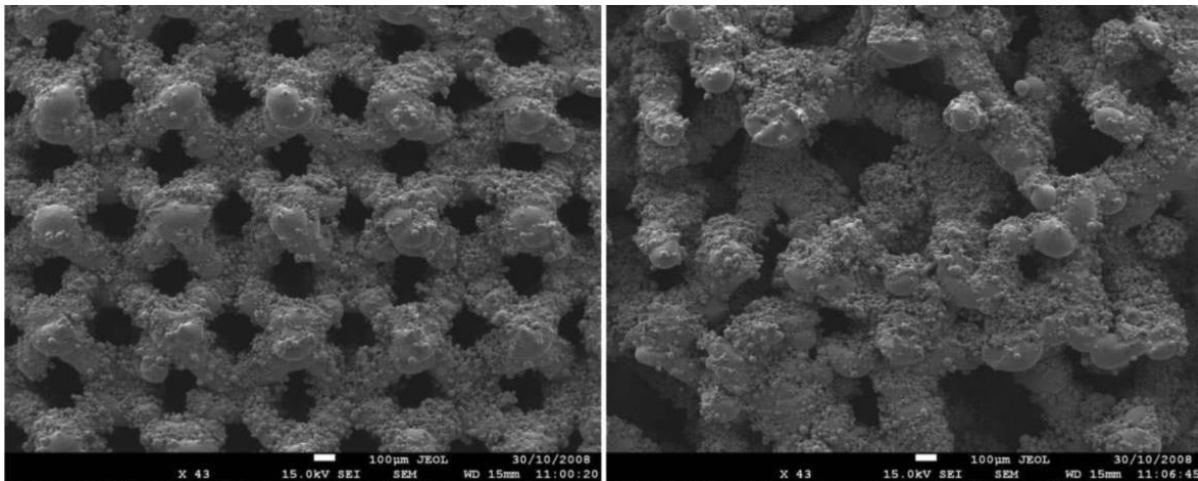


Figure 38: Scaffolds with no randomization (left) and 30% randomization (right).

A porous AM stem for total hip arthroplasty manufactured using SLM was evaluated by Arabnejad et al. [170]. Patient data from a CT-scan was used to determine the density of bone across the surface, which was converted to elastic modulus. The porous portion of the implant was generated from gauss quadrature integration with requirements including pore size ($500\ \mu\text{m}$), strut diameter, and porosity (70%). Six artificial femurs received either the porous or solid implant with identical outer geometry.

The authors reported significantly reduced strain with the porous implant; however, no mechanical testing of the properties of the mesh structure was directly performed [171].

Horn describes the use of a mesh geometry for limb sparing in the canine radius. A parametric rhombic dodecahedron mesh with circular strut cross sections was designed with strut sizes of 3 mm, 6 mm, and 9 mm and relative densities of 0.2, 0.3, and 0.4. Parts were manufactured in a single EBM build. Unit cells with 0.4 relative densities has elastic moduli most similar to the 15 GPa approximate value for cortical bone: 10.72 ± 0.33 Gpa (3 mm strut size), 12.54 ± 0.38 Gpa (6 mm strut size), and 14.05 ± 0.40 Gpa (9 mm strut size) [41].

4.3. Proposed Design Features and Process

Based on the results of the previous studies and the literature, the proposed design for a canine hemiarthroplasty implant would include the features found below in Table 29

Table 29: Design elements of hemiarthroplasty in the canine radius from literature and experiments performed in the body of work above.

Description	Specification
Bearing Material	Polyurethane, Shore Hardness 60A, Modulus 1.4 – 1.6MPa
Bearing Material Thickness	3.5 mm
Primary Ligament Clamp Texture	Spiked
Secondary Ligament Clamp Texture	Random Porous Structure [109]
Clamping Screw	M3 or Larger
Bulk Implant Design	0.4 Relative Density, Rhombic dodecahedron unit cell lattice structure with 9 mm Strut Size [41]
Soft Tissue Preserving Shell	1mm thick x 12 mm long alternating down the length of the bone [41]
Attachment to remaining bone	Conformal attachment plates on the dorsal side of the remaining radius [41]

The development process of a custom patient specific implant requires a team of individuals including both engineers and surgeons. A proposed development process is shown below in Figure 39. First, patient specific data must be obtained and based on the research presented in Chapter 1 above the minimum resolution for a feline model is 0.192 mm for both slice thickness and pixel dimensions. For a canine model, this number may likely be slightly higher; however, more accurate models are always better if they do not substantially increase the radiation dose or time of the scan.

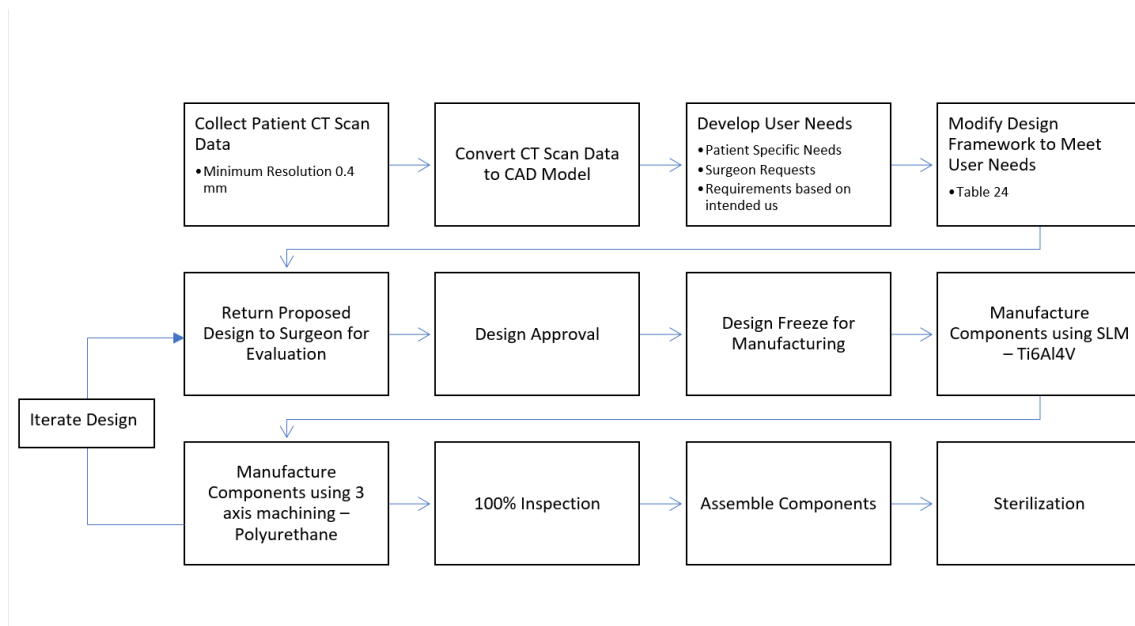


Figure 39: Suggested process model for custom patient specific hemiarthroplasty in a canine model.

Once the patient data is collected, the image files are converted into a CAD model. This step is important as selecting the best greyscale threshold values and manipulating the data to obtain the cad models can alter the data with little to no safeguards available until a surgeon is in the operating room with an implant that does not fit as expected. The resulting CAD models are then manipulated to design the implant features based on the results from the studies in Chapter 2 and 3 as well as

literature, a proposed set of features is described in Table 29. The manufacturing process should include GMP practices and components should be inspected fully. The design features and process framework provide an evidence based starting point for design process and manufacturing process validation for custom patient specific hemiarthroplasty in a canine model.

CONCLUSIONS

The current designs of hemiarthroplasty have limited its use clinically in both human and veterinary medicine. The work presented in this dissertation provides the basic scientific framework for the development of custom patient specific hemiarthroplasty.

Evaluating the accuracy of current CT scanning technology was critical to understanding the limitations of CAD models created by converting 2-dimensional image data obtained from CT scanning into patient specific CAD models to use for custom patient specific implant design. Using a feline model in the radial carpal joint provided similar size scale to human fingers, toes, and temporomandibular joints; however, the size limited the ability to obtain clinical CT scans that were accurate enough for use in custom patient specific hemiarthroplasty in the feline radius. Artificially reducing the resolution of μ CT scans using python scripting in combination with the common techniques for creating CAD models from CT scans allowed for a “big data” style approach to determining an appropriate resolution for small joints that may be clinically feasible in the future. A resolution of 0.192 mm was deemed to be appropriate; however, current clinical CT scanners can commonly achieve a lowest resolution of between 0.4 mm and 0.6 mm, and current *in-vivo* μ CT scanners have limited bore diameter. Evaluating the accuracy of a larger joint, potentially the canine radius, would have provided more globally applicable results from the experiments performed in Chapter 1.

Designs for attaching the feline MCL using additive manufacturing were evaluated in Chapter 2. The size of the feline radius again posed challenges due to the

size of the implant. Initial testing analogs were too large to be used, requiring a design change to using the shape of the CT scanned bone to use as the base for the clamps. Due to the size of the feline radius, screws for clamping were selected to be M2; however, the bolts would shear off when torque greater than 4 in-lbs was applied. That required yet another design change that included increasing the size of the implant model to accommodate M3 screws. Due to the delicate nature of the ligaments, several samples were lost due to tearing during loading. This also limited the findings as ligaments may have been exposed to high loads unintentionally during test setup, despite best efforts to avoid placing load on the ligament prior to testing. The results obtained from this study were promising. Additive manufacturing can be used as successfully as traditional manufacturing methods used to create tendon attachment methods. The spiked texture performed the best with respect to maximum load; however, the ridged design performed best with respect to stiffness. The selection of a manufacturing process with very few limitations will allow for the optimization of the clamp design to further improve performance.

A switch to a canine model was used for the experiments performed in Chapter 3 to more easily manufacture the bearing surfaces. Evaluating the potential bearing materials in a surface matched compressive test provided a link between the data that was published on both polyurethane and PVA-PVP hydrogels and the transition to their use as a bearing material in hemiarthroplasty. First, the experiments showed that both of the materials could be manufactured in a variety of thicknesses. The materials exhibited load vs displacement curves that were consistent with viscoelastic materials, and the maximum load at 65% strain was higher for all of the polyurethane specimen

regardless of strain rate or thickness. A polyurethane bearing surface of 3.5 mm thick should be selected as the baseline for further investigation for use in canine distal radial hemiarthroplasty.

The work culminated in a proposed design process and initial design framework for future validation and verification of the development of custom patient specific hemiarthroplasty in a veterinary model. This framework is limited to the veterinary scope as the size of the features evaluated limit the global utilization of the framework. Further work should be done to evaluate the components of the framework developed in the scope of this dissertation.

REFERENCES

1. Wiggins, L., *Tritanium pl cage 510(k) substantially equivalent*, F.a.D. Administration, Editor. 2016:
https://www.accessdata.fda.gov/cdrh_docs/pdf16/K162262.pdf.
2. *K133809* U.S.F.a.D. Administration, Editor.:
<https://www.accessdata.fda.gov/scripts/cdrh/cfdocs/cfpmn/pmn.cfm?ID=K133809>
3. *K121818*, U.S.F.a.D. Administration, Editor.:
<https://www.accessdata.fda.gov/scripts/cdrh/cfdocs/cfpmn/pmn.cfm?ID=K121818>
4. *K122870*, U.S.F.a.D. Administration, Editor.:
<https://www.accessdata.fda.gov/scripts/cdrh/cfdocs/cfpmn/pmn.cfm?ID=K122870>
5. Marcellin-Little, D.J., et al., *In vitro evaluation of a low-modulus mesh canine prosthetic hip stem*. American Journal of Veterinary Research, 2010. **71**(9): p. 1089-1095.
6. van den Bekerom, M.P.J., et al., *Total shoulder arthroplasty versus hemiarthroplasty for glenohumeral arthritis: A systematic review of the literature at long-term follow-up*. International Journal of Shoulder Surgery, 2013. **7**(3): p. 110-115.
7. Burgers, P.T.P.W., et al., *Total hip arthroplasty versus hemiarthroplasty for displaced femoral neck fractures in the healthy elderly: A meta-analysis and systematic review of randomized trials*. International Orthopaedics, 2012. **36**(8): p. 1549-1560.
8. Luetke, A., et al., *Osteosarcoma treatment - where do we stand? A state of the art review*. Cancer Treatment Reviews, 2014. **40**(4): p. 523-532.
9. Mirabello, L., R.J. Troisi, and S.A. Savage, *Osteosarcoma incidence and survival rates from 1973 to 2004: Data from the surveillance, epidemiology, and end results program*. Cancer, 2009. **115**(7): p. 1531-1543.
10. Anfinson, K.P., et al., *Age-period-cohort analysis of primary bone cancer incidence rates in the united states (1976-2005)*. Cancer Epidemiology Biomarkers & Prevention, 2011. **20**(8): p. 1770-1777.
11. Mirabello, L., R.J. Troisi, and S.A. Savage, *International osteosarcoma incidence patterns in children and adolescents, middle ages and elderly persons*. International Journal of Cancer, 2009. **125**(1): p. 229-234.
12. Mueller, F., B. Fuchs, and B. Kaser-Hotz, *Comparative biology of human and canine osteosarcoma*. Anticancer Research, 2007. **27**(1A): p. 155-164.
13. Brodey, R.S. and W.H. Riser, *Canine osteosarcoma - a clinicopathologic study of 194 cases*. Clinical Orthopaedics and Related Research, 1969(62): p. 54-&.
14. Brodey, R.S., *Use of naturally occurring cancer in domestic-animals for research into human cancer - general-considerations and a review of canine skeletal osteosarcoma*. Yale Journal of Biology and Medicine, 1979. **52**(4): p. 345-361.
15. Szewczyk, M., R. Lechowski, and K. Zabielska, *What do we know about canine osteosarcoma treatment? - review*. Veterinary Research Communications, 2015. **39**(1): p. 61-67.
16. Heldmann, E., M.A. Anderson, and C. Wagner-Mann, *Feline osteosarcoma: 145 cases (1990-1995)*. Journal of the American Animal Hospital Association, 2000. **36**(6): p. 518-521.

17. Kessler, M., et al., *Feline osteosarcoma: Epidemiologic, clinical, and radiologic findings in 78 cases (1990-1995)*. Tierarztliche Praxis, 1997. **25**(3): p. 275-283.
18. Liu, S.K., H.D. Dorfman, and A.K. Patnaik, *Primary and secondary bone tumours in the cat*. The Journal of small animal practice, 1974. **15**(3): p. 141-156.
19. Tas, O., et al., *Synovial osteochondromatosis and sclerosing osteosarcoma in a cat*. Veterinary and Comparative Orthopaedics and Traumatology, 2013. **26**(2): p. 160-164.
20. Sonnenschein, B., M.J. Dickomeit, and M.S. Bali, *Late-onset fracture-associated osteosarcoma in a cat*. Veterinary and Comparative Orthopaedics and Traumatology, 2012. **25**(5): p. 418-420.
21. Rowell, J.L., D.O. McCarthy, and C.E. Alvarez, *Dog models of naturally occurring cancer*. Trends in Molecular Medicine, 2011. **17**(7): p. 380-388.
22. Avila, H.M., et al., *Novel bilayer bacterial nanocellulose scaffold supports neocartilage formation in vitro and in vivo*. Biomaterials, 2015. **44**: p. 122-133.
23. Grimer, R.J., *Surgical options for children with osteosarcoma*. Lancet Oncology, 2005. **6**(2): p. 85-92.
24. Longhi, A., et al., *Primary bone osteosarcoma in the pediatric age: State of the art*. Cancer Treatment Reviews, 2006. **32**(6): p. 423-436.
25. Straw, R.C. and S.J. Withrow, *Limb-sparing surgery versus amputation for dogs with bone tumors*. The Veterinary clinics of North America. Small animal practice, 1996. **26**(1): p. 135-143.
26. Ta, H., et al., *Osteosarcoma treatment: State of the art*. Cancer and Metastasis Reviews, 2009. **28**(1-2): p. 247-263.
27. Morello, E., M. Martano, and P. Buracco, *Biology, diagnosis and treatment of canine appendicular osteosarcoma: Similarities and differences with human osteosarcoma*. The Veterinary Journal, 2011. **189**(3): p. 268-277.
28. Liu, T., et al., *Total femoral reconstruction with custom prosthesis for osteosarcoma*. World journal of surgical oncology, 2016. **14**(1): p. 93.
29. Mangat, K.S., L.M. Jeys, and S.R. Carter, *Latest developments in limb-salvage surgery in osteosarcoma*. Expert Review of Anticancer Therapy, 2011. **11**(2): p. 205-215.
30. Galasso, O., et al., *Disassembly of a distal femur modular prosthesis after tumor resection*. The Journal of Arthroplasty, 2010. **25**(2): p. 334.e5-334.e9.
31. Orlic, D., et al., *Lower limb salvage surgery: Modular endoprosthesis in bone tumour treatment*. International Orthopaedics, 2006. **30**(6): p. 458-464.
32. Peterson, J.R., et al., *Limb sparing resection for tumors involving the distal humerus and reconstruction with a modular endoprosthesis*. Bulletin of the NYU Hospital for Joint Diseases, 2015. **73**(3): p. 190.
33. Rosenbaum, D., et al., *Physical activity levels after limb salvage surgery are not related to clinical scores—objective activity assessment in 22 patients after malignant bone tumor treatment with modular prostheses*. Journal of Surgical Oncology, 2008. **98**(2): p. 97-100.
34. Ness, K.K., et al., *A comparison of function after limb salvage with non-invasive expandable or modular prostheses in children*. European journal of cancer (Oxford, England : 1990), 2014. **50**(18): p. 3212-3220.

35. Neel, M.D., et al., *Early multicenter experience with a noninvasive expandable prosthesis*. *Clinical Orthopaedics and Related Research*, 2003. **415**(415): p. 72-81.
36. Mitchell, K.E., et al., *Outcomes of limb-sparing surgery using two generations of metal endoprosthesis in 45 dogs with distal radial osteosarcoma. A veterinary society of surgical oncology retrospective study*. *Veterinary Surgery*, 2016. **45**(1): p. 36-43.
37. Venzin, C., S. Grundmann, and P. Montavon, *Endoprosthesis (en) in frontlimb-sparing surgery for distal radial tumours in the dog: Preliminary results*. *Schweizer Archiv für Tierheilkunde*, 2012. **154**(8): p. 337.
38. Venzin, C., S. Grundmann, and P.M. Montavon, *Loss of implant-bone interface following distal radial locking-plate endoprosthesis limb-sparing surgery in a dog*. *Journal of Small Animal Practice*, 2012. **53**(1): p. 57-62.
39. MacDonald, T.L. and T.D. Schiller, *Limb-sparing surgery using tantalum metal endoprosthesis in a dog with osteosarcoma of the distal radius*. *The Canadian veterinary journal. La revue vétérinaire canadienne*, 2010. **51**(5): p. 497-500.
40. Harrysson, O.L.A., D.J. Marcellin-Little, and T.J. Horn, *Applications of metal additive manufacturing in veterinary orthopedic surgery*. *JOM*, 2015. **67**(3): p. 647-654.
41. Horn, T.J., *Development and experimental evaluation of a novel, patient specific implant for limb sparing surgery*, in *Industrial and Systems Engineering*. North Carolina State University.
42. Liptak, J.M., et al., *Limb-sparing surgery in a dog with osteosarcoma of the proximal femur*. *Veterinary Surgery*, 2005. **34**(1): p. 71-77.
43. Chung, S.H., et al., *Temporary hemiarthroplasty with a synthetic device in children with osteosarcoma around the knee as a bridging procedure until skeletal maturity*. *Journal of Surgical Oncology*, 2015. **112**(1): p. 107-114.
44. Manoso, M.W., et al., *Acetabular development after bipolar hemiarthroplasty for osteosarcoma in children*. *Journal of Bone and Joint Surgery-British Volume*, 2005. **87B**(12): p. 1658-1662.
45. Mayilvahanan, N., et al., *Custom mega-prosthetic replacement for proximal humeral tumours*. *International Orthopaedics*, 2006. **30**(3): p. 158-162.
46. van Egmond, P.W., A.H.M. Taminiau, and H.J.L. van der Heide, *Hemiarthroplasties in young patients with osteonecrosis or a tumour of the proximal femur; an observational cohort study*. *BMC musculoskeletal disorders*, 2013. **14**(1): p. 31-31.
47. Price, S.L., et al., *Complications of cemented long-stem hip arthroplasty in metastatic bone disease revisited*. *Clinical Orthopaedics and Related Research*, 2013. **471**(10): p. 3303-3307.
48. Schneiderbauer, M.M., et al., *Dislocation rate after hip hemiarthroplasty in patients with tumor-related conditions*. *Journal of Bone and Joint Surgery*, 2005. **87**(8): p. 1810-1815.
49. Ahn, J., et al., *Systematic review of cemented and uncemented hemiarthroplasty outcomes for femoral neck fractures*. *Clinical Orthopaedics and Related Research*, 2008. **466**(10): p. 2513-2518.

50. Luo, X., et al., *Systematic review of cemented versus uncemented hemiarthroplasty for displaced femoral neck fractures in older patients*. Archives of orthopaedic and trauma surgery, 2012. **132**(4): p. 455-463.
51. Dos Santos, A.L.G., et al., *Hállux rígido: Prospective study of joint replacement with hemiarthroplasty*. Acta ortopedica brasileira, 2013. **21**(2): p. 71.
52. Ronconi, P., et al., *Hemiarthroplasty and distal oblique first metatarsal osteotomy for hallux rigidus*. Foot & ankle international, 2011. **32**(2): p. 148-152.
53. Sorbie, C. and G.A.B. Saunders, *Hemiarthroplasty in the treatment of hallux rigidus*. Foot & ankle international, 2008. **29**(3): p. 273-281.
54. Konkel, K.F., A.G. Menger, and S.A. Retzlaff, *Results of metallic hemi-great toe implant for grade iii and early grade iv hallux rigidus*. Foot & ankle international, 2009. **30**(7): p. 653-660.
55. Kissel, C.G., et al., *A prospective investigation of the biopro ® hemi-arthroplasty for the first metatarsophalangeal joint*. The Journal of Foot and Ankle Surgery, 2008. **47**(6): p. 505-509.
56. Raikin, S.M. and J. Ahmad, *Comparison of arthrodesis and metallic hemiarthroplasty of the hallux metatarsophalangeal joint. Surgical technique*. Journal of Bone and Joint Surgery, 2008. **90**(Supplement 2, Part 2): p. 171-180.
57. Sparrow, T., et al., *Shoulder joint hemiarthroplasty for treatment of a severe osteochondritis dissecans lesion in a dog*. Veterinary and Comparative Orthopaedics and Traumatology, 2014. **27**(3): p. 243-248.
58. Giannatsis, J. and V. Dedoussis, *Additive fabrication technologies applied to medicine and health care: A review*. International Journal of Advanced Manufacturing Technology, 2009. **40**(1-2): p. 116-127.
59. Sidambe, A.T., *Biocompatibility of advanced manufactured titanium implants-a review*. Materials, 2014. **7**(12): p. 8168-8188.
60. Haslauer, C.M., et al., *In vitro biocompatibility of titanium alloy discs made using direct metal fabrication*. Med Eng Phys, 2010. **32**(6): p. 645-52.
61. Anon, *Medical electronics instrumentation: Fda approval for ebm implants*. 2011, Centaur Communications Ltd: London. p. 35-35.
62. Murr, L.E., et al., *Next generation orthopaedic implants by additive manufacturing using electron beam melting*. International journal of biomaterials, 2012. **2012**: p. 245727.
63. Wang, X., et al., *Topological design and additive manufacturing of porous metals for bone scaffolds and orthopaedic implants: A review*. Biomaterials, 2016. **83**: p. 127-141.
64. *The world's first 3d printed total jaw reconstruction*. 2011; Available from: <http://www.xilloc.com/patients/stories/total-mandibular-implant/>.
65. Chen, X., B.K. Zimmerman, and X.L. Lu, *Determine the equilibrium mechanical properties of articular cartilage from the short-term indentation response*. J Biomech, 2015. **48**(1): p. 176-180.
66. Varga, P., et al., *Finite element based estimation of contact areas and pressures of the human scaphoid in various functional positions of the hand*. J Biomech, 2013. **46**(5): p. 984-90.
67. Marquez-Florez, K., et al., *Theoretical distribution of load in the radius and ulna carpal joint*. Comput Biol Med, 2015. **60**: p. 100-6.

68. Majors, B.J. and J.S. Wayne, *Development and validation of a computational model for investigation of wrist biomechanics*. Ann Biomed Eng, 2011. **39**(11): p. 2807-15.
69. Katz, M.A., et al., *Computed tomography scanning of intra-articular distal radius fractures: Does it influence treatment?* J Hand Surg Am, 2001. **26**(3): p. 415-21.
70. Leventhal, E.L., et al., *Interfragmentary motion in patients with scaphoid nonunion*. J Hand Surg Am, 2008. **33**(7): p. 1108-15.
71. Marquez-Florez, K., et al., *Load distribution on the radio-carpal joint for carpal arthrodesis*. Comput Methods Programs Biomed, 2016. **127**: p. 204-15.
72. Lalone, E.A., et al., *Accuracy assessment of 3d bone reconstructions using ct: An intro comparison*. Med Eng Phys, 2015. **37**(8): p. 729-38.
73. Zhang, Z.L., et al., *Detection accuracy of condylar bony defects in promax 3d cone beam ct images scanned with different protocols*. Dentomaxillofac Radiol, 2013. **42**(5): p. 20120241.
74. Bois, A.J., et al., *Quantifying glenoid bone loss in anterior shoulder instability: Reliability and accuracy of 2-dimensional and 3-dimensional computed tomography measurement techniques*. Am J Sports Med, 2012. **40**(11): p. 2569-77.
75. Fitzwater, K.L., et al., *Evaluation of the effect of computed tomography scan protocols and freeform fabrication methods on bone biomodel accuracy*. Am J Vet Res, 2011. **72**(9): p. 1178-1185.
76. Pinto, J.M., et al., *Sensitivity analysis of geometric errors in additive manufacturing medical models*. Med Eng Phys, 2015. **37**(3): p. 328-334.
77. Rahmati, S., F. Abbaszadeh, and F. Farahmand, *An improved methodology for design of custom-made hip prostheses to be fabricated using additive manufacturing technologies*. Rapid Prototyp J, 2012. **18**(5): p. 389-400.
78. Harris, W.H., et al. *Pressure distribution in the hip and selection of hemiarthroplasty*. in *Proceedings of the Third Open Scientific Meeting of the Hip Society*. 1975. St. Louis: CV Mosby.
79. DeVries, N.A., et al., *Validation of phalanx bone three-dimensional surface segmentation from computed tomography images using laser scanning*. Skeletal Radiol, 2008. **37**(1): p. 35-42.
80. Breit, S., K. Pfeiffer, and R. Pichler, *Use of a 3d laser scan technique to compare the surface geometry of the medial coronoid process in dogs affected with medial compartment disease with unaffected controls*. Veterinary Journal, 2010. **185**(3): p. 285-291.
81. Soslowsky, L.J., et al., *Articular geometry of the glenohumeral joint*. Clin Orthop Rel Res, 1992. **285**: p. 181-190.
82. Soslowsky, L.J., et al., *Articular geometry of the glenohumeral joint*. Clinical Orthopaedics and Related Research, 1992(285): p. 181-190.
83. Desai, S.J., et al., *An anthropometric study of the distal humerus*. Journal of Shoulder and Elbow Surgery, 2014. **23**(4): p. 463-469.
84. Wilson, L.A.B. and L.T. Humphrey, *A virtual geometric morphometric approach to the quantification of long bone bilateral asymmetry and cross-sectional shape*. Am J Phys Anthropol, 2015. **158**(4): p. 541-556.

85. Trinh, N.H., et al., *Accurate measurement of cartilage morphology using a 3d laser scanner*, in *Computer vision approaches to medical image analysis*, R.R. Beichel, Editor. 2006. p. 37-48.
86. Aubin, C.É., et al., *Morphometric evaluations of personalised 3d reconstructions and geometric models of the human spine*. *Med Biol Eng Comput*, 1997. **35**(6): p. 611-618.
87. Koo, S., et al., *Accuracy of 3d cartilage models generated from mr images is dependent on cartilage thickness: Laser scanner based validation of in vivo cartilage*. *Journal of Biomechanical Engineering-Transactions of the Asme*, 2009. **131**(12).
88. Millington, S.A., et al., *Quantification of ankle articular cartilage topography and thickness using a high resolution stereophotography system*. *Osteoarthritis and Cartilage*, 2007. **15**(2): p. 205-211.
89. Zumstein, V., et al., *The glenohumeral joint - a mismatching system? A morphological analysis of the cartilaginous and osseous curvature of the humeral head and the glenoid cavity*. *Journal of Orthopaedic Surgery and Research*, 2014. **9**.
90. Podolsky, D., et al., *Comparison of third toe joint cartilage thickness to that of the finger proximal interphalangeal (pip) joint to determine suitability for transplantation in pip joint reconstruction*. *Journal of Hand Surgery-American Volume*, 2011. **36A**(12): p. 1950-1958.
91. Arrieta, C., et al., *Quantitative assessments of geometric errors for rapid prototyping in medical applications*. *Rapid Prototyping Journal*, 2012. **18**(6): p. 431-442.
92. Hopper, K.D., et al., *The quality of 3d reconstructions from 1.0 and 1.5 pitch helical and conventional ct*. *Journal of Computer Assisted Tomography*, 1996. **20**(5): p. 841-847.
93. Huotilainen, E., et al., *Inaccuracies in additive manufactured medical skull models caused by the dicom to stl conversion process*. *Journal of Cranio-Maxillofacial Surgery*, 2014. **42**(5): p. E259-E265.
94. Clark, J. and J. Huber, *The structure of the human subchondral plate*. *J Bone Joint Surg Br*, 1990. **72-B**(5): p. 866-873.
95. Liptak, J.M., et al., *Cortical allograft and endoprosthesis for limb-sparing surgery in dogs with distal radial osteosarcoma: A prospective clinical comparison of two different limb-sparing techniques*. *Vet Surg*, 2006. **35**(6): p. 518-33.
96. Herzberg, G., et al., *Primary wrist hemiarthroplasty for irreparable distal radius fracture in the independent elderly*. *J Wrist Surg*, 2015. **4**(3): p. 156-63.
97. Cohnen, M., et al., *Effective doses in standard protocols for multi-slice ct scanning*. *Eur Radiol*, 2003. **13**(5): p. 1148-1153.
98. Brooks, R.A. and G.D. Chiro, *Beam hardening in x-ray reconstructive tomography*. *Phys Med Biol*, 1976. **21**(3): p. 390.
99. Joseph, P.M. and C. Ruth, *A method for simultaneous correction of spectrum hardening artifacts in ct images containing both bone and iodine*. *Med Phys*, 1997. **24**(10): p. 1629-1634.
100. Tan, Y., et al., *Simulation-aided investigation of beam hardening induced errors in ct dimensional metrology*. *Meas Sci Technol*, 2014. **25**(6).

101. Zhang, X., et al., *Improving the accuracy of ct dimensional metrology by a novel beam hardening correction method*. Meas Sci Technol, 2015. **26**(1): p. 1-11.
102. Krumm, M., S. Kasperl, and M. Franz, *Reducing non-linear artifacts of multi-material objects in industrial 3d computed tomography*. NDT E Int, 2008. **41**(4): p. 242-251.
103. Kohonen, I., et al., *Total ankle arthroplasty: Optimizing computed tomography imaging protocol*. Skeletal Radiol, 2013. **42**(11): p. 1507-1513.
104. Rathnayaka, K., et al., *Effects of ct image segmentation methods on the accuracy of long bone 3d reconstructions*. Med Eng Phys, 2011. **33**(2): p. 226-233.
105. Eggers, G., et al., *Geometric accuracy of digital volume tomography and conventional computed tomography*. Br J Oral Maxillofac Surg, 2008. **46**(8): p. 639-644.
106. Van den Broeck, J., et al., *Segmentation accuracy of long bones*. Med Eng Phys, 2014. **36**(7): p. 949-953.
107. McCann, L., et al., *An investigation of the effect of conformity of knee hemiarthroplasty designs on contact stress, friction and degeneration of articular cartilage: A tribological study*. J Biomech, 2009. **42**(9): p. 1326-1331.
108. Brand, J., et al., *Graft fixation in cruciate ligament reconstruction*. The American Journal of Sports Medicine, 2000. **28**(5): p. 761-774.
109. Reach Jr, J.S., et al., *Direct tendon attachment and healing to porous tantalum: An experimental animal study*. The Journal of Bone & Joint Surgery, 2007. **89**(5): p. 1000-1009.
110. Shetye, S.S., et al., *Determination of mechanical properties of canine carpal ligaments*. American Journal of Veterinary Research, 2009. **70**(8): p. 1026.
111. Voss, K., H. Geyer, and P.M. Montavon, *Antebrachiocarpal luxation in a cat a case report and anatomical study of the medial collateral ligament*. Veterinary and Comparative Orthopaedics and Traumatology (VCOT), 2003(4): p. 266-.
112. Streubel, R., M. Makara, and T. Guerrero, *Medial radio-carpal arthrodesis in three cats with a 2.0 mm locking maxillofacial plate system*. Veterinary and Comparative Orthopaedics and Traumatology (VCOT), 2011. **24**(4): p. 294-298.
113. Nakladal, B., et al., *Carpal joint injuries in cats – an epidemiological study*. Veterinary and Comparative Orthopaedics and Traumatology (VCOT), 2013. **26**(5): p. 333-339.
114. Whitney, W.O. and C.J. Mehlhaff, *High-rise syndrome in cats*. Journal of the American Veterinary Medical Association, 1987. **191**(11): p. 1399.
115. Corr, S., *Intensive, extensive, expensive. Management of distal limb shearing injuries in cats*. Journal of Feline Medicine and Surgery, 2009. **11**(9): p. 747-757.
116. Calvo, I., et al., *Carpal arthrodesis in cats*. Veterinary and Comparative Orthopaedics and Traumatology (VCOT), 2009(6): p. 498-504.
117. Nicholson, I., et al., *Feline talocrural luxation: A cadaveric study of repair using ligament prostheses*. Veterinary and Comparative Orthopaedics and Traumatology (VCOT), 2012. **25**(2): p. 116-125.
118. Gottsauner-Wolf, F., et al., *Fixation of canine tendons to metal*. Acta orthopaedica Scandinavica, 1994. **65**(2): p. 179-184.

119. Inoue, N., et al., *Biologic tendon fixation to metallic implant augmented with autogenous cancellous bone graft and bone marrow in a canine model*. Journal of Orthopaedic Research, 2002. **20**(5): p. 957-966.
120. Higuera, C.A., et al., *Tendon reattachment to a metallic implant using an allogenic bone plate augmented with rhop-1 vs. Autogenous cancellous bone and marrow in a canine model*. J Orthop Res, 2005. **23**(5): p. 1091-9.
121. Ari Itala, M., et al., *Successful canine patellar tendon reattachment to porous tantalum*. Clinical Orthopaedics and Related Research, 2007. **463**: p. 6.
122. Temenoff, J.S. and A.G. Mikos, *Review: Tissue engineering for regeneration of articular cartilage*. Biomaterials, 2000. **21**(5): p. 431-440.
123. Newman, A.P., *Articular cartilage repair*. American Journal of Sports Medicine, 1998. **26**(2): p. 309-324.
124. Stockwell, R.A., *The interrelationship of cell density and cartilage thickness in mammalian articular cartilage*. Journal of Anatomy, 1971. **109**(Pt 3): p. 411-421.
125. Malda, J., et al., *Of mice, men and elephants: The relation between articular cartilage thickness and body mass: E57683*. 2013. **8**(2).
126. Frisbie, D.D., M.W. Cross, and C.W. McIlwraith, *A comparative study of articular cartilage thickness in the stifle of animal species used in human pre-clinical studies compared to articular cartilage thickness in the human knee*. Veterinary and Comparative Orthopaedics and Traumatology (VCOT), 2006. **19**(3): p. 142-146.
127. Shepherd, D.E.T. and B.B. Seedhom, *Thickness of human articular cartilage in joints of the lower limb*. Annals of the Rheumatic Diseases, 1999. **58**(1): p. 27-34.
128. Athanasiou, K.A., et al., *Interspecies comparisons of insitu intrinsic mechanical-properties of distal femoral cartilage*. Journal of Orthopaedic Research, 1991. **9**(3): p. 330-340.
129. Herzog, W., et al., *Material and functional properties of articular cartilage and patellofemoral contact mechanics in an experimental model of osteoarthritis*. Journal of Biomechanics, 1998. **31**(12): p. 1137-1145.
130. Athanasiou, K.A., A. Agarwal, and F.J. Dzida, *Comparative-study of the intrinsic mechanical-properties of the human acetabular and femoral-head cartilage*. Journal of Orthopaedic Research, 1994. **12**(3): p. 340-349.
131. Korhonen, R.K., et al., *Comparison of the equilibrium response of articular cartilage in unconfined compression, confined compression and indentation*. Journal of Biomechanics, 2002. **35**(7): p. 903-909.
132. Camarero-Espinosa, S., et al., *Articular cartilage: From formation to tissue engineering*. Biomaterials Science, 2016. **4**(5): p. 734-767.
133. Mow, V.C., A. Ratcliffe, and A.R. Poole, *Cartilage and diarthrodial joints as paradigms for hierarchical materials and structures*. Biomaterials, 1992. **13**(2): p. 67-97.
134. Konkel, K.F. and A.G. Menger, *Mid-term results of titanium hemi-great toe implants*. Foot & ankle international, 2006. **27**(11): p. 922-929.
135. Turner, T.M., et al., *Bone ingrowth through porous titanium granulate around a femoral stem - histological assessment in a six-month canine hemiarthroplasty model*. Upsala Journal of Medical Sciences, 2007. **112**(2): p. 191-197.

136. Dalldorf, P.G., et al., *Rate of degeneration of human acetabular cartilage after hemiarthroplasty*. Journal of Bone and Joint Surgery-American Volume, 1995. **77A**(6): p. 877-882.
137. Field, J.R., et al., *Early acetabular cartilage wear following hemiarthroplasty: An ovine model*. Veterinary and Comparative Orthopaedics and Traumatology, 2016. **29**(2): p. 125-130.
138. Kaneko, K., et al., *Japanese acrylic hemi-arthroplasty of the hip with a 45-year follow-up without revision*. Archives of orthopaedic and trauma surgery, 2002. **122**(5): p. 299-301.
139. Daniels, T.R., et al., *Midterm outcomes of polyvinyl alcohol hydrogel hemiarthroplasty of the first metatarsophalangeal joint in advanced hallux rigidus*. Foot & ankle international, 2017. **38**(3): p. 243-247.
140. Bernasek, T.L., J.L. Stahl, and D. Pupello, *Pyrolytic carbon endoprosthetic replacement for osteonecrosis and femoral fracture of the hip: A pilot study*. Clinical Orthopaedics and Related Research, 2009. **467**(7): p. 1826-1832.
141. Kim, Y.S., et al., *The cartilage degeneration and joint motion of bipolar hemiarthroplasty*. International Orthopaedics, 2012. **36**(10): p. 2015-2020.
142. Jung, M., et al., *Comparison of cobalt chromium, ceramic and pyrocarbon hemiprostheses in a rabbit model: Ceramic leads to more cartilage damage than cobalt chromium*. Journal of Biomedical Materials Research Part B: Applied Biomaterials, 2008. **85B**(2): p. 427-434.
143. Katta, J., et al., *Biotribology of articular cartilage—a review of the recent advances*. Medical Engineering and Physics, 2008. **30**(10): p. 1349-1363.
144. Jia, L.Z., et al., *Effect of clearance on cartilage tribology in hip hemi-arthroplasty*. Proceedings of the Institution of Mechanical Engineers Part H-Journal of Engineering in Medicine, 2013. **227**(12): p. 1284-1291.
145. McCann, L., et al., *An investigation of the effect of conformity of knee hemiarthroplasty designs on contact stress, friction and degeneration of articular cartilage: A tribological study*. Journal of Biomechanics, 2009. **42**(9): p. 1326-1331.
146. Müller, L.P., et al., *Friction of ceramic and metal hip hemi-endoprostheses against cadaveric acetabula*. Archives of orthopaedic and trauma surgery, 2004. **124**(10): p. 681-687.
147. Patel, A.M. and M. Spector, *Tribological evaluation of oxidized zirconium using an articular cartilage counterface: A novel material for potential use in hemiarthroplasty*. Biomaterials, 1997. **18**(5): p. 441-447.
148. Chan, S.M.T., et al., *Friction and wear of hemiarthroplasty biomaterials in reciprocating sliding contact with articular cartilage*. JOURNAL OF TRIBOLOGY-TRANSACTIONS OF THE ASME, 2011. **133**(4).
149. Baker, M.I., et al., *A review of polyvinyl alcohol and its uses in cartilage and orthopedic applications*. Journal of Biomedical Materials Research Part B-Applied Biomaterials, 2012. **100B**(5): p. 1451-1457.
150. Li, F., et al., *Influence of dynamic load on friction behavior of human articular cartilage, stainless steel and polyvinyl alcohol hydrogel as artificial cartilage*. Journal of Materials Science-Materials in Medicine, 2010. **21**(1): p. 147-154.

151. Li, F., A.M. Wang, and C.T. Wang, *Analysis of friction between articular cartilage and polyvinyl alcohol hydrogel artificial cartilage*. Journal of Materials Science-Materials in Medicine, 2016. **27**(5).
152. Maiolo, A.S., et al., *Development and characterization of poly (vinyl alcohol) based hydrogels for potential use as an articular cartilage replacement*. Materials Science & Engineering C-Materials for Biological Applications, 2012. **32**(6): p. 1490-1495.
153. Gonzalez, J.S. and V.A. Alvarez, *Mechanical properties of polyvinylalcohol/hydroxyapatite cryogel as potential artificial cartilage*. Journal of the Mechanical Behavior of Biomedical Materials, 2014. **34**: p. 47-56.
154. Katta, J.K., et al., *Friction and wear behavior of poly(vinyl alcohol)/poly(vinyl pyrrolidone) hydrogels for articular cartilage replacement*. Journal of Biomedical Materials Research Part A, 2007. **83A**(2): p. 471-479.
155. Ma, R., et al., *Novel pvp/pva hydrogels for articular cartilage replacement*. Materials Science & Engineering C, 2009. **29**(6): p. 1979-1983.
156. Spiller, K.L., et al., *Superporous hydrogels for cartilage repair: Evaluation of the morphological and mechanical properties*. Acta biomaterialia, 2008. **4**(1): p. 17-25.
157. Maher, S.A., et al., *Nondegradable hydrogels for the treatment of focal cartilage defects*. Journal of Biomedical Materials Research Part A, 2007. **83A**(1): p. 145-155.
158. Luo, Y., et al., *Polyurethane as a potential knee hemiarthroplasty biomaterial: An in-vitro simulation of its tribological performance*. Proceedings of the Institution of Mechanical Engineers, Part H: Journal of Engineering in Medicine, 2010. **224**(3): p. 415-425.
159. Mocerneac, B. and M. Lobontiu, *Aspects regarding the comparative study of the cryogenic and conventional milling of vulcanized rubber*. Scientific Bulletin Series C : Fascicle Mechanics, Tribology, Machine Manufacturing Technology, 2014. **28**: p. 69.
160. Mente, P.L. and J.L. Lewis, *Elastic modulus of calcified cartilage is an order of magnitude less than that of subchondral bone*. Journal of Orthopaedic Research, 1994. **12**(5): p. 637-647.
161. Shi, Y., et al., *Effects of polymerization degree on recovery behavior of pva/pvp hydrogels as potential articular cartilage prosthesis after fatigue test*. Express Polymer Letters, 2016. **10**(2): p. 125-138.
162. Lawless, B.M., et al., *Viscoelasticity of articular cartilage: Analysing the effect of induced stress and the restraint of bone in a dynamic environment*. Journal of the Mechanical Behavior of Biomedical Materials, 2017. **75**: p. 293-301.
163. Sing, S.L., et al., *Laser and electron-beam powder-bed additive manufacturing of metallic implants: A review on processes, materials and designs*. Journal of Orthopaedic Research, 2016. **34**(3): p. 369-385.
164. Simske, S.J., R.A. Ayers, and T.A. Bateman, *Porous materials for bone engineering*. Materials Science Forum, 1997. **250**: p. 151-182.
165. Cheah, C.M., et al., *Development of a tissue engineering scaffold structure library for rapid prototyping. Part 1: Investigation and classification*. The

- International Journal of Advanced Manufacturing Technology, 2003. **21**(4): p. 291-301.
166. Taniguchi, N., et al., *Effect of pore size on bone ingrowth into porous titanium implants fabricated by additive manufacturing: An in vivo experiment*. Materials Science and Engineering: C, 2016. **59**: p. 690-701.
 167. Harrysson, O.L.A., et al., *Direct metal fabrication of titanium implants with tailored materials and mechanical properties using electron beam melting technology*. Materials Science & Engineering C, 2008. **28**(3): p. 366-373.
 168. Heintl, P., et al., *Cellular ti-6al-4v structures with interconnected macro porosity for bone implants fabricated by selective electron beam melting*. Acta biomaterialia, 2008. **4**(5): p. 1536-1544.
 169. Weißmann, V., et al., *Influence of the structural orientation on the mechanical properties of selective laser melted ti6al4v open-porous scaffolds*. MATERIALS & DESIGN, 2016. **95**: p. 188-197.
 170. Mullen, L., et al., *Selective laser melting: A unit cell approach for the manufacture of porous, titanium, bone in-growth constructs, suitable for orthopedic applications. li. Randomized structures*. Journal of Biomedical Materials Research Part B: Applied Biomaterials, 2010. **92B**(1): p. 178-188.
 171. Arabnejad, S., et al., *Fully porous 3d printed titanium femoral stem to reduce stress-shielding following total hip arthroplasty*. Journal of Orthopaedic Research, 2016.

APPENDICES

Appendix A – Feline Radius Geometry Characterization Full Results

Specimen	ML Distance	CC Distance	Shaft Radius	Depth of Full Articular Surface	Depth of primary bearing region of articular surface
PID2	13.26	8.55	2.8133	2.79	1.36
PID3	12.18	8.16	2.1538	2.71	1.06
PID4	11.88	7.72	2.3889	2.91	1.39
PID5	13.49	8.48	2.6671	2.9	1.2
ID 103	12.09	7.80	2.6388	2.87	1.36
ID 107	11.81	7.58	2.1563	2.55	1.26
ID 108	11.01	6.98	2.1436	2.43	1.20
ID 111	11.88	7.77	2.2964	3.07	1.52
ID 113	11.74	7.54	2.2864	2.79	1.63
ID 118	12.44	8.53	2.6182	3.01	1.45
ID 119	12.30	8.33	2.7612	2.91	1.41
ID 120	12.04	8.27	2.7418	3.00	1.58
ID 123	13.68	9.13	3.556	3.28	1.53
ID 126	12.80	8.65	2.6487	3.25	1.57
ID 127	12.42	9.01	2.5801	3.08	1.36
ID 128	13.38	8.72	2.6536	3.22	1.42
ID 129	14.22	9.18	2.9901	3.08	1.75
ID 130	13.82	9.00	3.2352	2.75	1.51
ID 134	13.05	8.85	2.7156	3.04	1.75
ID 136	14.42	9.60	2.6977	3.32	1.43
ID 139	11.30	7.69	2.3085	2.64	1.31
ID 140	13.16	9.08	3.6237	3.02	1.42
ID 142	12.28	7.90	2.7373	2.85	1.2

Appendix B – Imaging Modality Comparison Full Results

ML Distance (mm)				
Specimen	Imaging Method			
	LaserScan	LongCT	TransCT	uCT
PID2	13.26	13.38	13.65	13.06
PID3	12.18	12.65	11.97	11.96
PID4	11.88	12.09	12.13	11.75
PID5	13.49	13.96	14.05	13.21
ID103	12.09	13.85	13.09	12.02
ID108	11.01	12.17	11.27	10.98
ID129	14.22	14.05	14.07	13.57
ID111	11.88	12.33	12.08	11.85
ID113	11.74	12.52	12.71	11.65
ID119	12.30	12.76	12.60	12.25
ID107	11.81	11.77	12.49	11.71
ID118	12.44	12.69	13.58	12.30
ID123	13.68	14.21	14.24	13.41
ID126	12.80	13.39	13.53	12.65
ID127	12.42	12.80	12.74	12.46
ID120	12.04	12.33	13.33	11.87
ID128	13.38	13.65	14.00	13.22
ID139	11.30	11.65	11.89	11.23
ID140	13.16	13.33	13.63	13.13
ID142	12.28	12.47	12.71	12.05
ID 136	14.42	14.43	14.01	13.83
ID130	13.82	14.17	14.42	13.65
ID 134	13.05	13.83	13.83	12.98

DP Distance (mm)				
Specimen	Imaging Method			
	LaserScan	LongCT	TransCT	uCT
PID2	8.55	8.96	9.33	8.55
PID3	8.16	8.40	8.58	8.11
PID4	7.72	8.20	8.72	7.71
PID5	8.48	8.91	8.98	8.27
ID103	7.80	8.28	8.29	7.67
ID108	6.98	7.43	7.57	7.01
ID129	9.18	9.91	9.86	9.17
ID111	7.77	8.25	8.69	7.90
ID113	7.54	8.13	8.31	7.66
ID119	8.33	8.91	9.14	8.31
ID107	7.58	8.07	8.53	7.61
ID118	8.53	9.44	9.25	8.54
ID123	9.13	9.49	9.80	8.98
ID126	8.65	9.02	9.78	8.60
ID127	9.01	9.30	9.84	9.06
ID120	8.27	8.92	9.73	8.24
ID128	8.72	9.14	9.87	8.70
ID139	7.69	7.95	8.51	7.72
ID140	9.08	9.43	10.07	9.09
ID142	7.90	8.65	8.68	7.80
ID 136	9.60	9.85	10.09	9.29
ID 130	9.00	9.36	9.99	8.91
ID134	8.85	9.80	10.03	8.83

Surface Deviation										
Sample ID	Reference Model	Test Model	Positive Deviation (mm)				Negative Deviation (mm)			
			Average	Maximum	Stdev	# of Points	Average	Minimum	Stdev	# of Points
PID2	LongCT	Laser	0.18262	2.285355	0.27701	590	-0.2383	-3.063294	0.12192	63437
PID3	LongCT	Laser	0.08427	0.515471	0.08106	9019	-0.1543	-2.264876	0.08981	50124
PID4	LongCT	Laser	0.05357	2.430489	0.06173	5508	-0.1829	-1.303797	0.10485	59396
PID5	LongCT	Laser	0.11424	0.819923	0.1203	3156	-0.251	-1.924576	0.12099	89475
103	LongCT	Laser	0.069235	2.654808	0.177318	1001	-0.2765	-1.498795	0.146331	36667
107	LongCT	Laser	0.057016	0.753084	0.076331	306	-	-2.629085	0.125896	34346
							0.28688			
108	LongCT	Laser	0.225788	2.051202	0.227128	308	-	-2.747265	0.126846	62794
							0.31644			
111	LongCT	Laser	0.078324	4.700631	0.187295	3507	-	-4.149294	0.107168	48747
							0.17851			
113	LongCT	Laser	0.109054	2.154763	0.148492	1794	-	-3.674514	0.16675	63573
							0.32118			
118	LongCT	Laser	0.073848	1.757044	0.068486	5625	-0.1788	-5.404297	0.10675	69869
119	LongCT	Laser	0.104236	1.832558	0.107932	4361	-	-3.347239	0.104542	80951
							0.21045			
120	LongCT	Laser	0.082986	0.755092	0.086515	5780	-	-1.942875	0.114519	115063
							0.23663			
123	LongCT	Laser	0.153634	0.971414	0.102644	34620	-0.2613	-3.384169	0.149842	93977
126	LongCT	Laser	0.20261	0.950526	0.162506	2559	-	-3.734279	0.138954	106592
							0.30819			
127	LongCT	Laser	0.093637	1.753091	0.0869	14657	-	-4.944293	0.125471	79641
							0.18806			
128	LongCT	Laser	0.051442	0.920683	0.077202	4467	-0.2613	-4.213857	0.155949	63333
129	LongCT	Laser	0.145744	3.266986	0.288245	1521	-	-2.569733	0.172609	79501
							0.32797			
139	LongCT	Laser	0.116753	3.628988	0.189825	2018	-	-4.607864	0.102437	127805
							0.27536			
140	LongCT	Laser	0.288983	2.665551	0.31475	276	-	-2.99948	0.115377	75623
							0.25694			

142	LongCT	Laser	0.464	2.3214	0.30486	71194	- 0.14879	-3.765	0.20921	11733
PID2	TransCT	Laser	0.06905	2.340879	0.1687	4084	-0.219	-3.368239	0.16942	59943
PID3	TransCT	Laser	0.03913	1.869127	0.05441	13861	-0.0706	-1.794232	0.05773	45335
PID4	TransCT	Laser	0.03245	1.371386	0.04006	5550	-0.1262	-2.186583	0.08219	59288
PID5	TransCT	Laser	0.04116	0.570929	0.04796	6842	-0.1762	-2.802544	0.10135	85739
103	TransCT	Laser	0.075927	1.654894	0.096061	4137	- 0.24036	-2.157791	0.155633	33553
107	TransCT	Laser	0.346837	1.340753	0.219794	415	- 0.30473	-1.91752	0.141922	34255
108	TransCT	Laser	0.148898	0.878542	0.187803	733	- 0.26349	-1.929766	0.132948	62354
111	TransCT	Laser	0.171079	0.756963	0.178305	1837	- 0.18983	-1.474495	0.121311	50435
113	TransCT	Laser	0.227633	1.657841	0.255622	6411	- 0.30441	-2.602565	0.198078	58969
118	TransCT	Laser	0.071245	2.157156	0.083317	9123	- 0.19926	-2.534296	0.126964	66371
119	TransCT	Laser	0.197573	1.4377	0.166523	1572	- 0.18913	-1.984989	0.094672	83770
120	TransCT	Laser	0.100092	1.24635	0.086083	11441	- 0.24533	-1.319928	0.113202	109442
123	TransCT	Laser	0.229413	2.417458	0.189926	32432	- 0.26817	-1.614221	0.154752	96226
126	TransCT	Laser	0.294046	1.521513	0.327445	5580	- 0.31222	-2.16036	0.201147	103512
127	TransCT	Laser	0.104958	0.600921	0.097128	22330	- 0.19052	-1.87656	0.106618	71996
128	TransCT	Laser	0.098396	2.07483	0.111515	6506	- 0.24366	-2.401361	0.126242	61269
129	TransCT	Laser	0.067218	0.805164	0.086159	6818	- 0.21059	-4.022655	0.14974	74224
139	TransCT	Laser	0.136866	1.004891	0.210837	613	-0.3092	-4.297903	0.13089	129228
140	TransCT	Laser	0.135036	3.008722	0.327444	272	- 0.25087	-3.252806	0.118211	75626
142	TransCT	Laser	0.1183	0.9323	0.46045	81346	0.1235	2.9783	0.57932	1442
PID2	uCT	Laser	0.01912	0.194829	0.01756	34910	-0.0181	-0.665761	0.02336	29042

PID3	uCT	Laser	0.02346	0.321626	0.0177	32264	-0.0243	-0.484138	0.02105	27509
PID4	uCT	Laser	0.01761	0.253755	0.01794	30763	-0.0161	-0.294615	0.0171	33843
PID5	uCT	Laser	0.0179	0.165388	0.01288	58529	-0.0163	-0.323898	0.01601	33744
103	uCT	Laser	0.058109	0.25053	0.047668	33259	-	-0.274026	0.017043	4353
							0.01519			
107	uCT	Laser	0.033443	0.265637	0.019374	31675	-	-0.354231	0.024395	2938
							0.01443			
108	uCT	Laser	0.021476	0.15994	0.016379	23567	-	-0.156104	0.021578	39348
							0.03341			
111	uCT	Laser	0.028993	0.244298	0.020299	32845	-	-0.547348	0.02355	19373
							0.02446			
113	uCT	Laser	0.040002	0.26104	0.024332	35843	-	-0.660316	0.033813	29440
							0.04146			
118	uCT	Laser	0.011376	0.356321	0.012948	8642	-	-0.372055	0.020032	66855
							0.03267			
119	uCT	Laser	0.023814	0.230912	0.017518	57503	-	-0.368456	0.017111	27747
							0.01771			
120	uCT	Laser	0.027924	0.149769	0.022814	63689	-	-0.358747	0.016882	57021
							0.02081			
123	uCT	Laser	0.097456	0.325258	0.050793	123436	-	-0.335778	0.031672	5254
							0.03082			
126	uCT	Laser	0.071259	0.256254	0.051813	85816	-	-0.401638	0.027385	23298
							0.03108			
127	uCT	Laser	0.020778	0.284841	0.017125	54653	-	-0.260867	0.012344	39525
							0.01559			
128	uCT	Laser	0.031922	0.369637	0.02457	46742	-	-0.402396	0.02215	20808
							0.02423			
129	uCT	Laser	0.037647	0.181788	0.02741	54983	-	-0.390348	0.025351	26031
							0.02733			
139	uCT	Laser	0.018991	0.173425	0.017298	43996	-	-0.216675	0.023574	85586
							0.03051			
140	uCT	Laser	0.036879	0.232938	0.02161	62542	-	-0.189108	0.016616	13314
							0.01819			
142	uCT	Laser	0.021322	0.30719	0.018594	24667	-	-0.43262	0.028531	57919
							0.03966			

ID103 Radius of Curvature Comparison								
Name	LongCT	LS (LongCT)	Name	TransCT	LS (TransCT)	Name	uCT	LS (uCT)
DP	3.1419	2.3386	DP	3.2064	2.3386	DP	2.4089	2.3386
DP1	3.2204	2.6967	DP1	3.5612	2.6967	DP1	2.6989	2.6967
DP2	3.6964	2.487	DP2	3.7181	2.487	DP2	2.8961	2.487
DP3	2.2868	2.077	DP3	1.4886	2.077	DP3	1.7981	2.077
DP4	41.0931	35.6328	DP4	9.4352	35.6328	DP4	25.2475	35.6328
DP5	7.6689	7.9745	DP5	14.1978	7.9745	DP5	6.7984	7.9745
DP6	7.8265	4.9176	DP6	40.2792	4.9176	DP6	6.6848	4.9176
DP7	6.2704	3.9861	DP7	19.7715	3.9861	DP7	4.0809	3.9861
DP8	4.2033	3.399	DP8	4.2547	3.399	DP8	3.6136	3.399
DP9	3.2925	3.5895	DP9	3.1112	3.5895	DP9	3.5872	3.5895
DP10	1.9351	3.5482	DP10	3.0263	3.5482	DP10	3.6098	3.5482
DP11	2.8309	3.32	DP11	3.5702	3.32	DP11	3.3865	3.32
DP12	1.9166	2.9356	DP12	3.2048	2.9356	DP12	3.0686	2.9356
ML	16.5521	27.0972	ML	14.3531	27.0972	ML	27.3412	27.0972
ML1	5.2074	9.0267	ML1	6.5986	9.0267	ML1	10.8597	9.0267
ML2	5.5746	6.5521	ML2	6.7471	6.5521	ML2	6.6106	6.5521
ML3	6.4068	5.8339	ML3	6.1194	5.8339	ML3	5.8929	5.8339
ML4	6.169	5.4545	ML4	5.4827	5.4545	ML4	5.4229	5.4545
ML5	5.065	5.1927	ML5	4.9281	5.1927	ML5	5.1204	5.1927
ML6	4.6183	4.8149	ML6	4.904	4.8149	ML6	4.8979	4.8149
ML7	4.7635	4.2535	ML7	5.3349	4.2535	ML7	4.4199	4.2535
ML8	3.9966	3.1333	ML8	3.6397	3.1333	ML8	2.9822	3.1333

ID107 Radius of Curvature Comparison								
Name	LongCT	LS (LongCT)	Name	TransCT	LS (TransCT)	Name	uCT	LS (uCT)
DP	2.2868	2.1241	DP	3.5469	2.1241	DP	2.0798	2.1241
DP1	2.3886	2.1991	DP1	4.487	2.1991	DP1	2.1981	2.1991
DP2	1.5973	7.3246	DP2	2.9444	7.3246	DP2	6.5816	7.3246
DP3	3.6925	2.1747	DP3	11.9291	2.1747	DP3	1.376	2.1747
DP4	47.2093	6.9235	DP4	2.1434	6.9235	DP4	7.0013	6.9235
DP5	4.704	3.9313	DP5	1.5399	3.9313	DP5	3.7351	3.9313
DP6	3.6541	4.3012	DP6	2.5971	4.3012	DP6	4.1158	4.3012
DP7	2.9551	3.4451	DP7	4.1684	3.4451	DP7	3.3569	3.4451
DP8	2.2778	3.4505	DP8	3.9704	3.4505	DP8	3.3546	3.4505

DP9	2.2821	3.6247	DP9	3.0861	3.6247	DP9	3.3983	3.6247
DP10	2.9908	3.8523	DP10	3.4561	3.8523	DP10	3.6114	3.8523
DP11	3.5036	3.4816	DP11	3.0016	3.4816	DP11	3.3786	3.4816
DP12	3.6548	2.9711	DP12	2.311	2.9711	DP12	2.9087	2.9711
DP13	3.0531	2.5814	DP13	5.9888	2.5814	DP13	2.4412	2.5814
DP14	2.5965	3.0305	DP14	1.3476	3.0305	DP14	2.6926	3.0305
DP15	3.9397	6.0237	DP15	0.4734	6.0237	DP15	4.8841	6.0237
ML	6.7358	6.9909	ML	1.5119	6.9909	ML	7.2097	6.9909
ML1	6.196	9.8558	ML1	4.642	9.8558	ML1	10.082	9.8558
ML2	5.5377	6.0457	ML2	6.3142	6.0457	ML2	6.1263	6.0457
ML3	5.6794	5.945	ML3	6.2553	5.945	ML3	6.0053	5.945
ML4	4.9218	5.8053	ML4	6.026	5.8053	ML4	5.8094	5.8053
ML5	5.0036	5.4792	ML5	5.638	5.4792	ML5	5.4355	5.4792
ML6	4.7942	5.3238	ML6	6.6717	5.3238	ML6	5.3504	5.3238
ML7	5.0402	5.1262	ML7	6.8632	5.1262	ML7	5.1067	5.1262
ML8	4.0783	3.9617	ML8	4.1322	3.9617	ML8	3.6017	3.9617
ML9	3.5678	3.3987				ML9	3.6437	3.3987

ID108 Radius of Curvature Comparison								
Name	LongCT	LS (Long CT)	Name	TransCT	LS (TransCT)	Name	uCT	LS (uCT)
DP	3.5563	2.3031	DP	3.4546	2.3031	DP	2.2889	2.3031
DP1	3.8401	2.4893	DP1	6.4337	2.4893	DP1	2.6959	2.4893
DP2	3.526	2.7831	DP2	37.7691	2.7831	DP2	3.0095	2.7831
DP3	2.6678	2.8719	DP3	294.6203	2.8719	DP3	3.4878	2.8719
DP5	5.2045	1.5064	DP5	1.3861	1.5064	DP5	1.6316	1.5064
DP6	4.4062	4.0398	DP6	1.5714	4.0398	DP6	4.0151	4.0398
DP7	2.3321	3.4164	DP7	2.5253	3.4164	DP7	3.3768	3.4164
DP8	2.432	3.7314	DP8	2.8683	3.7314	DP8	3.6799	3.7314
DP9	2.9774	3.7381	DP9	2.7681	3.7381	DP9	3.605	3.7381

DP10	2.9852	3.5277	DP10	3.6523	3.5277	DP10	3.393	3.5277
DP11	2.6631	3.0778	DP11	4.9334	3.0778	DP11	2.9202	3.0778
DP12	1.7077	2.4858	DP12	6.7683	2.4858	DP12	2.2847	2.4858
ML	4.869	10.7382	ML	8.2612	10.7382	ML	9.9939	10.7382
ML1	6.0958	6.3227	ML1	5.5083	6.3227	ML1	5.9604	6.3227
ML2	5.2929	5.6857	ML2	5.8656	5.6857	ML2	5.695	5.6857
ML3	5.2947	5.332	ML3	5.9326	5.332	ML3	5.4364	5.332
ML4	4.4707	5.0439	ML4	6.7949	5.0439	ML4	5.1222	5.0439
ML5	3.5729	4.8192	ML5	6.8074	4.8192	ML5	4.9147	4.8192
ML6	3.9694	4.0357	ML6	6.9718	4.0357	ML6	4.0489	4.0357
ML7	3.0945	2.7651	ML7	3.6006	2.7651	ML7	2.6919	2.7651

ID111 Radius of Curvature Comparison								
Name	LongCT	LS (Long CT)	Name	TransCT	LS (TransCT)	Name	uCT	LS (uCT)
DP	2.2436	2.096	DP	2.2675	2.096	DP	2.0895	2.096
DP1	2.4876	2.5166	DP1	2.3389	2.5166	DP1	2.5291	2.5166
DP2	2.8002	3.3211	DP2	3.1701	3.3211	DP2	3.3393	3.3211
DP3	2.2183	22.0022	DP3	2.6449	22.0022	DP3	18.4019	22.0022
DP4	1.4133	3.2841	DP4	3.6684	3.2841	DP4	4.4945	3.2841
DP5	3.2102	7.5946	DP5	2.8955	7.5946	DP5	7.4568	7.5946
DP6	4.8562	5.6444	DP6	2.5601	5.6444	DP6	5.1114	5.6444
DP7	2.8146	4.01	DP7	3.2277	4.01	DP7	3.8423	4.01
DP8	3.18	3.723	DP8	3.3247	3.723	DP8	3.5289	3.723
DP9	4.6593	3.5755	DP9	4.0111	3.5755	DP9	3.3957	3.5755
DP10	4.7698	3.5146	DP10	3.679	3.5146	DP10	3.4258	3.5146
DP11	23.6271	3.7193	DP11	2.8754	3.7193	DP11	3.2989	3.7193
DP12	3.0515	3.1614	DP12	2.7621	3.1614	DP12	2.8983	3.1614
DP13	2.9731	2.873	DP13	2.1904	2.873	DP13	2.3598	2.873
ML	25.217	42.1693	ML	5.1846	42.1693	ML	128.7435	42.1693
ML1	11.3608	8.1434	ML1	5.7035	8.1434	ML1	8.3822	8.1434
ML2	5.0759	6.0613	ML2	5.129	6.0613	ML2	5.8959	6.0613
ML3	4.6157	5.55	ML3	4.9516	5.55	ML3	5.5528	5.55
ML4	5.2133	5.4597	ML4	4.814	5.4597	ML4	5.4368	5.4597
ML5	2.5724	5.1669	ML5	4.0836	5.1669	ML5	5.1446	5.1669
ML6	2.6044	4.8443	ML6	5.218	4.8443	ML6	4.8302	4.8443

ML7	4.0723	4.6188	ML7	4.228	4.6188	ML7	4.5877	4.6188
ML8	4.2085	4.2723	ML8	3.5515	4.2723	ML8	3.6712	4.2723
ML9	2.428	7.3996	ML9	0.9082	7.3996	ML9	8.3197	7.3996

ID 119 Radius of Curvature Comparison								
Name	LongCT	LS (LongCT)	Name	TransCT	LS (TransCT)	Name	uCT	LS(uCT)
DP	2.2481	1.812	DP	1.8842	1.812	DP	1.8744	1.812
DP1	2.2335	1.9943	DP1	2.1248	1.9943	DP1	1.9013	1.9943
DP2	2.3875	2.1017	DP2	2.3417	2.1017	DP2	2.0429	2.1017
DP3	2.5669	2.2552	DP3	2.3453	2.2552	DP3	2.2234	2.2552
DP4	3.0786	2.9094	DP4	3.8207	2.9094	DP4	2.8853	2.9094
DP5	3.3822	3.7691	DP5	5.3789	3.7691	DP5	3.7055	3.7691
DP6	1.4685	2.029	DP6	3.7406	2.029	DP6	1.8909	2.029
DP7	3.2815	5.7876	DP7	6.3002	5.7876	DP7	5.6752	5.7876
DP8	3.571	4.3777	DP8	4.503	4.3777	DP8	4.7274	4.3777
DP9	3.8216	3.6608	DP9	4.2466	3.6608	DP9	3.5878	3.6608
DP10	3.6996	3.5968	DP10	4.3282	3.5968	DP10	3.4432	3.5968
DP11	3.5455	3.4199	DP11	3.0258	3.4199	DP11	3.3126	3.4199
DP12	2.9592	3.2372	DP12	3.4531	3.2372	DP12	3.1767	3.2372
DP13	3.5738	2.9091	DP13	3.3352	2.9091	DP13	2.8675	2.9091
DP14	2.5258	2.5977	DP14	4.0646	2.5977	DP14	2.5005	2.5977
DP15	2.0518	2.5488	DP15	1.9103	2.5488	DP15	2.1508	2.5488
DP16	4.416	3.8105	DP16	3.042	3.8105	DP16	3.2696	3.8105
DP17	N/A	N/A	DP17	3.0031	2.5558	DP17	2.5876	2.5558
ML	2.5728	2.6668	ML	2.3268	2.6668	ML	2.8094	2.6668
ML1	2.7747	2.0505	ML1	2.2795	2.0505	ML1	1.9972	2.0505
ML2	8.8052	8.0758	ML2	4.6685	8.0758	ML2	7.8248	8.0758
ML3	4.8321	5.3303	ML3	4.3472	5.3303	ML3	5.1534	5.3303
ML4	5.2475	5.3388	ML4	4.8001	5.3388	ML4	5.2531	5.3388
ML5	5.3662	5.6303	ML5	5.0349	5.6303	ML5	5.6926	5.6303
ML6	4.6199	5.2879	ML6	5.0046	5.2879	ML6	5.4709	5.2879
ML7	4.2242	5.1414	ML7	4.8399	5.1414	ML7	5.2778	5.1414
ML8	5.4995	5.8079	ML8	4.5443	5.8079	ML8	6.1238	5.8079
ML9	5.1601	6.5855	ML9	5.2458	6.5855	ML9	7.3177	6.5855

ID120 Radius of Curvature Comparison								
Name	LongCT	LS (LongCT)	Name	TransCT	LS(TransCT)	Name	uCT	LS (uCT)
DP	2.6897	2.3036	DP	2.4122	2.3036	DP	2.2505	2.3036

DP1	3.1037	2.905	DP1	2.855	2.905	DP1	2.8531	2.905
DP2	3.3327	3.2494	DP2	3.338	3.2494	DP2	3.2432	3.2494
DP3	3.7733	3.1116	DP3	1.5116	3.1116	DP3	2.7381	3.1116
DP4	2.9498	100.0838	DP4	2.9037	100.0838	DP4	37.7598	100.0838
DP5	8.3476	13.2222	DP5	70.3426	13.2222	DP5	12.5062	13.2222
DP6	6.9793	5.4664	DP6	4.1233	5.4664	DP6	5.6062	5.4664
DP7	4.6759	3.7878	DP7	4.0938	3.7878	DP7	3.7472	3.7878
DP8	2.721	3.2043	DP8	2.8743	3.2043	DP8	3.0883	3.2043
DP9	3.362	3.1403	DP9	2.5364	3.1403	DP9	3.231	3.1403
DP10	4.1945	3.0061	DP10	2.9095	3.0061	DP10	3.3678	3.0061
DP11	3.9912	3.3136	DP11	3.2645	3.3136	DP11	3.3043	3.3136
DP12	4.6887	2.8116	DP12	2.8639	2.8116	DP12	2.8337	2.8116
DP13	3.7728	2.4171	DP13	2.7995	2.4171	DP13	2.1854	2.4171
DP14	0.8831	2.5564	DP14	0.7917	2.5564	DP14	2.2793	2.5564
DP15	2.3355	2.2352	DP15	N/A	N/A	DP15	2.1419	2.2352
ML	4.6376	4.1797	ML	4.1168	4.1797	ML	3.9214	4.1797
ML1	3.6423	4.6161	ML1	4.2732	4.6161	ML1	4.43	4.6161
ML2	4.7262	4.777	ML2	4.9207	4.777	ML2	4.8035	4.777
ML3	4.8514	5.0462	ML3	5.424	5.0462	ML3	4.9659	5.0462
ML4	4.6373	5.0578	ML4	4.5042	5.0578	ML4	4.9978	5.0578
ML5	4.9925	5.1245	ML5	4.6891	5.1245	ML5	5.0754	5.1245
ML6	5.5234	5.6167	ML6	5.8792	5.6167	ML6	5.6089	5.6167
ML7	7.7643	7.3665	ML7	7.0151	7.3665	ML7	7.3004	7.3665

ID123 Radius of Curvature Comparison								
Name	LongCT	LS (LongCT)	Name	TransCT	LS(TransCT)	Name	uCT	LS (uCT)
DP	2.3436	2.4577	DP	2.663	2.4577	DP	2.375	2.4577
DP1	2.5404	2.5911	DP1	2.5699	2.5911	DP1	2.5239	2.5911
DP2	2.7539	2.5765	DP2	2.9042	2.5765	DP2	2.7538	2.5765
DP3	1.3289	1.6785	DP3	1.2973	1.6785	DP3	1.6377	1.6785
DP4	1.9749	5.5049	DP4	1.3942	5.5049	DP4	4.3384	5.5049

DP5	9.8129	14.2447	DP5	2.3204	14.2447	DP5	7.9497	14.2447
DP6	3.9397	6.0824	DP6	4.2676	6.0824	DP6	5.7093	6.0824
DP7	3.628	5.3266	DP7	5.0337	5.3266	DP7	5.441	5.3266
DP8	4.2096	4.5912	DP8	3.9299	4.5912	DP8	4.5637	4.5912
DP9	3.4641	4.2176	DP9	3.5939	4.2176	DP9	4.2114	4.2176
DP10	2.7928	3.8551	DP10	4.4118	3.8551	DP10	3.7459	3.8551
DP11	2.6882	3.5275	DP11	4.3016	3.5275	DP11	3.4901	3.5275
DP12	2.8454	3.5566	DP12	3.1219	3.5566	DP12	3.4278	3.5566
DP13	2.5735	3.4201	DP13	3.1412	3.4201	DP13	3.0931	3.4201
DP14	2.178	2.7958	DP14	2.2927	2.7958	DP14	2.5004	2.7958
DP15	1.7505	2.1898	DP15	2.121	2.1898	DP15	2.0631	2.1898
DP16	1.6332	2.7683	DP16	2.6376	2.7683	DP16	2.8568	2.7683
ML	N/A	N/A	ML	8.3399	9.3656	ML	11.8525	9.3656
ML1	5.5257	5.7755	ML1	5.523	5.7755	ML1	5.8325	5.7755
ML2	5.6617	5.7993	ML2	5.4257	5.7993	ML2	5.6822	5.7993
ML3	5.7142	5.6628	ML3	5.4204	5.6628	ML3	5.7253	5.6628
ML4	5.69	5.9365	ML4	5.1398	5.9365	ML4	5.8366	5.9365
ML5	4.9926	5.8618	ML5	4.8797	5.8618	ML5	5.7973	5.8618
ML6	5.2032	5.8116	ML6	4.7319	5.8116	ML6	5.5928	5.8116
ML7	4.8921	5.6331	ML7	5.368	5.6331	ML7	5.5969	5.6331
ML8	4.6217	5.4922	ML8	4.9443	5.4922	ML8	5.5438	5.4922
ML9	4.5379	5.8671	ML9	6.09	5.8671	ML9	6.613	5.8671
ML10	4.1028	4.2416	ML10	4.3093	4.2416	ML10	4.3247	4.2416

ID127 Radius of Curvature Comparison								
Name	LongCT	LS (LongCT)	Name	TransCT	LS(TransCT)	Name	uCT	LS (uCT)
DP	2.1875	2.1281	DP	2.6609	2.1281	DP	2.0507	2.1281
DP1	2.9413	2.6006	DP1	2.6508	2.6006	DP1	2.5446	2.6006
DP2	3.3813	2.9397	DP2	3.3048	2.9397	DP2	3	2.9397
DP3	2.5739	2.7886	DP3	2.4312	2.7886	DP3	2.7723	2.7886
DP4	5.6303	3.7917	DP4	2.2295	3.7917	DP4	3.4403	3.7917
DP5	16.3291	7.642	DP5	3.6309	7.642	DP5	6.2781	7.642
DP6	6.899	79.4889	DP6	4.2139	79.4889	DP6	131.8949	79.4889
DP7	4.0507	7.1833	DP7	4.8379	7.1833	DP7	8.1956	7.1833
DP8	3.7985	5.6689	DP8	4.5912	5.6689	DP8	5.8007	5.6689
DP9	4.4844	4.4079	DP9	2.591	4.4079	DP9	4.5681	4.4079
DP10	5.0614	4.2807	DP10	4.3399	4.2807	DP10	4.2509	4.2807
DP11	5.6654	4.0776	DP11	5.1583	4.0776	DP11	4.229	4.0776
DP12	5.3667	3.8057	DP12	4.4039	3.8057	DP12	3.7985	3.8057
DP13	7.522	3.0598	DP13	2.6749	3.0598	DP13	2.9814	3.0598
DP14	5.1576	3.6437	DP14	5.3364	3.6437	DP14	3.2298	3.6437

ML	6.8797	6.6467	ML	5.7072	6.6467	ML	6.2303	6.6467
ML1	5.7687	6.464	ML1	6.4937	6.464	ML1	6.2044	6.464
ML2	5.816	6.2789	ML2	6.5736	6.2789	ML2	6.2495	6.2789
ML3	5.5477	6.3841	ML3	5.9652	6.3841	ML3	6.3882	6.3841
ML4	5.0978	5.8998	ML4	6.1838	5.8998	ML4	6.0134	5.8998
ML5	4.9156	5.6289	ML5	6.6248	5.6289	ML5	5.7313	5.6289
ML6	4.5436	5.5967	ML6	6.3156	5.5967	ML6	5.691	5.5967
ML7	5.4224	6.0048	ML7	7.4965	6.0048	ML7	6.2076	6.0048
ML8	6.1404	6.6492	ML8	9.7801	6.6492	ML8	9.145	6.6492

ID128 Radius of Curvature Comparison								
Name	LongCT	LS (LongCT)	Name	TransCT	LS(TransCT)	Name	uCT	LS (uCT)
DP	2.9546	2.3097	DP	2.5849	2.3097	DP	2.26	2.3097
DP1	4.3611	2.4334	DP1	2.8118	2.4334	DP1	2.3799	2.4334
DP2	3.0375	2.5323	DP2	3.1103	2.5323	DP2	2.4697	2.5323
DP3	3.1768	2.3054	DP3	1.949	2.3054	DP3	2.2078	2.3054
DP4	3.0517	3.375	DP4	5.7392	3.375	DP4	3.5608	3.375
DP5	8.6611	11.1581	DP5	1.3841	11.1581	DP5	21.4232	11.1581
DP6	2.8273	6.4833	DP6	1.7956	6.4833	DP6	6.9636	6.4833
DP7	9.312	4.0737	DP7	2.574	4.0737	DP7	4.1404	4.0737
DP8	2.8814	3.5565	DP8	2.8873	3.5565	DP8	3.5754	3.5565
DP9	2.3724	3.0734	DP9	10.6677	3.0734	DP9	3.1691	3.0734
DP10	2.1024	2.9984	DP10	40.7112	2.9984	DP10	2.835	2.9984
DP11	2.6941	2.9189	DP11	201.9788	2.9189	DP11	3.0105	2.9189
DP12	2.746	2.7906	DP12	16.376	2.7906	DP12	2.5707	2.7906
DP13	3.6842	2.71	DP13	32.8339	2.71	DP13	2.5127	2.71
DP14	2.4138	2.2414	DP14	2.0893	2.2414	DP14	1.9898	2.2414
DP15	1.6155	1.9938	DP15	1.7023	1.9938	DP15	1.9519	1.9938
ML	5.433	5.6895	ML	8.5291	5.6895	ML	5.776	5.6895
ML1	6.2975	5.9335	ML1	7.9515	5.9335	ML1	6.0402	5.9335
ML2	6.0101	5.6813	ML2	6.9016	5.6813	ML2	5.7193	5.6813
ML3	6.2987	5.7863	ML3	6.1135	5.7863	ML3	5.8381	5.7863
ML4	6.9806	5.9624	ML4	5.0465	5.9624	ML4	6.0788	5.9624
ML5	6.3154	6.0766	ML5	5.6742	6.0766	ML5	6.1572	6.0766
ML6	6.406	5.8418	ML6	5.9024	5.8418	ML6	5.9245	5.8418

ID129 Radius of Curvature Comparison								
Name	LongCT	LS (LongCT)	Name	TransCT	LS(TransCT)	Name	uCT	LS (uCT)
DP	2.724	2.462	DP	2.6875	2.462	DP	2.3821	2.462
DP1	2.803	2.5672	DP1	2.8381	2.5672	DP1	2.5284	2.5672

DP2	3.3569	2.9249	DP2	3.1121	2.9249	DP2	2.9695	2.9249
DP3	3.8308	3.4526	DP3	3.673	3.4526	DP3	3.4772	3.4526
DP4	4.18	4.5054	DP4	4.2681	4.5054	DP4	4.5569	4.5054
DP5	4.0425	11.4585	DP5	9.491	11.4585	DP5	12.4547	11.4585
DP6	1.4536	5.3509	DP6	22.1637	5.3509	DP6	6.8641	5.3509
DP7	3.2573	4.2953	DP7	43.929	4.2953	DP7	4.6032	4.2953
DP8	4.4306	3.7599	DP8	74.7827	3.7599	DP8	3.9409	3.7599
DP9	3.0269	3.6632	DP9	4.9123	3.6632	DP9	3.6045	3.6632
DP10	3.1256	3.4687	DP10	5.0683	3.4687	DP10	3.5681	3.4687
DP11	4.2256	3.239	DP11	4.721	3.239	DP11	3.3303	3.239
DP12	3.7884	3.0729	DP12	4.9877	3.0729	DP12	3.0017	3.0729
DP13	3.3976	2.7796	DP13	2.5594	2.7796	DP13	2.731	2.7796
DP14	4.532	2.6551	DP14	2.6158	2.6551	DP14	2.4854	2.6551
DP15	47.5446	2.8739	DP15	3.0651	2.8739	DP15	2.6509	2.8739
DP16	2.6028	3.3474	DP16	9.7205	3.3474	DP16	3.331	3.3474
ML	1.7782	3.1065	ML	3.1664	3.1065	ML	3.0846	3.1065
ML1	5.5469	4.8666	ML1	4.5953	4.8666	ML1	4.9125	4.8666
ML2	6.2089	4.3824	ML2	3.5122	4.3824	ML2	4.29	4.3824
ML3	7.0614	5.205	ML3	5.8535	5.205	ML3	5.3	5.205
ML4	6.9911	5.4804	ML4	5.0665	5.4804	ML4	5.5786	5.4804
ML5	6.7508	5.5395	ML5	5.2449	5.5395	ML5	5.5927	5.5395
ML6	7.291	5.8929	ML6	5.7915	5.8929	ML6	6.1234	5.8929
ML7	6.9896	6.216	ML7	5.5053	6.216	ML7	6.6143	6.216
ML8	5.9855	6.516	ML8	5.7419	6.516	ML8	6.7531	6.516
ML9	7.7294	6.7339	ML9	5.9933	6.7339	ML9	7.0101	6.7339
ML10	9.3253	9.9439	ML10	5.8469	9.9439	ML10	11.2544	9.9439
ML11	33.2453	9.5622	ML11	10.4015	9.5622	ML11	22.9177	9.5622

ID140 Radius of Curvature Comparison								
Name	LongCT	LS (LongCT)	Name	TransCT	LS(TransCT)	Name	uCT	LS (uCT)
DP	2.2643	2.0537	DP	2.3581	2.0537	DP	1.9711	2.0537
DP1	2.4254	2.3473	DP1	2.4785	2.3473	DP1	2.3085	2.3473
DP2	2.8013	2.6023	DP2	2.5114	2.6023	DP2	2.3434	2.6023
DP3	3.3518	2.5757	DP3	2.4197	2.5757	DP3	2.3681	2.5757
DP4	3.6341	3.0755	DP4	3.2176	3.0755	DP4	2.9596	3.0755
DP5	13.5751	23.6722	DP5	63.6522	23.6722	DP5	12.872	23.6722
DP6	3.0895	2.6101	DP6	1.5613	2.6101	DP6	2.2236	2.6101
DP7	2.7524	2.3163	DP7	2.2948	2.3163	DP7	1.9533	2.3163
DP8	4.4749	3.2506	DP8	2.1479	3.2506	DP8	2.6051	3.2506
DP9	4.2258	5.0174	DP9	12.3219	5.0174	DP9	5.6894	5.0174
DP10	3.4781	4.7942	DP10	5.1212	4.7942	DP10	4.462	4.7942

DP11	3.2175	4.2081	DP11	4.7023	4.2081	DP11	4.0791	4.2081
DP12	3.3735	3.9847	DP12	3.0202	3.9847	DP12	4.0374	3.9847
DP13	3.4139	3.6838	DP13	3.0424	3.6838	DP13	3.6159	3.6838
DP14	3.3054	3.722	DP14	3.7485	3.722	DP14	3.3589	3.722
ML	14.0173	2.1748	ML	3.1573	2.1748	ML	2.0238	2.1748
ML1	5.8636	6.7905	ML1	8.1139	6.7905	ML1	6.4335	6.7905
ML2	6.6363	6.4271	ML2	7.0734	6.4271	ML2	6.4037	6.4271
ML3	6.0359	6.274	ML3	6.7344	6.274	ML3	6.3615	6.274
ML4	6.0444	6.3645	ML4	6.4033	6.3645	ML4	6.4586	6.3645
ML5	6.0063	6.3256	ML5	6.3917	6.3256	ML5	6.4639	6.3256
ML6	5.8751	6.139	ML6	5.8989	6.139	ML6	6.1191	6.139
ML7	5.4856	5.7967	ML7	5.1697	5.7967	ML7	5.7767	5.7967
ML8	5.1615	6.876	ML8	5.462	6.876	ML8	7.1973	6.876

ID142 Radius of Curvature Comparison								
Name	LongCT	LS (LongCT)	Name	TransCT	LS(TransCT)	Name	uCT	LS (uCT)
DP	2.0735	1.9256	DP	2.0976	1.9256	DP	1.8003	1.9256
DP1	2.2331	2.1253	DP1	2.3425	2.1253	DP1	1.9795	2.1253
DP2	2.37	2.6159	DP2	1.9152	2.6159	DP2	2.3775	2.6159
DP3	2.702	2.7494	DP3	2.202	2.7494	DP3	2.5729	2.7494
DP4	3.2465	2.1176	DP4	1.1138	2.1176	DP4	2.0496	2.1176
DP5	2.5779	6.5701	DP5	4.4841	6.5701	DP5	6.9977	6.5701
DP6	309.9374	4.7563	DP6	68.9406	4.7563	DP6	4.7798	4.7563
DP7	4.5736	3.5895	DP7	6.1034	3.5895	DP7	3.6767	3.5895
DP8	3.5097	3.1663	DP8	2.9757	3.1663	DP8	3.1097	3.1663
DP9	2.2301	2.9261	DP9	2.8865	2.9261	DP9	2.9164	2.9261
DP10	2.7009	2.7904	DP10	2.6267	2.7904	DP10	2.7652	2.7904
DP11	2.0679	2.5985	DP11	2.9947	2.5985	DP11	2.6485	2.5985
DP12	2.4502	2.435	DP12	3.2948	2.435	DP12	2.4999	2.435
DP13	2.3291	2.0705	DP13	1.1109	2.0705	DP13	2.4114	2.0705
DP14	3.5971	2.2343	DP14	88.2103	2.2343	DP14	2.716	2.2343
DP15	2.6323	21.4935	DP15	0.4694	21.4935	DP15	8.4094	21.4935
ML	4.5977	6.097	ML	4.8214	6.097	ML	6.1838	6.097
ML1	4.953	5.6523	ML1	3.9299	5.6523	ML1	5.6165	5.6523
ML2	5.025	5.6028	ML2	5.0148	5.6028	ML2	5.5426	5.6028
ML3	7.0676	5.72	ML3	4.9857	5.72	ML3	5.8436	5.72
ML4	8.6429	5.8593	ML4	6.8833	5.8593	ML4	5.982	5.8593
ML5	8.4481	6.1243	ML5	7.314	6.1243	ML5	6.0293	6.1243
ML6	6.283	10.9477	ML6	5.394	10.9477	ML6	11.9221	10.9477
ML7	5.4841	6.895	ML7	5.7041	6.895	ML7	6.3668	6.895

Appendix C – Resolution Study Results

0.024 Resolution, Lossless Compression		
Threshold	Mean RMSE (mm)	Stdev
2850	Not able to fit radius	
3000	0.072443073	0.038842576
3150	0.080082516	0.039150407
3300	0.088287468	0.038373576
3450	0.098325236	0.044039683
3600	0.107602665	0.054917835
3750	0.114383522	0.061709209
3900	0.122089228	0.069784717
4050	0.127703715	0.077565559
4200	0.125691232	0.073837852
4350	0.133518516	0.083014599

0.048 Resolution, Lossless Compression		
Threshold	Mean RMSE (cm)	Stdev
2850	0.008701104	0.003602
3000	0.007027022	0.000497
3150	0.009738646	0.003393
3300	0.010365802	0.004027
3450	0.011149956	0.004988
3600	0.011725515	0.005506
3750	0.012541223	0.006339
3900	0.013196342	0.006967
4050	0.013974805	0.007704
4200	0.014372683	0.007982
4350	0.014780806	0.008215

0.096 Resolution, Lossless Compression		
Threshold	Mean RMSE (cm)	Stdev
2850	0.011134952	0.003332
3000	0.0112538	0.003307
3150	0.011691986	0.003722
3300	0.012381809	0.004263
3450	0.01345372	0.005138
3600	0.014473566	0.005957
3750	0.015137197	0.006377
3900	0.015902704	0.006793
4050	0.017355757	0.007847

4200	0.017994774	0.008141
4350	0.01518155	0.007402

0.192 Resolution, Lossless Compression		
Threshold	Mean RMSE	Stdev
2850	0.011168276	0.004016489
3000	0.011075766	0.004284238
3150	0.010693264	0.004519567
3300	0.010966655	0.004703884
3450	0.011832167	0.005527658
3600	0.012756731	0.006265002
3750	0.013472602	0.006496293
3900	0.014309281	0.006776147
4050	0.015137667	0.007273225
4200	0.016332751	0.007849142
4350	0.016802763	0.007140336

0.384 Resolution, Lossless Compression		
Threshold	Mean RMSE (cm)	Stdev
2850	0.014942993	0.004504
3000	0.048809227	0.007902
3150	0.159073385	0.150417
3300	0.159232257	0.1503
3450	0.159969982	0.149903
3600	0.240792908	0.133531
3750	0.242056757	0.132913
3900	0.03289347	0.019937
4050	0.034000157	0.019704
4200	0.035728158	0.019653
4350	0.037229282	0.019638

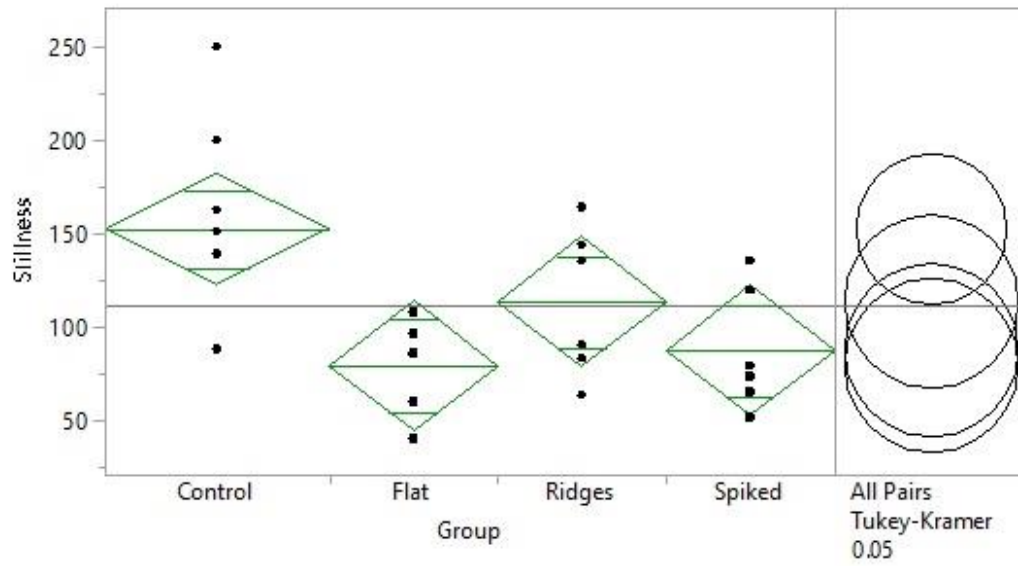
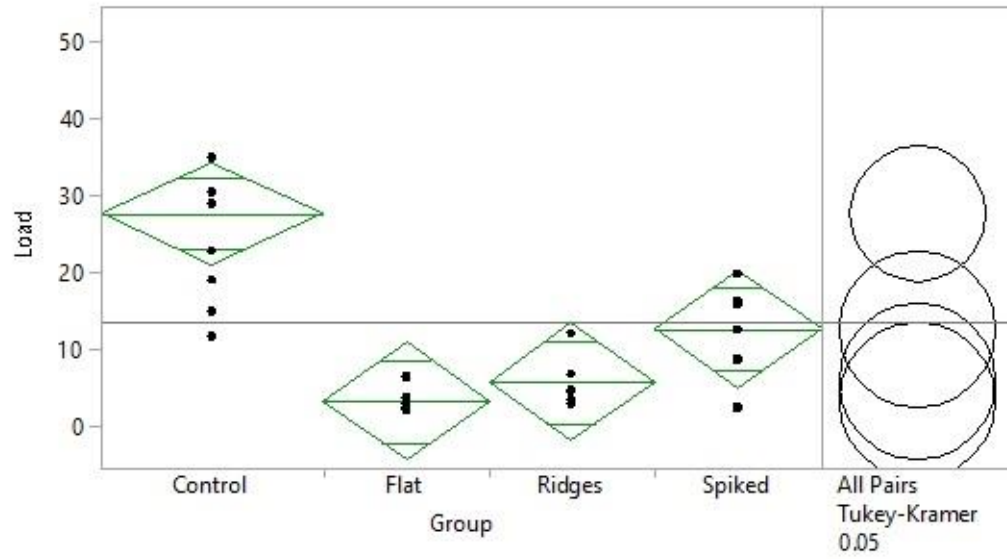
ID	DICOM Image Compression	Resolution (x10⁻³ mm)	ROI (mm)	Pos_Avg	Neg_Avg	Max	Min	RMSE
103	Lossless	24	5	0.040502	-0.03776	0.39051	-0.90263	0.052126
107	Lossless	24	5	0.021503	-0.01579	0.5917	-0.53954	0.025608
108	Lossless	24	5	0.031085	-0.05335	0.544176	-0.54854	0.06249
111	Lossless	24	5	0.031601	-0.02992	0.626309	-0.6223	0.041039
118	Lossless	24	5	0.038659	-0.03312	1.437608	-1.45991	0.068814
119	Lossless	24	5	0.028476	-0.02122	0.605844	-0.94905	0.03564
120	Lossless	24	5	0.03237	-0.02225	0.829322	-0.96364	0.037557

123	Lossless	24	5	0.06741	-0.03247	0.402316	-0.53325	0.074631
126	Lossless	24	5	0.068641	-0.04392	0.334362	-0.83105	0.076008
127	Lossless	24	5	0.020718	-0.02303	0.432827	-0.66875	0.028672
128	Lossless	24	5	0.035311	-0.02395	0.649473	-0.65463	0.041782
129	Lossless	24	5	0.0341	-0.01978	0.766533	-0.48349	0.045392
134	Lossless	24	5	0.025943	-0.03021	0.442001	-0.71112	0.036727
139	Lossless	24	5	0.027802	-0.04172	0.330871	-0.58305	0.048135
140	Lossless	24	5	0.035673	-0.03595	0.270479	-0.45458	0.045618
103	Lossless	48	5	0.041737	-0.04992	1.686144	-1.69538	0.074349
107	Lossless	48	5	0.022072	-0.01945	1.099208	-1.49115	0.036076
108	Lossless	48	5	0.029983	-0.06257	1.236655	-1.2149	0.075334
111	Lossless	48	5	0.033254	-0.04044	1.326633	-1.43293	0.067587
118	Lossless	48	5	0.043812	-0.03685	1.463894	-1.46065	0.076076
119	Lossless	48	5	0.02925	-0.03079	1.379363	-1.81981	0.061752
120	Lossless	48	5	0.032846	-0.03115	1.15917	-1.67282	0.060525
123	Lossless	48	5	0.078229	-0.03947	1.522264	-1.61225	0.090593
126	Lossless	48	5	0.074137	-0.05359	1.083892	-1.59462	0.090347
127	Lossless	48	5	0.02123	-0.02814	1.879568	-1.63053	0.047947
128	Lossless	48	5	0.036679	-0.03171	1.323838	-1.60592	0.055682
129	Lossless	48	5	0.035518	-0.02625	1.073705	-1.4448	0.060625
134	Lossless	48	5	0.027417	-0.03832	1.129451	-1.61169	0.057234
139	Lossless	48	5	0.030211	-0.05075	0.970513	-1.16186	0.063737
140	Lossless	48	5	0.032343	-0.0498	1.444869	-1.48413	0.060889
103	Lossless	96	5	0.034662	-0.04786	1.865627	-1.89323	0.073807
107	Lossless	96	5	0.019699	-0.03045	1.557142	-1.6299	0.043425
108	Lossless	96	5	0.030448	-0.07419	1.397919	-1.25875	0.087687
111	Lossless	96	5	0.027693	-0.04673	1.173007	-1.41775	0.073374
118	Lossless	96	5	0.043952	-0.0435	1.527507	-1.54831	0.07706
119	Lossless	96	5	0.026244	-0.03599	1.400392	-1.86099	0.06772
120	Lossless	96	5	0.026415	-0.03519	1.314135	-1.85512	0.062758
123	Lossless	96	5	0.06574	-0.04339	1.095626	-1.64192	0.077631
126	Lossless	96	5	0.063839	-0.05861	1.396024	-1.68684	0.082776
127	Lossless	96	5	0.02025	-0.03799	2.049178	-2.01059	0.057857
128	Lossless	96	5	0.031096	-0.03628	1.434222	-1.62139	0.057158
129	Lossless	96	5	0.031102	-0.03296	1.51589	-1.52691	0.063348
134	Lossless	96	5	0.025872	-0.04611	1.011647	-1.61462	0.063621
139	Lossless	96	5	0.02939	-0.06062	1.043156	-1.32206	0.076838
140	Lossless	96	5	0.032343	-0.0498	1.444869	-1.48413	0.060889
103	Lossless	192	5	0.03292	-0.05374	1.719856	-1.88435	0.078829
107	Lossless	192	5	0.021521	-0.04967	2.308999	-2.00232	0.063223
108	Lossless	192	5	0.03672	-0.08853	1.394243	-2.24674	0.103889

111	Lossless	192	5	0.029472	-0.06002	2.687622	-2.16014	0.087838
118	Lossless	192	5	0.046751	-0.06353	1.901145	-2.16848	0.103346
119	Lossless	192	5	0.031118	-0.05097	1.371249	-1.86091	0.085883
120	Lossless	192	5	0.026565	-0.0499	1.609117	-1.89174	0.07676
123	Lossless	192	5	0.060881	-0.05604	1.702881	-1.93103	0.085225
126	Lossless	192	5	0.060951	-0.06833	2.806329	-2.10654	0.095445
127	Lossless	192	5	0.025023	-0.05466	2.703944	-2.65349	0.076187
128	Lossless	192	5	0.03496	-0.05228	1.971201	-2.48408	0.078544
129	Lossless	192	5	0.033979	-0.04868	1.698946	-1.80102	0.076508
134	Lossless	192	5	0.032379	-0.06172	1.498342	-1.83273	0.082024
139	Lossless	192	5	0.032457	-0.07622	1.419766	-1.49184	0.098288
140	Lossless	192	5	0.031879	-0.05405	2.087775	-1.79112	0.070478
103	Lossless	384	5	0.047361	-0.08391	2.494158	-2.52577	0.108817
107	Lossless	384	5	0.039536	-0.08597	2.373049	-2.14291	0.101702
108	Lossless	384	5	0.054503	-0.12146	2.985813	-2.39821	0.138593
111	Lossless	384	5	0.05092	-0.0966	1.652957	-2.4998	0.122923
118	Lossless	384	5	0.064242	-0.10264	2.729099	-2.45284	0.144478
119	Lossless	384	5	0.051649	-0.0861	2.644749	-2.32776	0.121685
120	Lossless	384	5	0.038018	-0.0891	2.038733	-2.02743	0.112933
123	Lossless	384	5	0.06893	-0.08762	2.582735	-2.53964	0.11812
126	Lossless	384	5	0.073995	-0.09393	3.100755	-3.02368	0.122498
127	Lossless	384	5	0.042886	-0.09314	2.361066	-2.87349	0.114094
128	Lossless	384	5	0.058698	-0.09301	2.023776	-3.75226	0.12165
129	Lossless	384	5	0.046895	-0.08615	2.423171	-2.29986	0.113928
134	Lossless	384	5	0.05567	-0.0985	2.73529	-2.2843	0.121658
139	Lossless	384	5	0.054124	-0.11474	1.874543	-2.0404	0.142315
140	Lossless	384	5	0.044568	-0.08141	2.896499	-3.46853	0.101422

Appendix D – Ligament Fixation Full Data

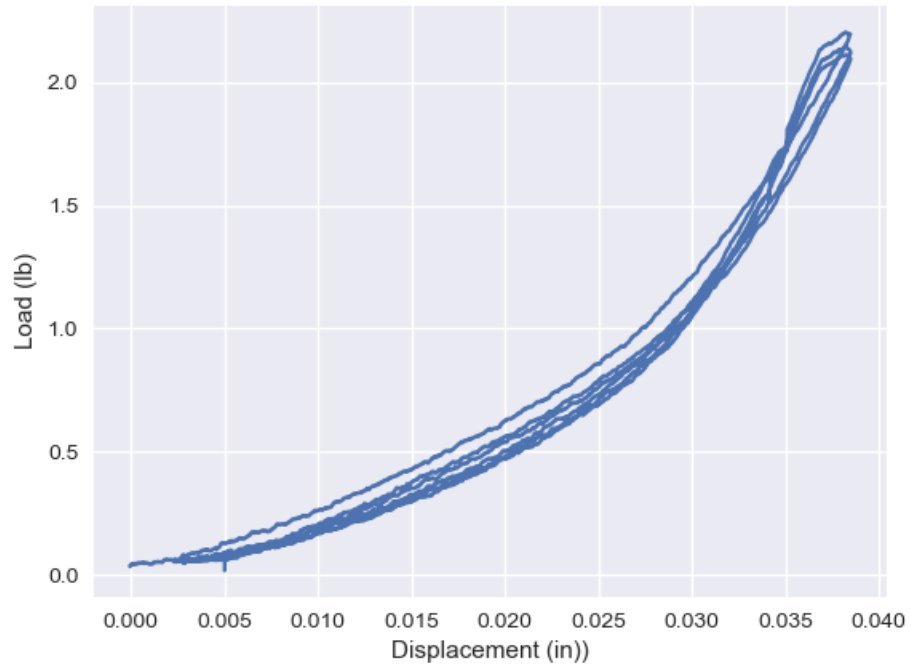
Specimen ID	Group	Test Order	Max Load (lbs)	Stiffness
20150622-04	Control	1	30.388	249.95
030616M	Control	2	28.831	138.81
03062014-6	Control	3	18.968	200.03
20150611-3	Control	4	22.761	87.583
20150622-02	Control	5	34.889	139.06
20150706-12R	Control	6	11.67	151.14
20150715-6R	Control	7	58.078	162.63
20150716-8R	Control	8	14.798	88.38
20160604-05	Flat	1	2.0401	96.386
20150622 - 03	Flat	2	2.316	108.01
20150618-03	Flat	3	2.766	59.87
20150710-5	Flat	4	2.374	39.875
20150715-4	Flat	Tore During Test Setup		
20150715-3L	Flat	6	6.376	85.119
20150623-3	Flat	7	3.623	86.063
20150716-9L	Ridges	1	6.743	90.401
20150623-4L	Ridges	2	3.484	63.538
20150623-7	Ridges	3	4.496	164.17
20150612-1	Ridges	4	2.831	135.39
/at003	Ridges	5	12.039	143.88
20150519-4	Ridges	6	4.718	83.1
20150623-8R	Ridges	Tore During Test Setup		
20150601-3	Spiked	Tore During Initial Cyclic Loading		
20140402	Spiked	2	15.844	135.39
20150716-7	Spiked	3	2.393	73.429
20150622-01R	Spiked	4	8.581	51.331
20150604-04	Spiked	5	16.194	119.7
20150716-6R	Spiked	6	19.762	79.358
20140306-8	Spiked	7	12.513	64.83



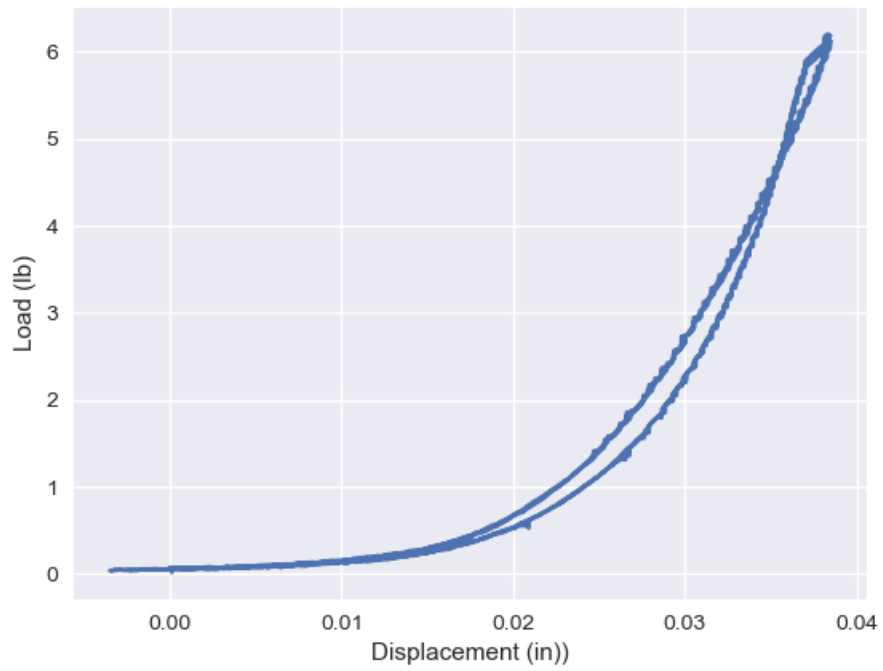
Appendix E – Polymer Bearing Surface Compressive Testing

Material	Thickness	Strain Rate	Avg Max
Polyurethane	1.5	100	2.153667
Polyurethane	1.5	100	4.491667
Polyurethane	1.5	100	11.897
Polyurethane	2.5	100	15.984
Polyurethane	2.5	100	16.42367
Polyurethane	3.5	100	24.34533
Polyurethane	3.5	100	21.11233
Polyurethane	3.5	100	24.54633
PVA-PVP	1.5	100	1.223333
PVA-PVP	1.5	100	1.918
PVA-PVP	1.5	100	4.417667
PVA-PVP	2.5	100	2.850333
PVA-PVP	2.5	100	6.499667
PVA-PVP	2.5	100	3.942333
PVA-PVP	3.5	100	5.649
PVA-PVP	3.5	100	5.231
PVA-PVP	3.5	100	4.612667
Polyurethane	1.5	1000	3.491333
Polyurethane	1.5	1000	7.255333
Polyurethane	1.5	1000	14.29733
Polyurethane	2.5	1000	17.40233
Polyurethane	2.5	1000	21.72567
Polyurethane	3.5	1000	27.25267
Polyurethane	3.5	1000	25.34067
Polyurethane	3.5	1000	24.74567
PVA-PVP	1.5	1000	1.764333
PVA-PVP	1.5	1000	2.055667
PVA-PVP	1.5	1000	3.829333
PVA-PVP	2.5	1000	3.812667
PVA-PVP	2.5	1000	7.413
PVA-PVP	2.5	1000	3.057333
PVA-PVP	3.5	1000	6.045333
PVA-PVP	3.5	1000	6.633667
PVA-PVP	3.5	1000	6.766667

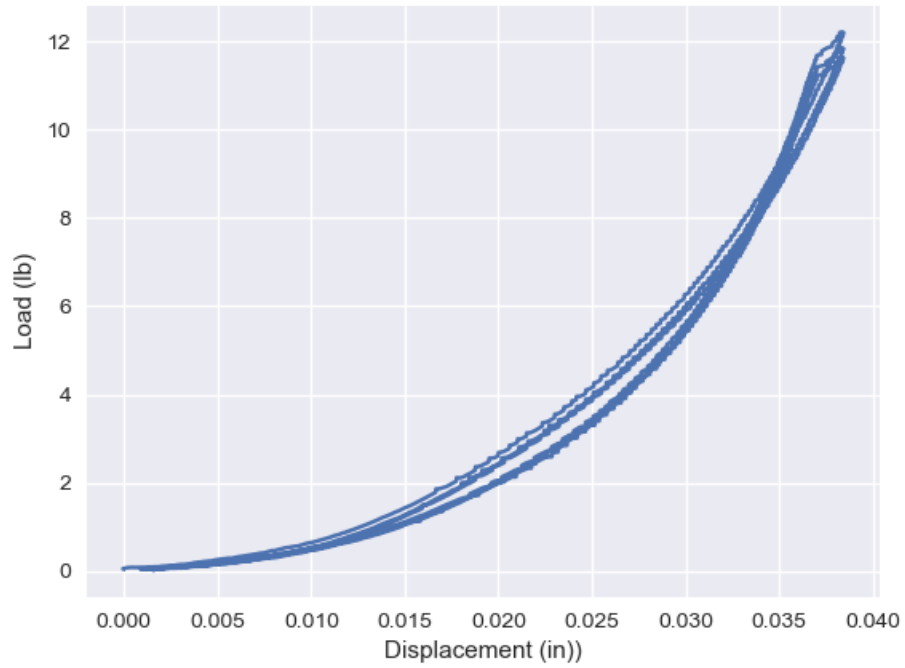
Polyurethane 1.5mm 100%/min - Sample:1



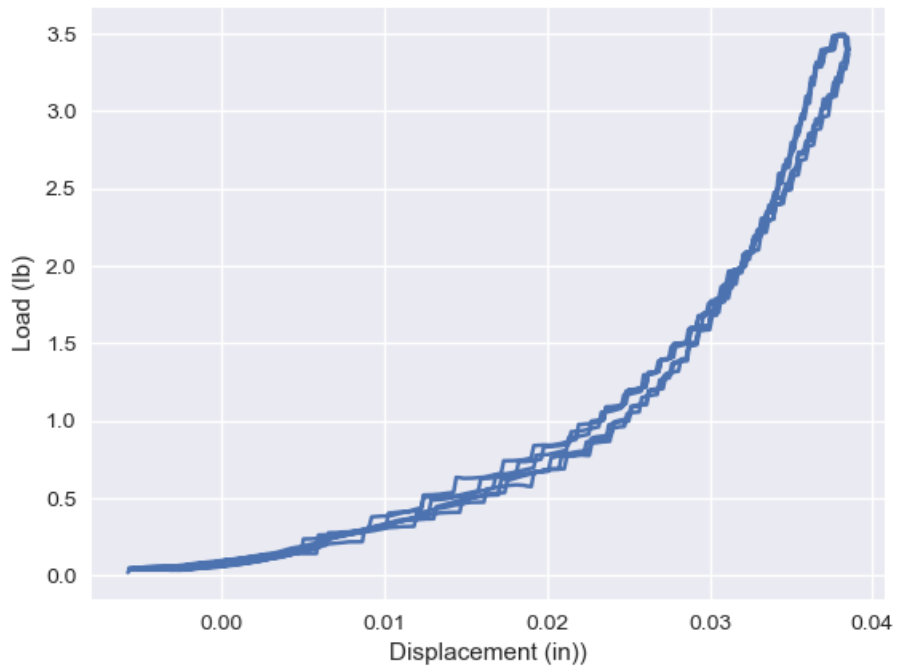
Polyurethane 1.5mm 100%/min - Sample:2



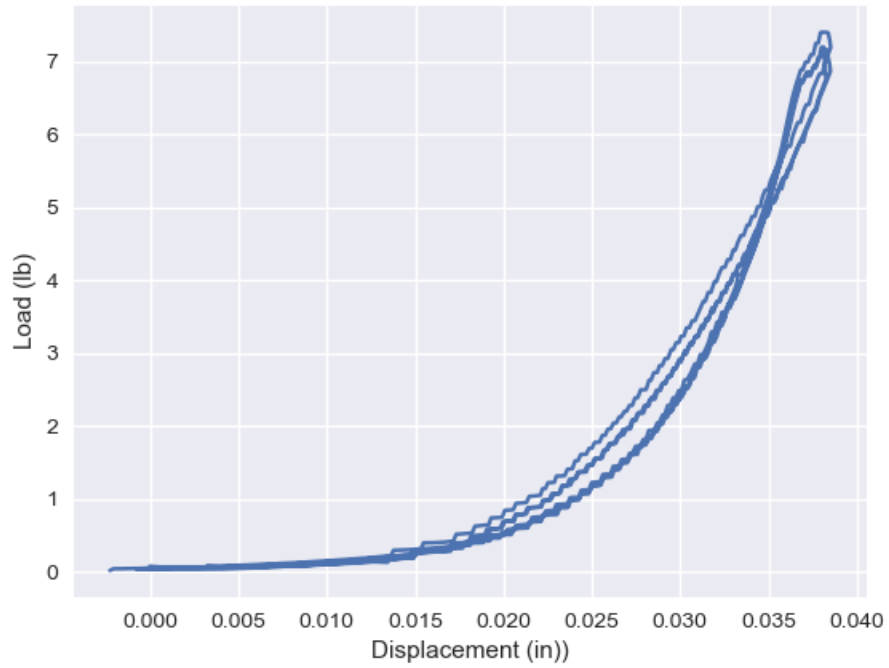
Polyurethane 1.5mm 100%/min - Sample:3



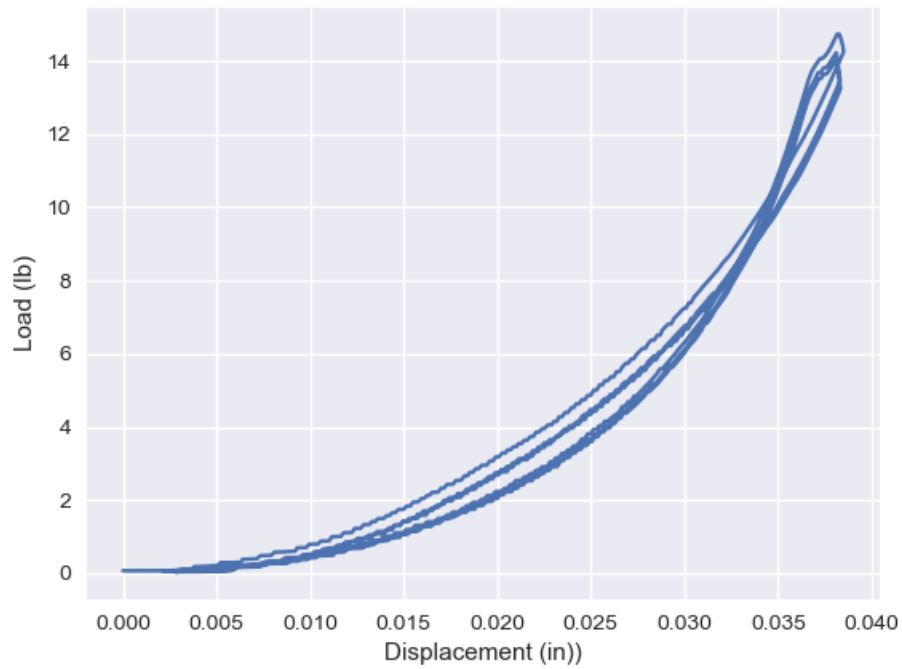
Polyurethane 1.5mm 1000%/min - Sample:1



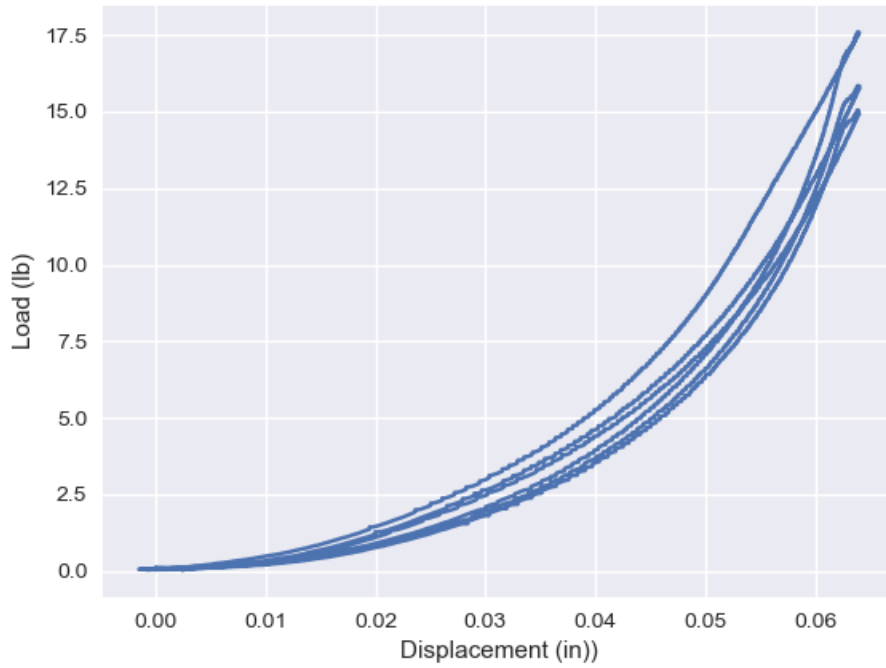
Polyurethane 1.5mm 1000%/min - Sample:2



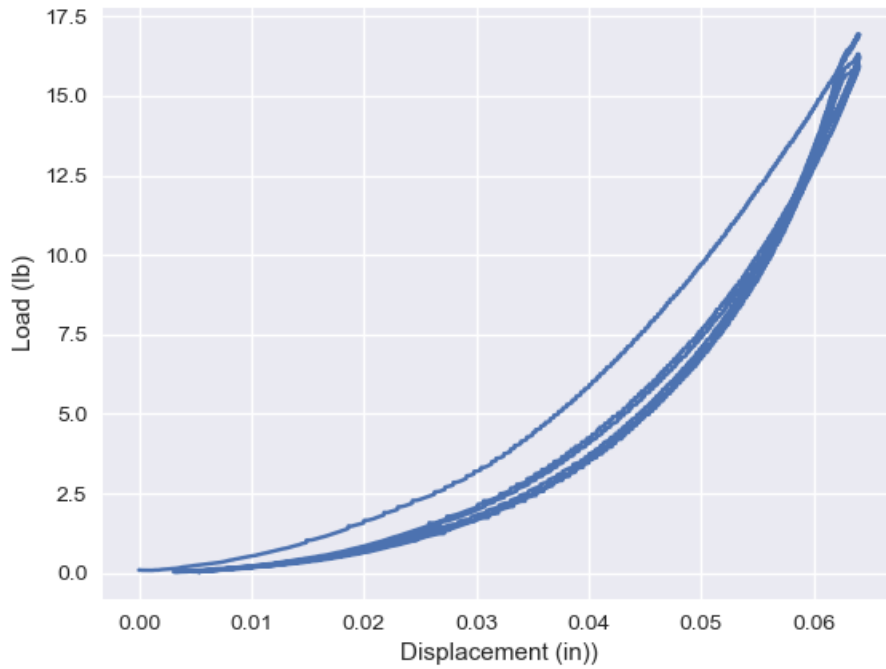
Polyurethane 1.5mm 1000%/min - Sample:3



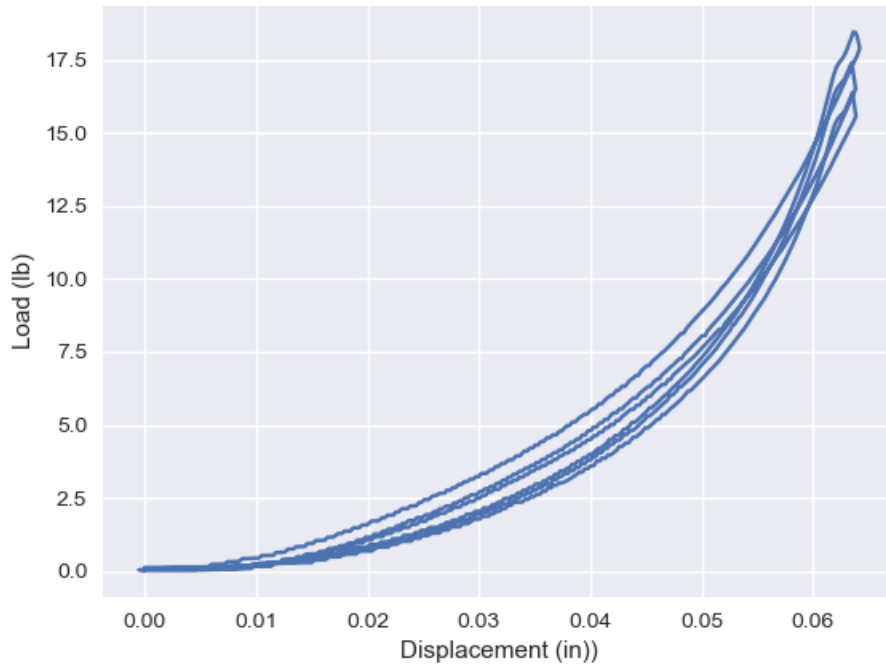
Polyurethane 2.5 mm 100%/min - Sample:1



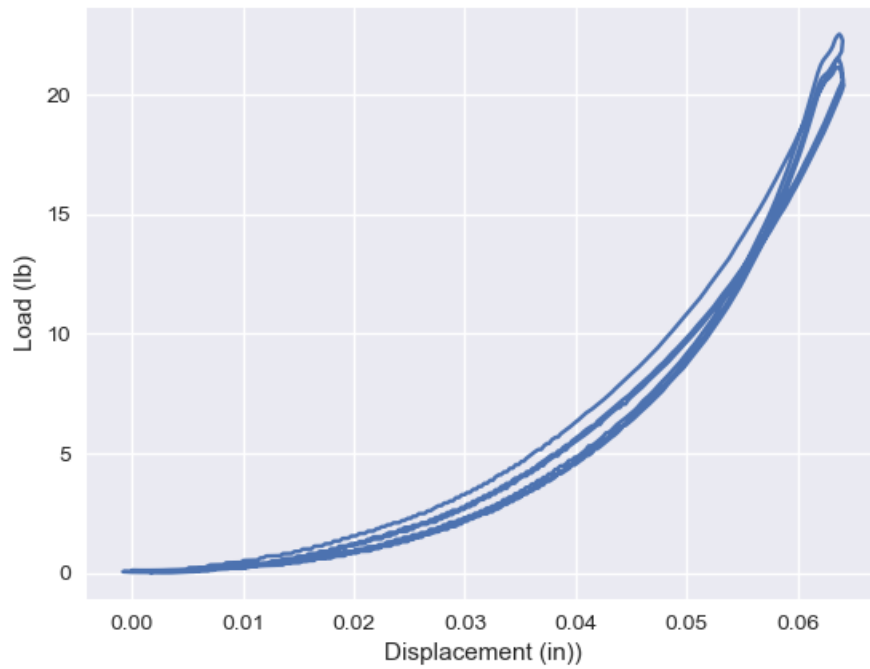
Polyurethane 2.5 mm 100%/min - Sample:2



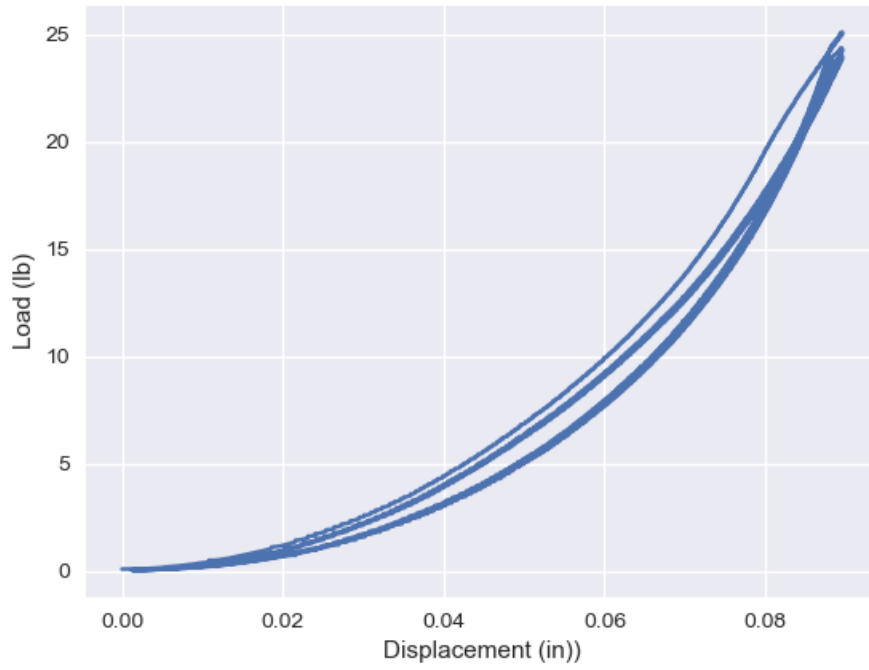
Polyurethane 2.5 mm 1000%/min - Sample:1



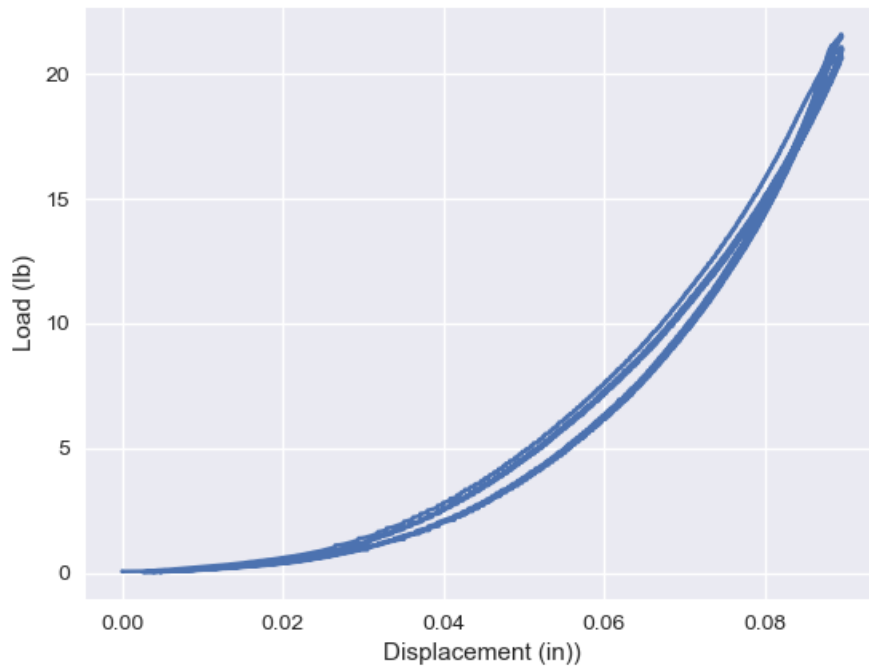
Polyurethane 2.5 mm 1000%/min - Sample:2



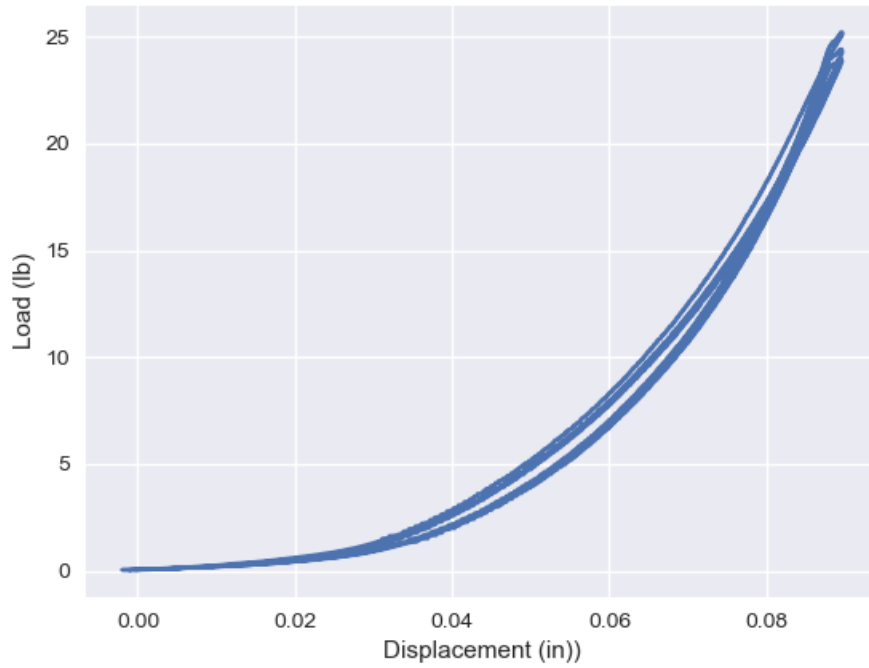
Polyurethane 3.5 mm 100%/min - Sample:1



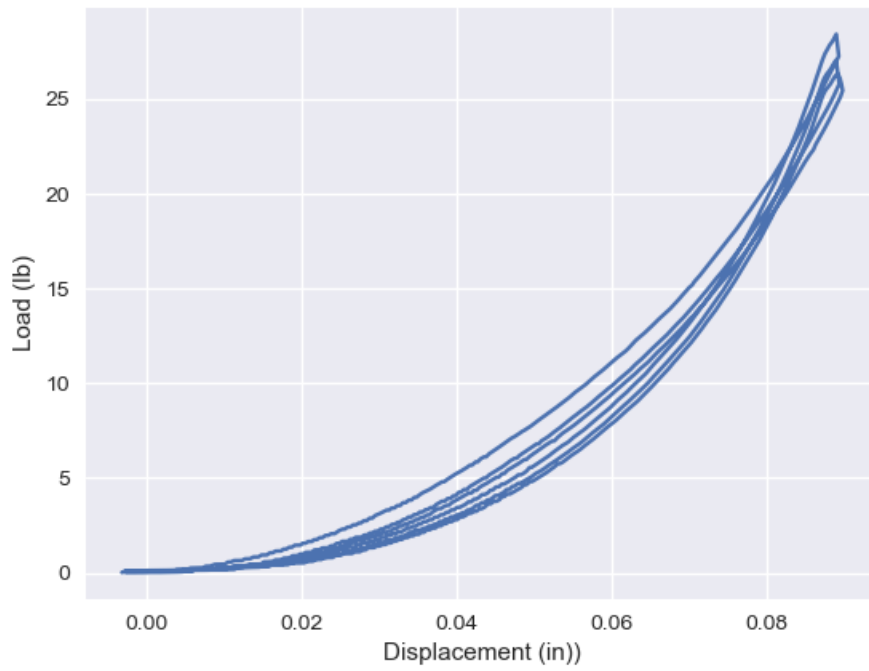
Polyurethane 3.5 mm 100%/min - Sample:2



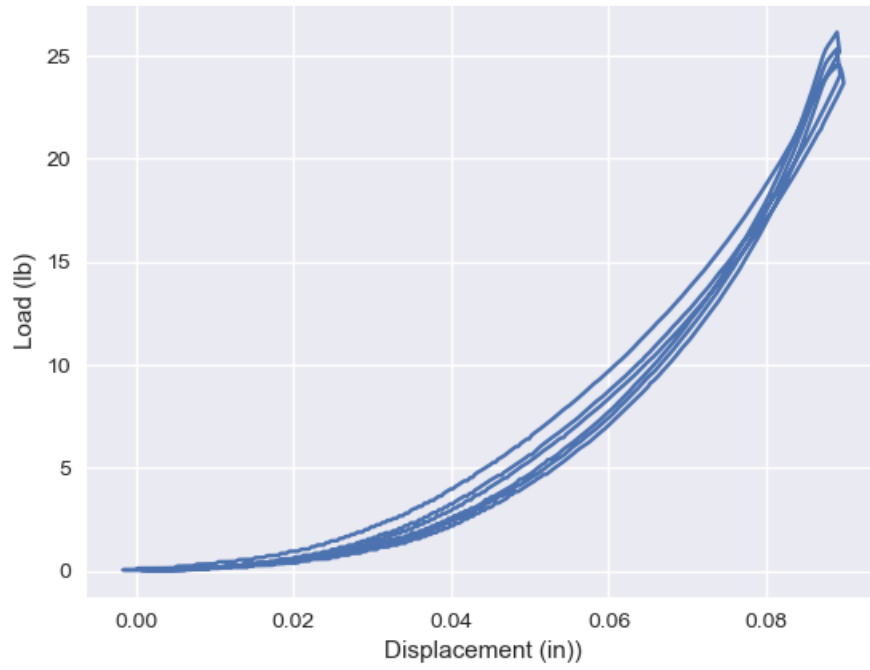
Polyurethane 3.5 mm 100%/min - Sample:3



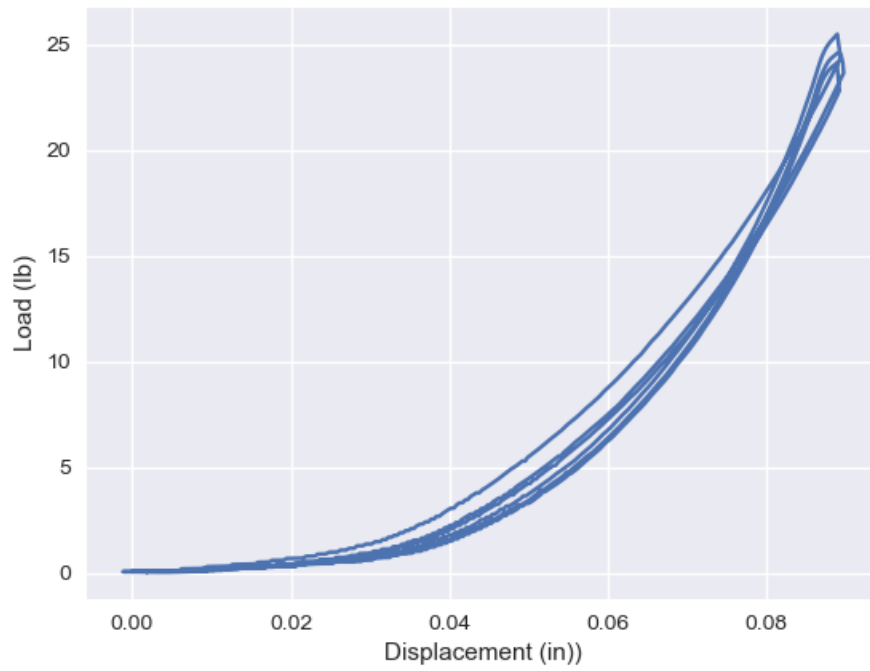
Polyurethane 3.5 mm 1000%/min - Sample:1



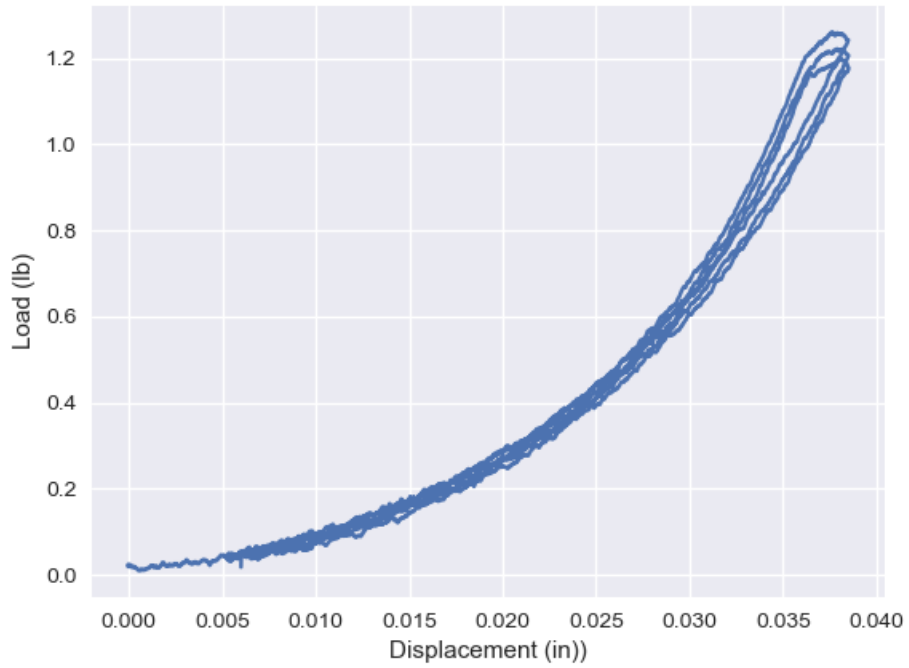
Polyurethane 3.5 mm 1000%/min - Sample:2



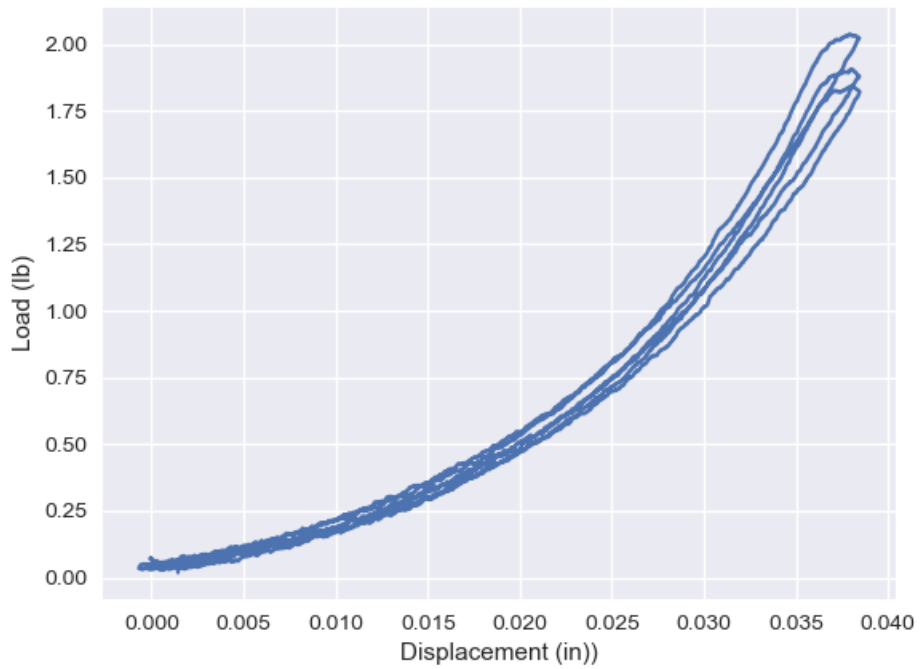
Polyurethane 3.5 mm 1000%/min - Sample:3



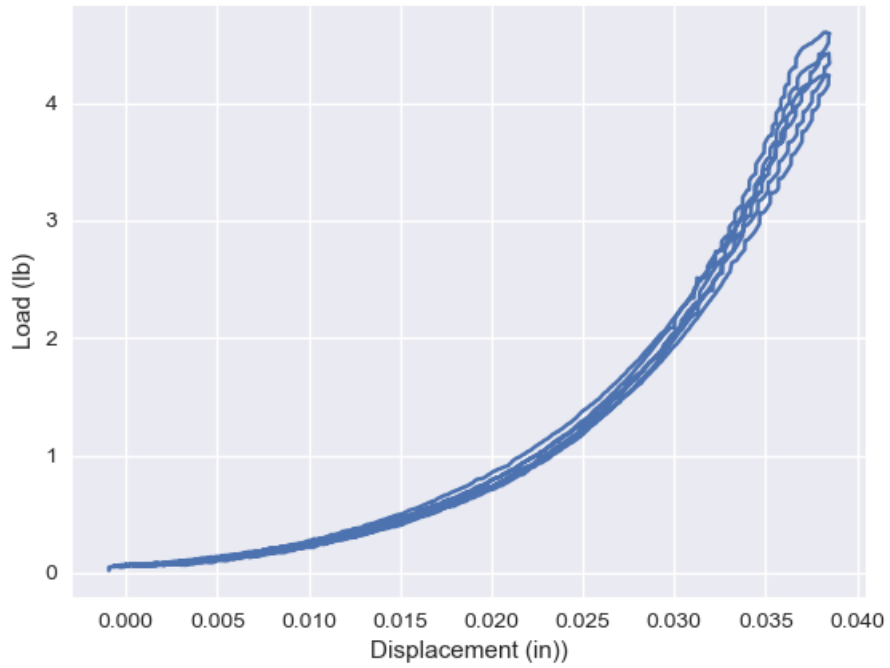
PVA - PVP 1.5mm 100%/min - Sample:1



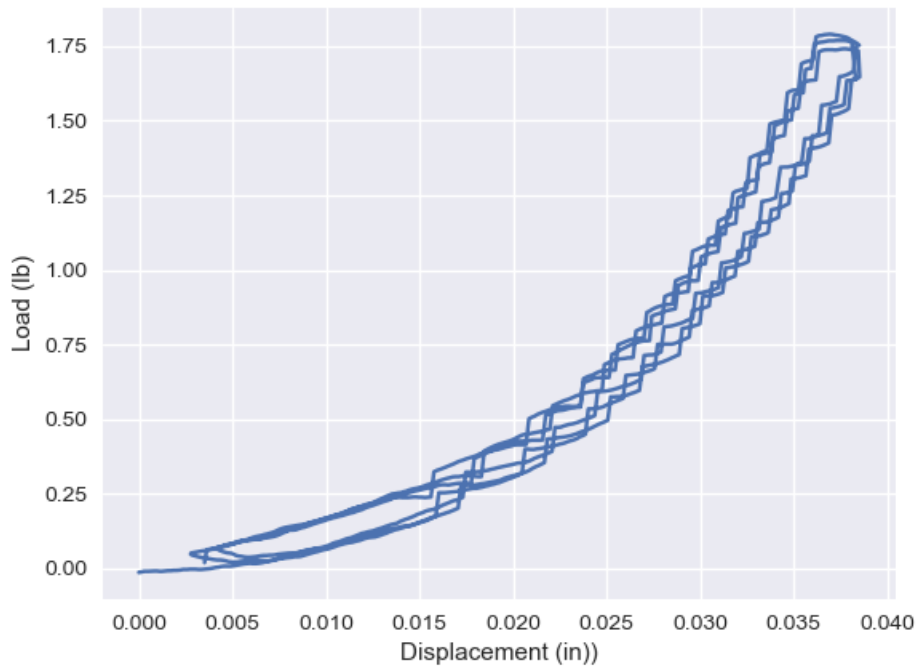
PVA - PVP 1.5mm 100%/min - Sample:2



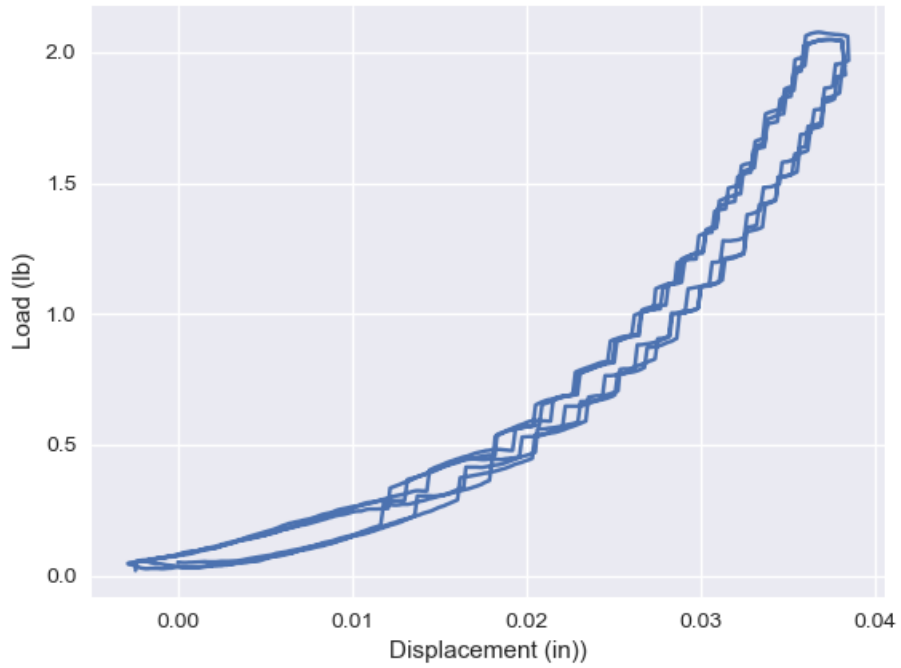
PVA - PVP 1.5mm 100%/min - Sample:3



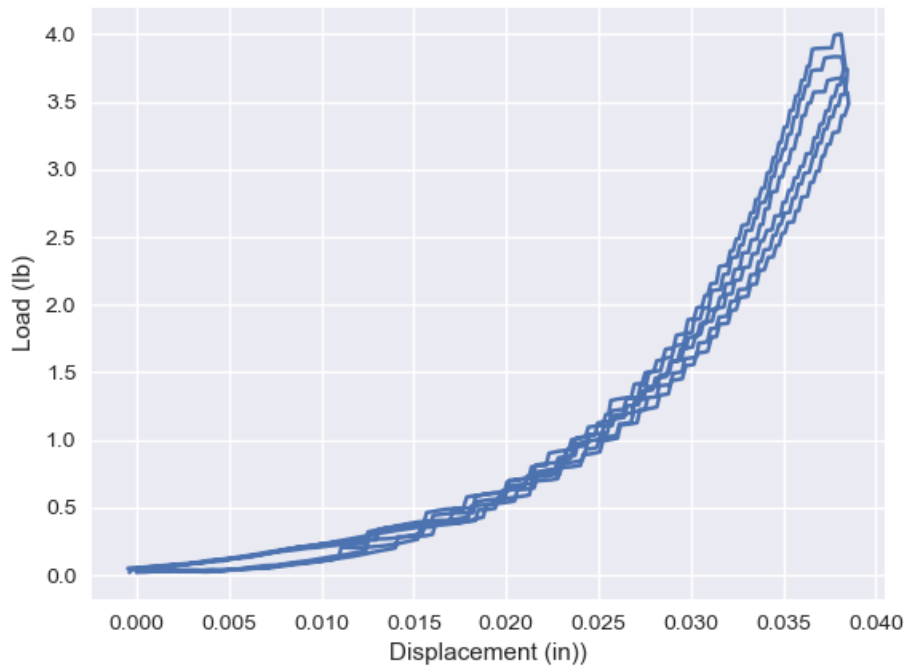
PVA - PVP 1.5mm 1000%/min - Sample:1



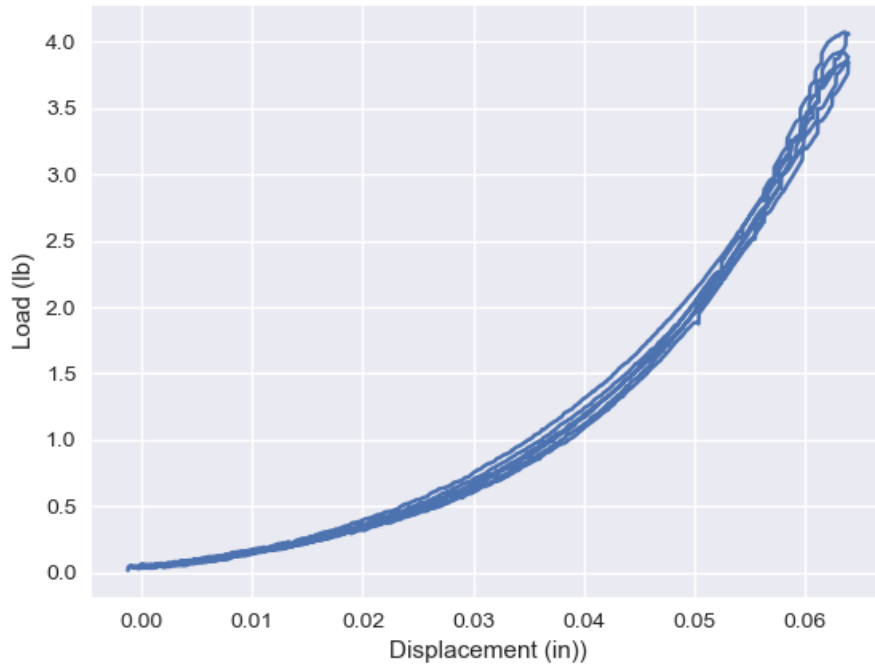
PVA - PVP 1.5mm 1000%/min - Sample:2



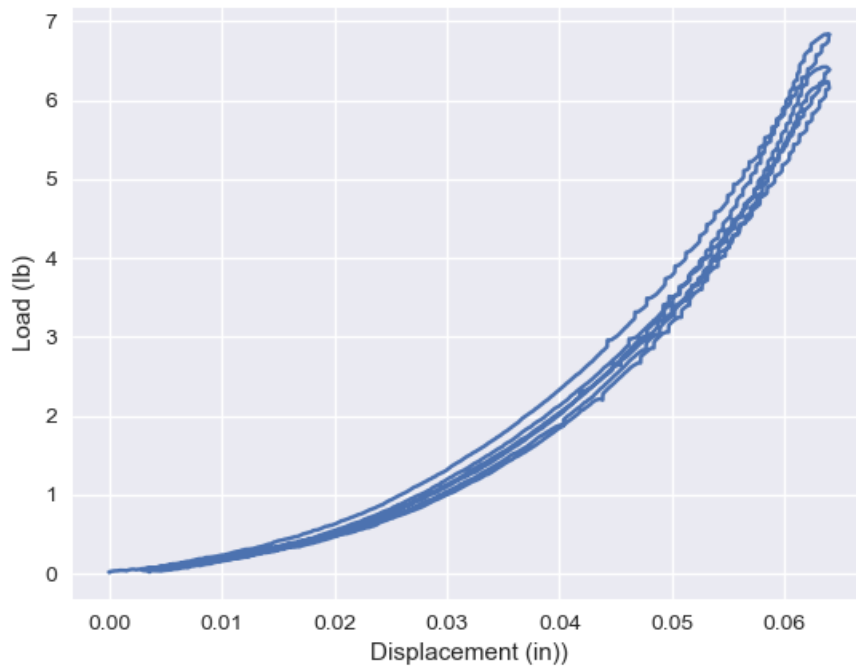
PVA - PVP 1.5mm 1000%/min - Sample:3



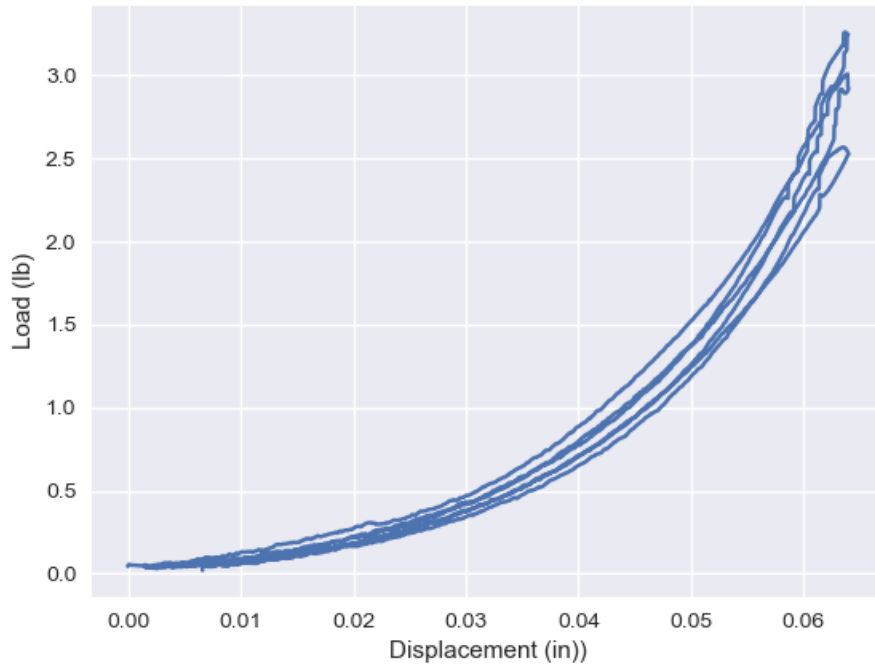
PVA - PVP 2.5 mm 100%/min - Sample:1



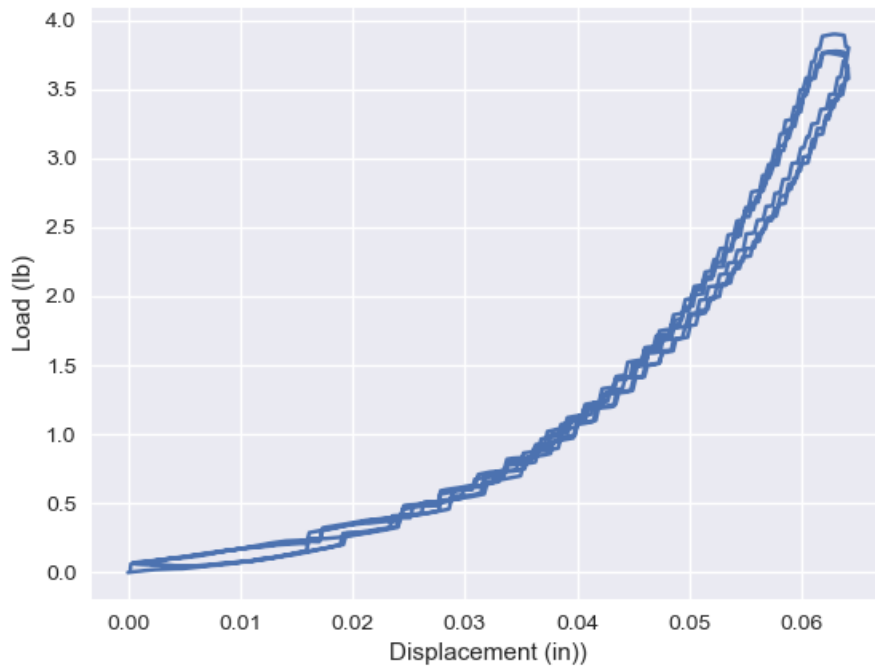
PVA - PVP 2.5 mm 100%/min - Sample:2

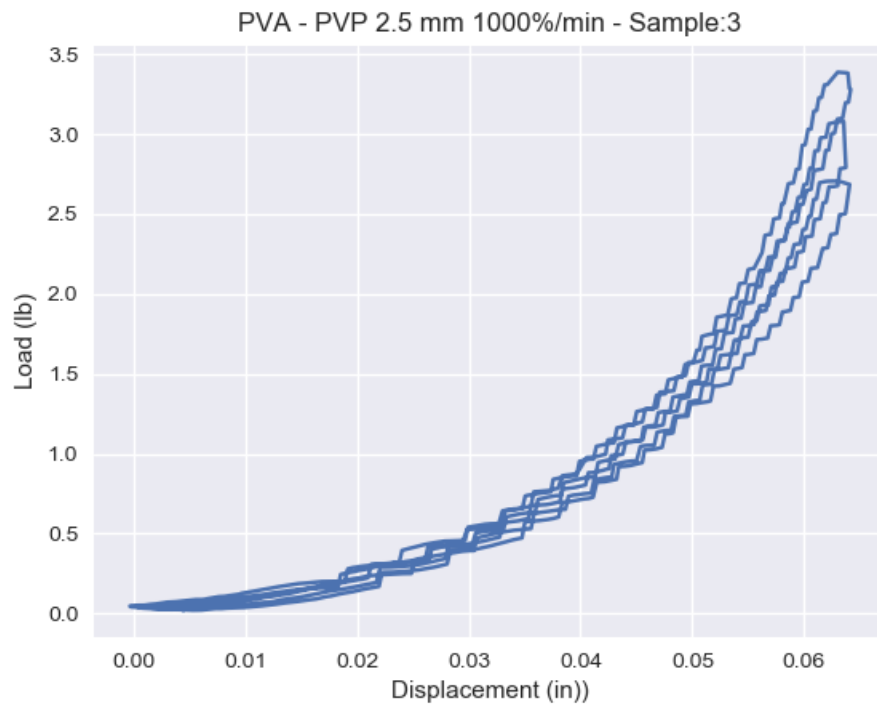
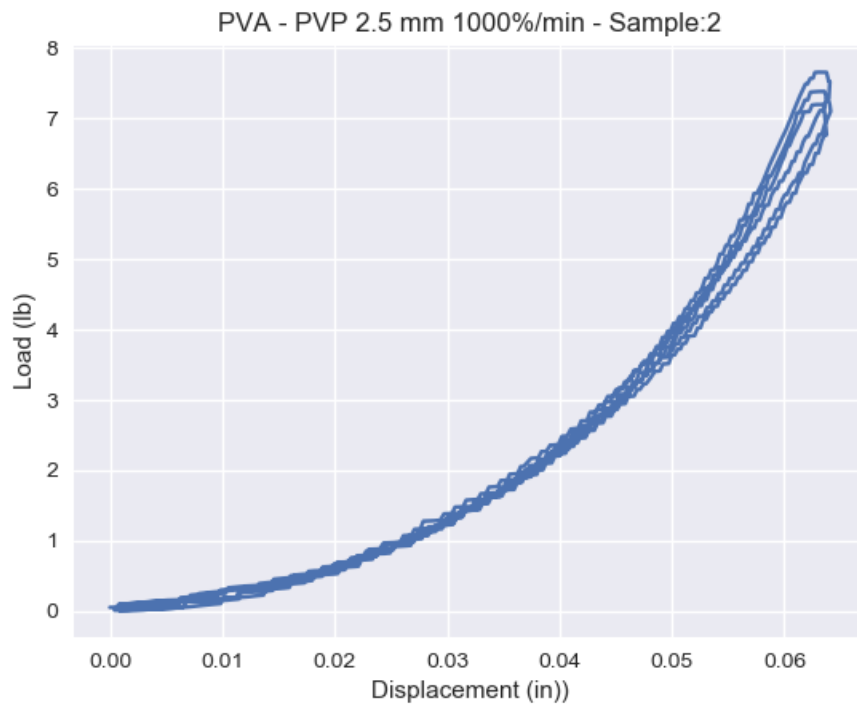


PVA - PVP 2.5 mm 100%/min - Sample:3

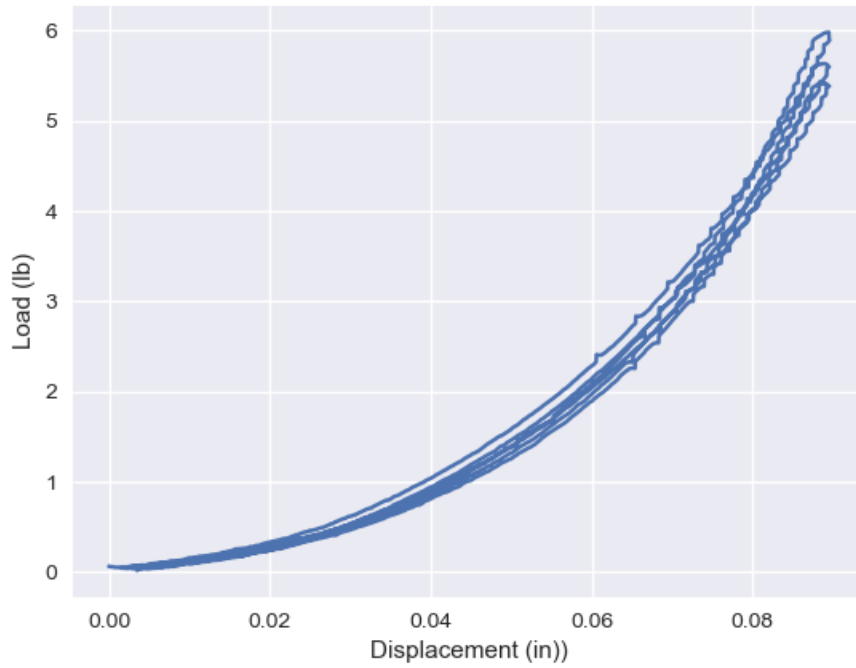


PVA - PVP 2.5 mm 1000%/min - Sample:1

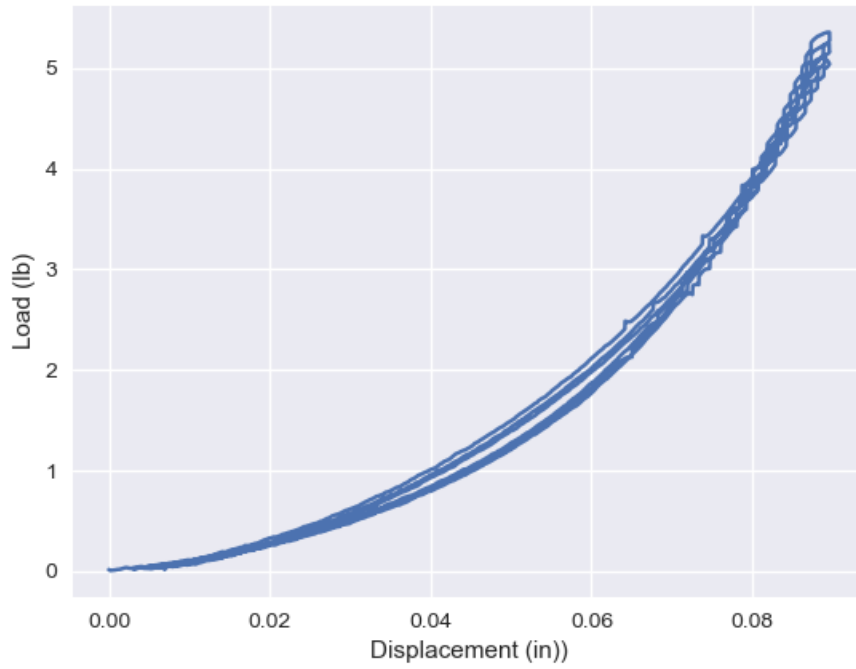




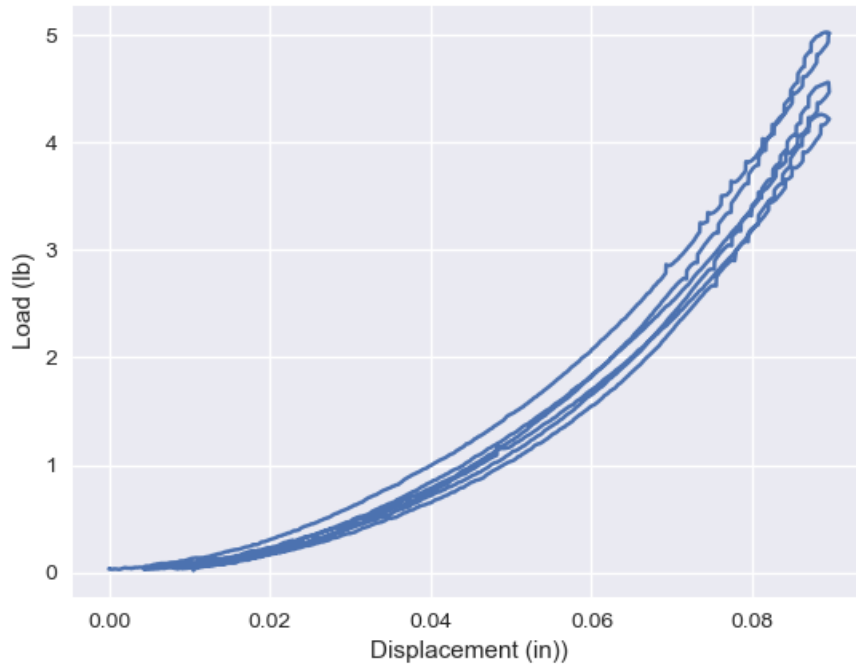
PVA - PVP 3.5 mm 100%/min - Sample:1



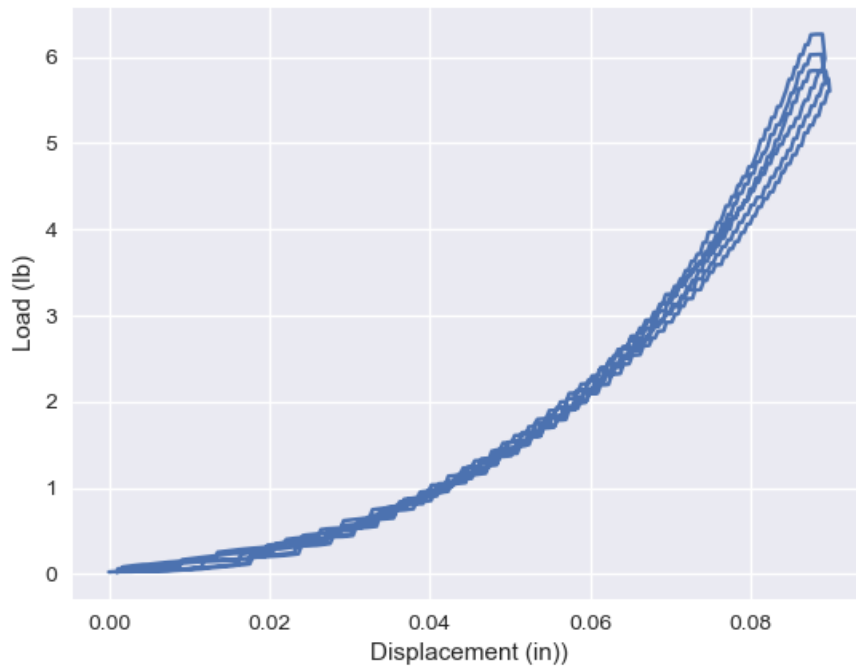
PVA - PVP 3.5 mm 100%/min - Sample:2



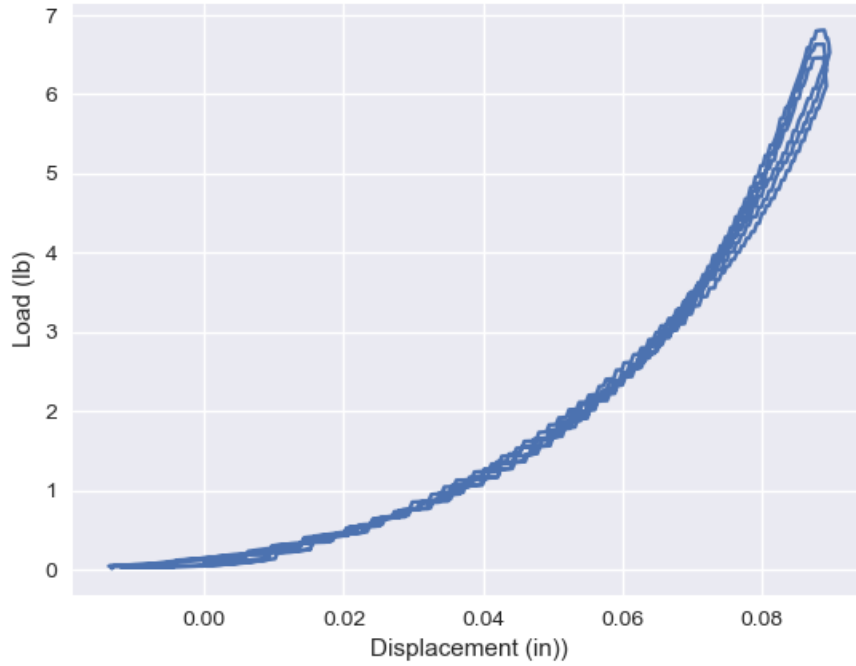
PVA - PVP 3.5 mm 100%/min - Sample:3



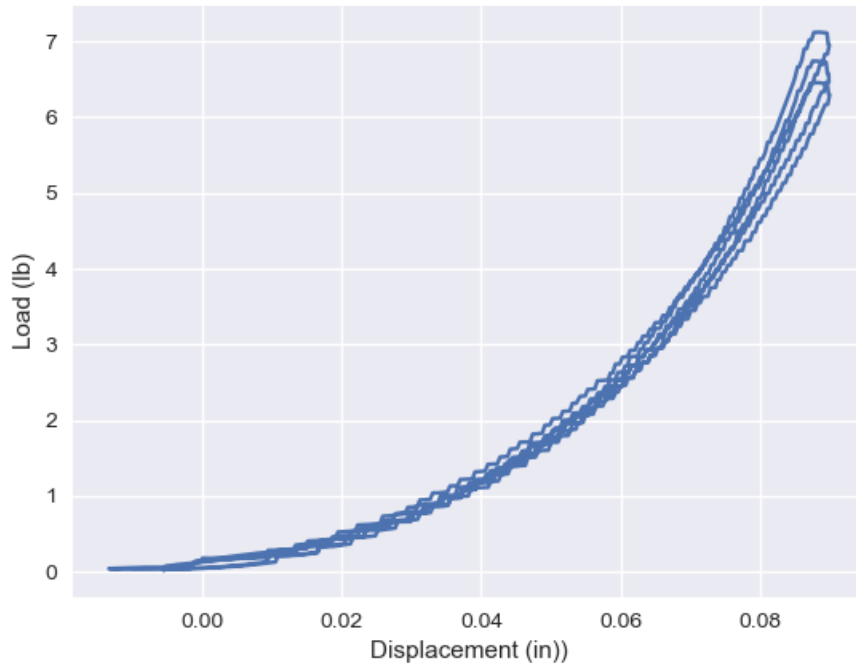
PVA - PVP 3.5 mm 1000%/min - Sample:1



PVA - PVP 3.5 mm 1000%/min - Sample:2



PVA - PVP 3.5 mm 1000%/min - Sample:3



Material	Thickness (mm)	Strain Rate	Sample	Compressive Tangent Stiffness (lb/in)					
				10% Strain	20% Strain	30% Strain	40% Strain	50% Strain	60% Strain
PU	1.5	100	1	23.2542	32.2095	36.4589	45.4286	78.334	131.465
PU	1.5	100	2	12.2649	24.386	77.8147	165.467	301.055	418.882
PU	1.5	100	3	54.7315	140.484	234.859	323.564	451.703	749.654
PU	1.5	1000	1	32.3521	41.2282	48.335	82.4255	132.651	219.277
PU	1.5	1000	2	7.1339	27.9337	91.7926	196.718	341.765	534.752
PU	1.5	1000	3	66.7458	173.307	272.338	366.231	533.73	986.761
PU	2.5	100	1	54.2063	120.67	163.147	242.936	401.767	621.409
PU	2.5	100	2	49.0062	103.29	165.858	283.473	401.809	618.519
PU	2.5	1000	1	60.9643	129.462	178.461	253.39	397.554	723.158
PU	2.5	1000	2	62.4382	127.228	214.585	347.543	522.607	898.286
PU	3.5	100	1	66.6233	139.489	218.537	293.235	406.595	617.303
PU	3.5	100	2	32.7607	91.7041	179.426	269.667	386.604	574.136
PU	3.5	100	3	29.7671	80.6376	200.205	302.738	449.345	688.634
PU	3.5	1000	1	73.9414	150.025	236.897	317.518	444.109	727.409
PU	3.5	1000	2	45.5308	116.986	219.63	312.679	431.336	697.764
PU	3.5	1000	3	31.3655	74.6514	200.183	314.855	451.26	727.321
PVA	1.5	100	1	7.54652	13.9067	21.4926	33.8221	46.083	75.3093
PVA	1.5	100	2	18.5379	25.2215	38.1164	54.2195	77.2821	102.276
PVA	1.5	100	3	23.4247	39.6071	66.9762	105.909	182.037	296.662
PVA	1.5	1000	1	5.82616	17.8597	31.9277	48.7588	74.7868	111.819
PVA	1.5	1000	2	13.8167	26.2975	39.1944	51.5575	78.8658	129.233
PVA	1.5	1000	3	10.0035	33.0447	57.8683	92.2214	155.928	282.985
PVA	2.5	100	1	15.6978	27.7026	42.1309	62.7999	93.8029	146.306

PVA	2.5	1000	1	10.2514	26.4807	35.971	60.8708	90.9857	150.846
PVA	2.5	100	2	28.3931	49.3092	81.7159	109.672	162.615	224.477
PVA	2.5	100	3	9.01976	17.0952	25.5655	47.029	66.4741	108.695
PVA	2.5	1000	2	29.6912	55.835	84.416	118.456	170.885	287.545
PVA	2.5	1000	3	7.45182	19.3052	29.4146	47.2817	70.4392	132.213
PVA	3.5	100	1	16.1815	30.3189	47.9293	68.162	98.6021	139.865
PVA	3.5	100	2	20.1495	32.1578	43.8662	59.9654	83.8377	129.07
PVA	3.5	100	3	13.5495	29.5499	40.3547	55.9074	76.887	108.914
PVA	3.5	1000	1	14.1066	32.201	49.4657	70.4319	101.52	168.267
PVA	3.5	1000	2	25.3156	36.7228	50.4936	70.4223	102.009	187.975
PVA	3.5	1000	3	23.0614	37.6967	55.327	77.3657	110.75	168.743

